ELECTRONIC ABSORPTION SPECTRA OF

MINERALS AT ELEVATED TEMPERATURES

by

Kathleen Marie Parkin

A.B., Oberlin College (1974)

SUBMITTED IN PARTIAL FULFILLMENT
OF THE REQUIREMENTS FOR THE
DEGREE OF

DOCTOR OF PHILOSOPHY

at the

MASSACHUSETTS INSTITUTE OF TECHNOLOGY

(September 1979)

Signature of Author......................................
              Department of Earth & Planetary Sciences
                                  September 6, 1979

Certified by.........../..............................
                                      Thesis Supervisor

Accepted by...
              Lindgren   Chairman, Department Committee

ELECTRONIC ABSORPTION SPECTRA OF

MINERALS AT ELEVATED TEMPERATURES

by

Kathleen Marie Parkin

Submitted to the Department of Earth and Planetary Sciences

on September 6, 1979 in partial fulfillment of the requirements

for the Degree of Doctor of Philosophy.

ABSTRACT

The electronic absorption spectra of a variety of transition metal-bearing minerals were investigated in the temperature range 20C-400C. Overall results indicate a shift in energy of the absorption bands toward the free ion state, broadening of the bands, and an increase in absorption intensity of spin-allowed bands and a decrease of field-independent spin-forbidden band intensity. The energy shift is related to the thermal expansion of the cation site and the degree of distortion of the site. Crystal field (CF) bands due to Fe^{2+} on the highly distorted 8-fold site in almandine and the channel site in beryl show no significant change in energy with increased temperature to 400C, as compared with earlier work which demonstrated a shift to lower energy of approximately 500 cm^{-1} of the CF band arising from Fe^{2+} on the centrosymmetric, slightly distorted Ml site in olivine. Slight energy shifts (<200 cm^{-1}) were also measured for the spin-forbidden, field independent CF bands of Cr^{3+}, Fe^{3+} and Mn^{2+}.

Changes in the intensity of CF bands with temperature can be attributed to increases in vibronic coupling and changes in site distortion with temperature. The intensities of the symmetry-forbidden Cr^{3+} bands in emerald and ruby which are due to vibronic coupling increased by 100% as compared with the 20-50% increase of the symmetry-allowed bands. The most dramatic increase in absorption intensity was evidenced by Fe^{2+} in almandine. Only one of the absorption bands is symmetry-forbidden and yet each band increased in intensity more than 100%. This increase is attributed to the increase in distortion of the 8-fold site. The intensities of the field-independent spin-forbidden bands of Cr^{3+}, Fe^{3+} and Mn^{2+} decreased markedly with increased temperature. No explanation for this effect is presently available.

High temperature absorption spectra of transition metal-bearing minerals give an indication of the degree and nature of cation site expansion if care is exercised to distinguish absorption features due to symmetry-allowed or symmetry-forbidden transitions.

Dr. Roger G. Burns
Professor of Mineralogy and Geochemsitry

TABLE OF CONTENTS

Index of Figures

Page

Index of Tables

Acknowledgements

A thesis is never written in isolation. This work manifests the influence of many people who have helped me through to this day. To my fellow graduate students and cohorts Dan Nolet, Margery Osborne, Julie Morris, Bruce Loeffler, and Carla Montgomery, I owe many thanks. Dr. Alan Parkes was always available with useful suggestions and aid whenever I faced difficulties, experimental and otherwise. My thanks also go to Fran Doughty for the typing of this thesis and to the change ringers of MIT and the Church of the Advent for their encouragement of another kind of insanity during the preparation of this thesis.

I am extremely grateful for the encouragement, inspiration and enlightenment of Professor Roger Burns, who taught me, through example, the meaning of mentor. Much love and heartfelt thanks go to Jim "Igor" Willemin, who not only drafted all the figures contained herein, but provided unhesitating love, courage and support when it was so needed.

This thesis is lovingly dedicated to my mother and in memory of my father, whose encouragement and love have always carried me through.

CHAPTER 1

Introduction

Transition metal cations in minerals are often responsible for mineral color (Loeffler and Burns, 1976; Nassau, 1978) and for the absorption of light in the ultraviolet, visible and near-infrared regions (Burns, 1970; Marfunin, 1979). The energies and intensities of bands in the absorption spectra of minerals are determined by the identity, structure and bonding properties of the absorbing cation and its coordinating atoms. The close relationship between mineral structure and absorption spectra means that structural information must be taken into account in order to analyze absorption spectral data, and that absorption spectra obtained under varying conditions can be used to indicate the structural changes which accompany changes in site occupancy, temperature or pressure.

Many geological processes occur under high temperature and pressure conditions. Absorption spectral changes with increased temperature and/or pressure can be correlated with known structural changes. Once the spectral correlations have been determined, structural information can be extended to minerals of different compositions. Information concerning site size and distortion, cation distribution, and chemical fractionation can then be determined for minerals and compositions whose high temperature structure has not been determined.

The energies of absorption bands are determined primarily by site size. Faye (1972) and Goldman (1977) correlated the average metal-oxygen (M-O) distance with the average energy of the two crystal field bands of Fe^{2+} in distorted octahedral sites ("Δ_{vi}") in a variety of minerals. "Δ_{vi}" decreased $\sim$150 cm^{-1} per 0.01Å increase in the mean M-O distance. Manning (1970) noted the regular increase in the Fe^{3+} Racah-B parameter in the garnet series spessartite < grossularite < andradite which correlates with increasing Fe^{3+}/Al^{3+} - O distances. Abu-Eid (1976) measured significant shifts of absorption bands due to Ti^{3+}, Fe^{2+}, Mn^{3+}, and Cr^{3+} to higher energies with increased pressure and correlated it with the compression of the sites.

Distortion of the cation site from a regular octahedron or tetrahedron enhances the intensity of absorption bands due to transition metal ions. Goldman (1977) correlated the site distortion of Fe^{2+} octahedral sites, measured as the range of M-O distances, with the intensity of the Fe^{2+} absorption bands. After distinguishing those sites that are symmetric with respect to inversion from non-centrosymmetric sites, he noted the increase in absorption intensity with increased site distortion.

The Racah parameters B and C, which can be determined from absorption spectra, are a measure of the covalency of the cation-oxygen bond. Keester and White (1968) demonstrated that the B-parameter is higher for the more ionic manganese

fluoride, oxide, phosphate and sulfate than for silicates and sulfide. Abu-Eid and Burns (1976) noted a decrease in the B-parameter with increased pressure in a suite of Cr^{3+}, Fe^{3+} and Fe^{2+} minerals. As the interatomic distance decreased, the metal-oxygen orbital overlap increased causing an increase in the radius of the 3d electron shell.

The effect of temperature on the size and distortion of cation sites has been determined through x-ray crystal structure determination for a variety of silicates (e.g., Bloss and Papike, 1973; Lager and Meagher, 1978; and others). In general, silica tetrahedra do not expand with temperature. Since many cation sites share edges or corners with the silica tetrahedra, much of the thermal expansion of the crystal is accomodated by increases in cation site size and distortion.

Sung et al. (1977) measured the absorption spectra of Fe^{2+} in olivine and pyroxene at elevated temperature and correlated observed spectral changes with known structural changes. This thesis is an extension of that work to Fe^{2+} in non-octahedral sites in almandine garnet, staurolite, and beryl, and to Cr^{3+} in octahedral coordination in beryl, corundum, diopside, and kyanite, Fe^{3+} in epidote and andradite, and Mn^{2+} in spessartite and rhodonite.

CHAPTER 2

Theoretical Basis

The presence of first row transition metal cations is known to be a source of color in many minerals and to be responsible for the absorption of near-infrared and visible light (Burns, 1970). A principal cause of light absorption in this region is electronic transitions associated with single cations occupying a crystallographic site in the mineral. The energy of an electronic transition depends on several factors including: the identity of the cation and its oxidation state; the coordination number, size and distortion of the site; and the identity of the atoms bonded to the cation (oxygens, hydroxyls, halides). All of these factors contribute to the crystal field or ligand field about the cation (Figgis, 1966).

The presence of the crystal field results in the loss of degeneracy of the free ion terms. For example, the ^4F ground term of Cr^{3+} (d^3) is split by a regular octahedral field into $^4A_{2g}$, $^4T_{2g}$ and $^4T_{1g}$ crystal field states. The energy separation of the terms is determined primarily by the identity of the ligand and the cation-ligand distance, and is measured as the energy of light required to promote an electron from the ground state to an excited state. The degree of splitting of the free ion terms and the relative energies of the resultant crystal field states are presented in the form of Tanabe-Sugano diagrams (d^3, octahedral, Figure 1, Berkes, 1968).
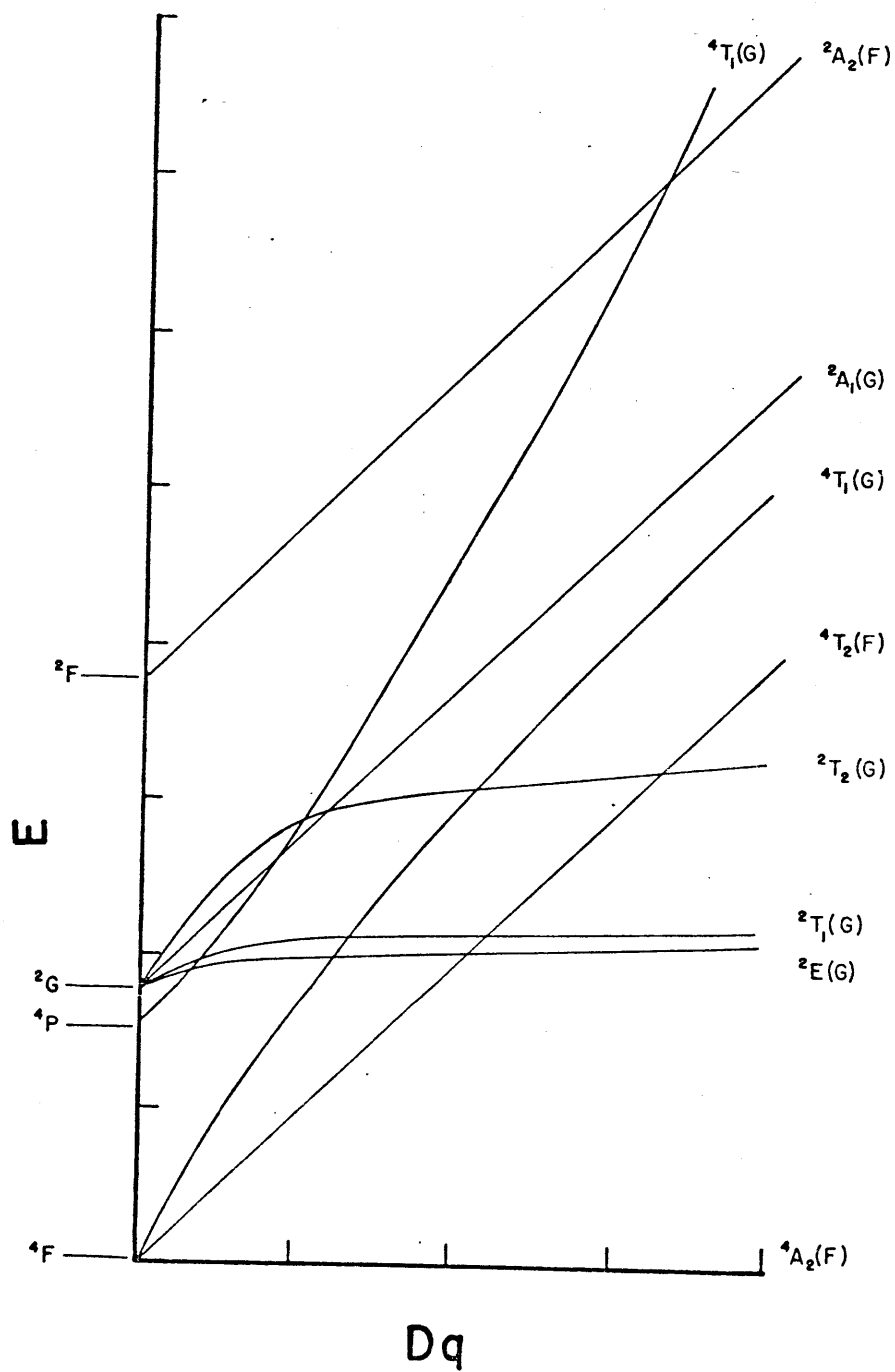
Figure 1. d^3 octahedral energy level diagram (after Berkes, 1968)

Three parameters describe the relative energies of
terms of an ion as split by a crystal field: the crystal
field splitting parameter Δ, and the Racah parameters B and
C. Δ, or 10Dq, is the energy of separation of the two sets
of d orbitals split by a perfect octahedral field. B can
be associated with the interelectronic repulsion terms of
the ionic wave function, and C can be associated loosely
with the shape of the orbitals.

The B-parameter is a function of the interelectronic
repulsion. If the electron orbitals expand, that is, if
there is some overlap of metal and ligand orbitals, B will
decrease. The degree to which B decreases is an indication
of the degree of overlap, or the degree of covalent bonding
between metal and ligands. Jørgensen (1958) proposed two
explanations for the decrease in B. One he termed central
field covalency results from the expansion of the radial
wave function caused by the presence in the core of the central
ion of electrons donated by the ligands. These electrons
decrease the effective charge on the cation and allow radial
expansion of the d-orbitals. They come from the lone pairs
on the ligands and can be in any metal orbital including s, p,
or sp hybrids. The other reason for the decrease in B, which
Jørgensen terms symmetry-restricted covalency, is caused
by the formation of σ-antibonding orbitals of the metal
e_g-orbitals and π-bonding of the t_{2g}-orbitals with appropriate
ligand orbitals. If the main covalency is through t_{2g} π-bonding
the system is better treated by molecular orbital theory.

In both of these cases, the metal orbitals are expanded and the amount of interelectronic repulsion decreases. This is termed the nephelauxetic effect (cloud-expanding). To quantify the amount of covalency, Jørgensen proposed the use of the nephelaxetic ratio $\beta = B/B_o$ where B is the B Racah parameter in the crystal and B_o is the B-parameter in the free gaseous ion.

Δ, B and C can be determined from absorption spectral data of octahedral complexes.

For Fe^{2+} (d^6) ions:

$$\nu_1 \ (^5T_{2g} \rightarrow \ ^5E_g) = \Delta$$

For Cr^{3+} (d^3) ions:

$$\nu_1 \ (^4A_{2g} \rightarrow \ ^4T_{2g}) = \Delta$$

$$\nu_2 \ (^4A_{2g} \rightarrow \ ^4T_{1g}) - \nu_1 = \tfrac{1}{2} (\Delta + 15B - \sqrt{\Delta^2 - 18\Delta B + 225B^2})$$

where ν_1 and ν_2 are the transition frequencies. Therefore,

$$B = \frac{(2\Delta - \nu_2)(\nu_2 - \Delta)}{(27\Delta - 15\nu_2)} + \tfrac{2}{3}\alpha$$

where the final term is added by inclusion of the Racah-Trees correction (Witzke, 1971).

For Mn^{2+} or Fe^{3+} (d^5) ions:

$$\nu_1 \ (^6A_{1g} \rightarrow \ ^4T_{1g}(G)) = -\Delta + 10B + 6C - 26B^2/\Delta$$

$$\nu_2 \ (^6A_{1g} \rightarrow \ ^4T_{2g}(G)) = -\Delta + 18B + 6C - 26B^2/\Delta$$

Therefore, $\nu_2 - \nu_1 = 8B$ (Marfunin, 1979).

In the spectra of minerals discussed here the ligand is usually oxygen or hydroxyl, and its identity does not

change during the course of the experiments. Therefore,
the crystal field splitting, Δ,can be closely correlated
with the cation-ligand distance (e.g., for Fe^{2+} minerals;
Faye, 1972; Goldman, 1977). As the temperature of the
mineral increases, the cation site expands. The influence
of the crystal field on the cation decreases, and the
energy difference between the ground and excited states
approaches that of the free ion configuration. The result
is a shift in the peak maxima of absorption bands to
either higher or lower energy dependent upon the relative
slope of the ground and excited states in the Tanabe-Sugano
diagram. The B Racah parameter will increase as the degree
of orbital overlap decreases with increasing cation-oxygen
distance.

The slope of an excited state on the Tanabe-Sugano
diagram also gives an indication of the width of an absorption
band. A site in a crystal structure is not static because
the cation and ligands undergo thermal vibrations. To a
first approximation, such thermal vibrations cause continual
variations in the cation-ligand distance and is manifested
in the width of the absorption band. As the temperature
increases, band widths increase due to increased thermal
vibration. It is for this reason that most temperature
dependence studies of ligand field transitions are carried
out at temperatures below 300K since bands are narrower and
transition energies (measured as the location peak maxima)
are more defined.

The intensity of an absorption band may also vary with temperature. In order that absorption occur it is necessary that the transition moment, Q, be non-zero.

$$Q = \int \psi_1 \vec{r} \psi_2 d\tau$$

where ψ_1 and ψ_2 are the wave functions of the ground and excited states, respectively, and $\vec{r}$ is the radius vector and has the symmetry of an electric dipole moment (Figgis, 1966). The wave function may be broken down into component functions:

$$\psi = \psi_{orbital} \cdot \psi_{spin} \cdot \psi_{vibrational} \cdot \psi_{rotational} \cdot \psi_{translationa}$$

In the solid state the rotational and translational components are unlikely to change during the lifetime of the excited state. In the absence of mixing of the remaining components, Q will be zero unless

$$\psi_{1, spin} = \psi_{2, spin}$$

that is, there is no difference in spin state between the ground and excited states. A transition in which the spin state changes is termed spin-forbidden. A transition will also have a non-zero intensity only if the reducible representation of the direct product of the symmetries of $\psi_{1, orbital} \, r \, \psi_{2, orbital}$ contains the totally symmetric representation, A_{1g}.

In a regular octahedral ligand field, the symmetries of the $\psi_{1,orbital} (\Gamma_1)$ and $\psi_{2, orbital} (\Gamma_2)$ are symmetric with respect to inversion (g) while the symmetry of the radius vector (Γ_r) is antisymmetric (u). The irreducible

representation of $\Gamma_1\Gamma_r\Gamma_2$ does not contain A_{1g}. Transitions of this type are La Porte-forbidden.

While the spin and symmetry selection rules place constraints on the probability of a given transition, they are not sufficient to determine the intensity of an absorption band. A spin- and La Porte-allowed transition may have zero or near-zero intensity. Conversely, coupling of the vibrational component of the wave function with the electronic component or coupling of the spin component with the electronic component can relax the selection rules. A spin- or La Porte-forbidden transition can thereby have a non-zero intensity. An increase in temperature will increase the occupation of higher energy vibrational levels and can lead to an increase in the intensity of the absorption band.

In minerals, the crystallographic sites occupied by transition metal cations are rarely regular octahedra and many times do not possess a center of symmetry. The symmetries of the orbital wave functions are not g, and it may not be necessary to invoke vibronic coupling in order to explain non-zero absorption intensities.

In addition to losing g symmetry in a distorted octahedral site, the terms of the ground and excited states often lose their degeneracy. For example, for a d^6 cation (Fe^{2+}), a tetragonal distortion of the site causes the octahedral $^5T_{2g}$ ground state to split into $^5B_{2g}$ and ^5E_g states, and the octahedral ^5E_g excited state to split into $^5B_{1g}$ and $^5A_{1g}$ state.

The relative energies of these additional crystal field states are determined by the exact nature and degree of distortion.

Recent determination of the crystal structure of some minerals at elevated temperature (Bloss and Papike, 1973; Meagher, 1975; and others) has demonstrated that the thermal expansion of a crystal is not isotropic. In many silicates (e.g., garnet, pyroxene), the silica tetrahedra remain nearly constant in size and relatively free of distortion as temperature increases to 800-900C. Since the cation octahedral sites often share edges with silica tetrahedra, thermal expansion of the structure can significantly increase the distortion of a cation site and thereby greatly increase the expected intensity of an absorption band when a transition metal cation occupies the site.

CHAPTER 3

Previous High Temperature Mineral Spectra

Earlier investigations of the effect of temperature on the absorption spectra of minerals (McClure, 1962; Burns, 1965; Fukao, et al., 1968; and Sung, et al., 1977) show two trends affecting spectral parameters: change in site size and distortion, and change in the population of the vibrational and electronic energy levels of the cation.

McClure (1962) measured the absorption spectra of Cr^{3+}-, V^{3+}-, and Co^{3+}-doped corundum from 77K to 1200K. The spectra of all three cations showed an overall increase in integrated absorption intensity with increased temperature, as well as shifting of the absorption bands to lower energy and significant broadening.

The total integrated intensity of Cr^{3+} absorption increased approximately 35% as temperature increased to 1000K. McClure noted a much larger increase in intensity of the band which is symmetry forbidden. He attributed the increase to the increased population of higher vibrational levels, and the consequent increase in vibronic coupling.

While the V^{3+} absorption intensity also increased with temperature, the individual absorption bands showed varied influences of temperature. The total integrated intensity $(A \parallel + 2 A\perp)$ of the $^3T_1$ (F) $\rightarrow$ $^3T_1$ (P) band did not change significantly with temperature. McClure offered no explanation of the observation that the band in the $E\perp C$

polarization increased in intensity while the $E \parallel C$ band decreased. The other prominent absorption band, $^3T_1(F) \rightarrow$ $^3T_2(F)$, increased in integrated intensity in both polarizations by more than a factor of two. Again the symmetry-forbidden band showed the most dramatic intensity increase. McClure attributed the increase to increased vibronic coupling and the increased population of the other component of the split $^3T_2$ ground state. The increased temperature allowed the observation of both the $^3A_2(T_2) \rightarrow {}^3T_1(P)$ symmetry-forbidden transition and the $^3E(T_2) \rightarrow {}^3T_1(P)$ symmetry-allowed transition.

The other factor affecting the temperature dependence of crystal field bands is the change in cation site size and distortion. The structural changes with temperature of the Fe sites in olivine appear to be critical to interpretation of the absorption spectra at elevated temperature. Absorption spectra of olivine at temperature have been measured by Burns (1965), Fukao et al. (1968) and Sung et al. (1977). All the researchers found the intensity of the 1.04μ to 1.08μ band (γ polarization) due to Fe^{2+} on the M2 site decreased with increased temperature, while the 1.2μ and 0.8μ bands due to Fe^{2+} on the M1 site increased in intensity (Sung, et al., 1977). The crystal structure of olivine to 900C has been determined by Brown and Prewitt (1973), Smyth and Hazen (1973), and Smyth (1975). As the temperature increased both Fe sites increased in distortion and expanded. The M2 site, however, became more centrosymmetric. The electronic

transition due to Fe^{2+} in the M2 site lost intensity due to the near addition of a center of symmetry to the site. The 1.2μ and 0.8μ bands reflected the increase in distortion of the Ml site with temperature.

Sung et al. (1977) also reported the transmission and reflectance spectra of Fe^{2+} in pyroxene. The absorption band at 0.9μ due to Fe^{2+} in both the Ml and M2 sites intensified and moved to longer wavelengths in both ortho- and clinopyroxene. The 1.8μ band in orthopyroxene (Fs_{14}) did not shift in energy with temperature, but decreased in intensity.

CHAPTER 4

Experimental Methods

1. Absorption Spectra

Visible-near-infrared absorption spectra were obtained
in the region 330nm to 2500nm using a Cary 17 spectrophotometer.
Polaroid sheet polarizers HN42 for the visible and HR for
the near-infrared, allowed the incident beam to be polarized.

Mineral samples were cut parallel to the indicatrix
axes using external crystal morphology as a guide whenever
possible. Optic orientations were confirmed with a polarizing
microscope by interference figures or using a universal-stage
attachment. When it was not possible to use crystal morphology
to orient the crystals a thin section was first prepared and
the mineral orientation was determined using universal-stage
microscopy. A thicker oriented section was then cut from
the original crystal for the spectral measurements.

Samples were polished on both sides using 1μm alumina.
The crystals were polished while attached to glass slides
by Apeizon W wax which melted at approximately 100C. The
wax was removed from the crystals by dissolution in carbon
tetrachloride. Sample thickness was measured using a
Starrett metric micrometer caliper to an accuracy of ± 0.02mm.

The samples were heated during measurement of the spectra
in a furnace designed by Dr. Chuen-Min Sung (Sung et al., 1977).
Samples were attached to a brass mask with Eastman 910 adhesive
which loses its cohesive strength at approximately 300C.

Samples measured above 300C were held in the furnace solely by friction. This arrangement made measurements of small samples (<2mm diameter) difficult.

The arrangement of the sample compartment in the spectrophotometer allowed some thermal contact between the polarizers and the heated sample holder. As a result, partial darkening of the polarizers occurred over time.

The major problem encountered during the measurement of spectra at temperatures above 200C was the dramatic increase in instrumental noise in the infrared region. In order to decrease the noise, the pen was damped using the Pen Period circuitry of the Cary 17 and spectra were recorded at a much slower rate. Possibly related to the noise problem was the impossibility of keeping the slitwidth on scale throughout the infrared region. The double-beam Cary 17 spectrophotometer attempts to maintain a constant reference beam intensity through the use of variable incoming beam slitwidth. Although there was no apparent thermal contact between either the infrared lead sulfide detector or the reference beam chamber and the sample furnace, insufficient light reached the detector even with the slits opened to their maximum in the region 750nm to ∿850nm. This led to severe problems in determining the baseline of Cr^{3+} spectra at 300C and 400C.

2. Electron Microprobe Analysis

Major element compositions of the samples were measured
on an automated MAC-5 electron microprobe, operating at 15kV
accelerating voltage and 30nA sample current. Matrix
corrections were made using ALPHA correction factors (Bence
and Albee, 1968; Albee and Ray, 1970). Standards were
primarily mineral standards maintained by the MIT microprobe
facility. All compositions are reported as weight per cent
of the oxides and all iron is expressed as FeO.

3. Curve Fitting Procedure

Spectra recorded on chart paper in analogue mode were digitized on a Wayne-George Coördicon X-Y Coordinate Converter and curve fitted using the author's modification of the Mossbauer spectra curve resolution program of Stone et al. (1971). The function used in the fitting procedure was a sum of Gaussian line shapes added to a constant baseline (I_o) and an exponential absorption edge of the form:

$$F(x) = I_o + ae^{bx^2} + \sum_i I_i \exp(4(\ln 0.5)(x - E_i)^2/W_i^2)$$

where a and b are parameters of the absorption edge, and I_i, E_i and W_i are the intensity at peak maximum, peak position, and full width at half maximum (FWHM) of each peak (i), respectively.

In order to achieve convergence in a reasonable time, initial estimates of the spectral parameters needed to be carefully chosen. The digitized spectra were plotted with x linear with energy using a Calcomp 580 in the mode of a Stromberg-Carlson 4020. These plots were then transfered to the plotting bed of a Hewlett Packard 7210A Digital Plotter attached to the Digital Equipment Corporation PDP11/20 computer maintained by the MIT electron microprobe facility. The plots were overlaid by tracing paper and through successive approximation of the spectral parameters, a good visual fit of the function to the data was achieved. The absorption edge parameters were first approximated using the Exponential Curve Fitting program of the Hewlett-Packard 19C which finds the regression coefficients a and b from solving

the linear equations:

$$\begin{bmatrix} n & x_i^2 \\ x_i^2 & x_i^4 \end{bmatrix} \begin{bmatrix} \ln a \\ b \end{bmatrix} = \begin{bmatrix} \ln y_i \\ x_i^2 \ln y_i \end{bmatrix}$$

The Stone et al. (1971) curve fitting program uses the Gauss non-linear regression procedure and allows any parameter to be constrained equal to the initial estimate. For all the spectra it was necessary at first to constrain the baseline and absorption edge parameters (I_o, a, and b) to be equal to their initial estimates. After the peak parameters were allowed to converge, the constraints on the absorption edge parameters, a and b, could be lifted. Finally, it was usually possible to lift the constraint on I_o, if the baseline was well defined by the data.

For the spectra with weak, broad peaks, such as chromediopside and andradite, it was necessary to constrain the widths of such peaks constant, allow the other parameters to converge, and then release the width constraints.

Three problems still exist concerning the curve fitting program. First, at this point there is no reasonable estimate of the weighting factor for the data points. The usual statistical weight of a data point is the inverse of the estimated variance, that is, the inverse of the square of the estimated error ($1/\hat{\sigma}^2$). The estimated error in counting statistics (number of data points)$^{1/2}$ is the weighting factor used in Mössbauer spectroscopy fitting procedures. No comparable

easily determined, factor is available for absorption spectra.
The present weighting factor used in the absorption spectra
fitting procedure in 0.5% of the value of y in absorbance
units. This leads to unreasonable values of the sum of
the squares of the weighted residuals,

$$R^2 = \sum_{i=1}^{n} [w(x_i) \cdot (y_i - F(x_i))]^2$$

where (x_i, y_i) are the experimental data points, $F(x_i)$ is
the value of the fit function at x_i, n is the number of data
points, and $w(x_i) = 0.005 \cdot y_k$.

Another possible option for $w(x_i)$ is to use some function
of the pen noise. Alternatively, some function of x_i and y_i
may be able to be determined to measure reproducibility of
spectra.

The second major problem concerning the fitting procedure
involves the assumption that the absorption spectral bands
are pure Gaussian line shapes. From attempts to fit well
characterized single bands in the emerald spectra, Wood (1965) it has
been determined that this is not a reasonable assumption.
The bands are skewed and it will probably be necessary to
introduce a new peak parameter to the fitting procedure in
order to adequately fit skewed bands.

Finally, the absorption edge function was chosen by
assuming the edge was due to an intense ligand-to-cation
charge transfer band in the ultraviolet. If, as appears to
be the case for Cr^{3+}-kyanite, the absorption edge is partially
due to light scattering, the choice of the function ae^{bx^2}
may be inadequate, and another function should be considered.

The fit spectral data are presented for each mineral in tabulated form. Baseline parameters (I_o, a, and b), peak parameters E (peak position), W (full width at half maximum), and I (intensity at peak maximum) and the peak area,

$$A = \frac{\pi}{|4 \ln 0.5|}^{1/2} W \cdot I$$

for each peak, the uncertainties in these parameters, and R^2/degrees of freedom for each spectrum are reported. In those cases where it was necessary to constrain a parameter throughout the fitting procedure, a (c) follows the value of the parameter.

CHAPTER 5

d^3-Minerals: Cr^{3+}

Chromium in its most common oxidation state, Cr^{3+}, is a d^3 ion which can easily substitute in minerals for octahedral Al^{3+}, Fe^{3+}, Fe^{2+} or Mg^{2+}. The lowest energy states of the d^3 free ion are ^4F (ground state), ^4P, ^2G, and ^2F states. An octahedral crystal field splits the free ion states as follows: ^4F into $^4A_{2g}$, $^4T_{2g}$ and $^4T_{1g}$; ^4P into $^4T_{1g}$; and ^2G into ^2E_g, $^2T_{1g}$, $^2T_{2g}$, and $^2A_{1g}$. The ^2F state is also split ($^2A_{2g}$, $^2T_{1g}$, $^2T_{2g}$) but is of sufficiently higher energy that transitions involving these states are not measured in the energy region studied (Wood et al., 1963).

Three spin-allowed transitions are measured in the visible and near-ultraviolet region:

$$^4A_{2g} \rightarrow {}^4T_{2g}(F) \qquad (1)$$

$$^4A_{2g} \rightarrow {}^4T_{1g}(F) \qquad (2)$$

$$^4A_{2g} \rightarrow {}^4T_{1g}(P) \qquad (3)$$
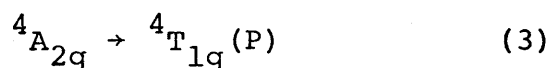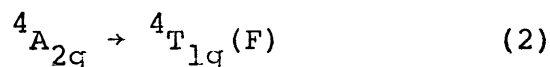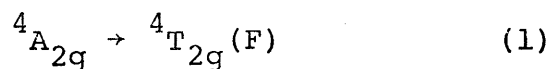
These transitions are crystal field dependent and have a positive slope on the Tanabe-Sugano diagram.

Three spin-forbidden transitions are also measured in this energy region:

$$^4A_{2g} \rightarrow {}^2E_g(G) \qquad (4)$$

$$^4A_{2g} \rightarrow {}^2T_{1g}(G) \qquad (5)$$

$$^4A_{2g} \rightarrow {}^2T_{2g}(G) \qquad (6)$$
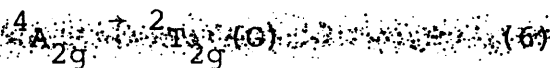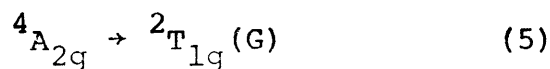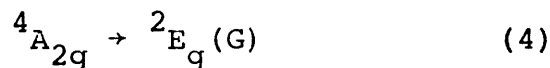
Transitions 4 and 5 are relatively crystal field independent and therefore observed as sharp, temperature independent absorption bands. Transition 6 is broad with low intensity.

Four chromium-bearing minerals were investigated to determine the temperature dependence of the Cr^{3+} absorption bands: Cr-corundum (ruby), Cr-beryl (emerald), Cr-kyanite, and Cr-diopside. In ruby, emerald, and kyanite, chromium occupies a slightly distorted octahedral aluminum site (mean M-O distance: $\sim 1.91 \overset{o}{A}$). Chromium occupies a slightly distorted octahedral (Fe, Mg) site in chromdiopside (mean M-O distance: $2.08 \overset{o}{A}$). The compositions and sources of the chromium mineral samples used are reported in Table 1.

Table 1

Cr^{3+} Minerals: Chemical Compositions and Sources

	Cr-Beryl	Cr-Corundum	Cr-Kyanite	Cr-Diopside
SiO_2	67.40(21)	0.02(1)	37.45(43)	54.55(21)
TiO_2	0.02(1)	0.0	0.0	0.0
Al_2O_3	17.84(7)	100.06(33)	62.68(55)	0.58(8)
Cr_2O_3	0.10(2)	0.30(2)	0.65(7)	1.34(7)
MgO	0.45(2)	0.02(1)	0.02(1)	16.43(14)
CaO	0.00(1)	0.03(1)	0.0	24.95(3)
MnO	0.00(1)	0.0	0.04(2)	0.08(2)
FeO	0.09(1)	0.10(2)	0.12(2)	2.04(18)
Na_2O	0.38(3)	0.02(1)	0.03(2)	0.43(2)
K_2O	0.02(1)	0.01(1)	0.01(1)	0.01(1)
Total:	86.30	100.55	100.98	100.42

Cr-Beryl   HVD #97472, Minas Columbia
             ω-ϵ section 0.2042(2) cm

Cr-Corundum HVD #96074, loc. unknown
             ω-ϵ section 0.0792(2) cm

Cr-Kyanite   HVD #105693, with fuchsite, Leydsdorp Dist., Transvaal, S. Africa
             β-γ section 0.0218(2) cm
             α section (not determined)

Cr-Diopside HVD #105019, Outokompu, Finland
             α-γ section 0.0242(2) cm
             β section 0.0257(2) cm

1. Ruby - Cr^{3+}-corundum

Cr^{3+} in corundum occupies the distorted octahedral Al^{3+} site (mean M-O distance 1.91Å, Moss and Newnham, 1964) with site symmetry C_{3v}. The absorption spectra of Cr^{3+} in corundum has been well studied (McClure, 1962; Kushida, 1966). The spectrum in each polarization consists of two broad bands in the visible region arising from $^4A_2 \rightarrow {}^4T_2$ at 18,000 cm^{-1} and $^4A_2 \rightarrow {}^4T_1$ at 25,700 cm^{-1} (Wood et al., 1963). The ^4T states are split by the low site symmetry and transitions to the resultant states are polarization dependent. The polarized spectra have been assigned:
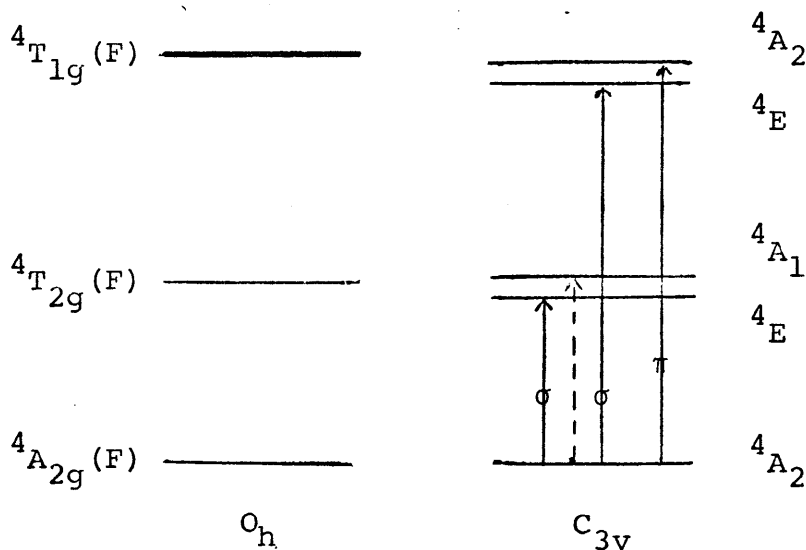
Only the $^4A_2 \rightarrow {}^4A_2$ transition is symmetry-allowed in the $E \| C$ spectrum, while the $^4A_2 \rightarrow {}^4E$ transitions are symmetry-allowed in the $E \perp C$ polarization. Vibronic coupling must be invoked in order to explain the presence of the low energy band in the $E \| C$ spectrum.

Three spin-forbidden bands are observed in the visible region as sharp peaks at 14,430 cm^{-1} ($^4A_2 \rightarrow {}^2E$), 15,110 cm^{-1}

$(^4A_2 \rightarrow {}^2T_1)$ and 21,140 cm^{-1} $(^4A_2 \rightarrow {}^2T_2)$ (Kushida <u>et al</u>., 1966).

The ^2T states have been split by the low site symmetry.

McClure (1962) reported the absorption spectra of ruby from 77K to 1175K. As discussed previously, he noted the shift in the absorption bands to lower energy, band broadening, and an overall increase in absorption intensity. In particular, the $^4A_2 \rightarrow {}^4A_1 (T_2)$ band, which is symmetry-forbidden, increases in intensity far more rapidly than the others.

The total absorption strength to the $^4T_2 (F)$ and $^4T_1 (F)$ states is measured by $A \parallel + 2A\underline{\perp}$ where $A \parallel$ and $A \underline{\perp}$ are the integrated intensities observed in $E \parallel C$ and $E\underline{\perp}C$ polarized spectra, respectively. McClure (1962) empirically determined the intensity increase to be represented by

$$A(T)/A(0) = 1 + \exp (-\theta_D/T)$$

where $\theta_D = 1050 \pm 30K$.

Results

The absorption spectra of a natural ruby containing 0.30 wt.% Cr_2O_3 were measured at five temperatures from 20C to 400C (Figures 2 and 3). The sample was not completely optically clear. The cloudiness could be the result of micro-fractures or micro-inclusions, although there was no indication from the electron microprobe analysis of inclusions. The lack of clarity in the sample is probably the reason why the spin-forbidden bands are poorly defined.

Both the $E \parallel C$ and $E\underline{\perp}C$ spectra were fit to four peaks (Figures 4 and 5). The two high energy, broad and intense
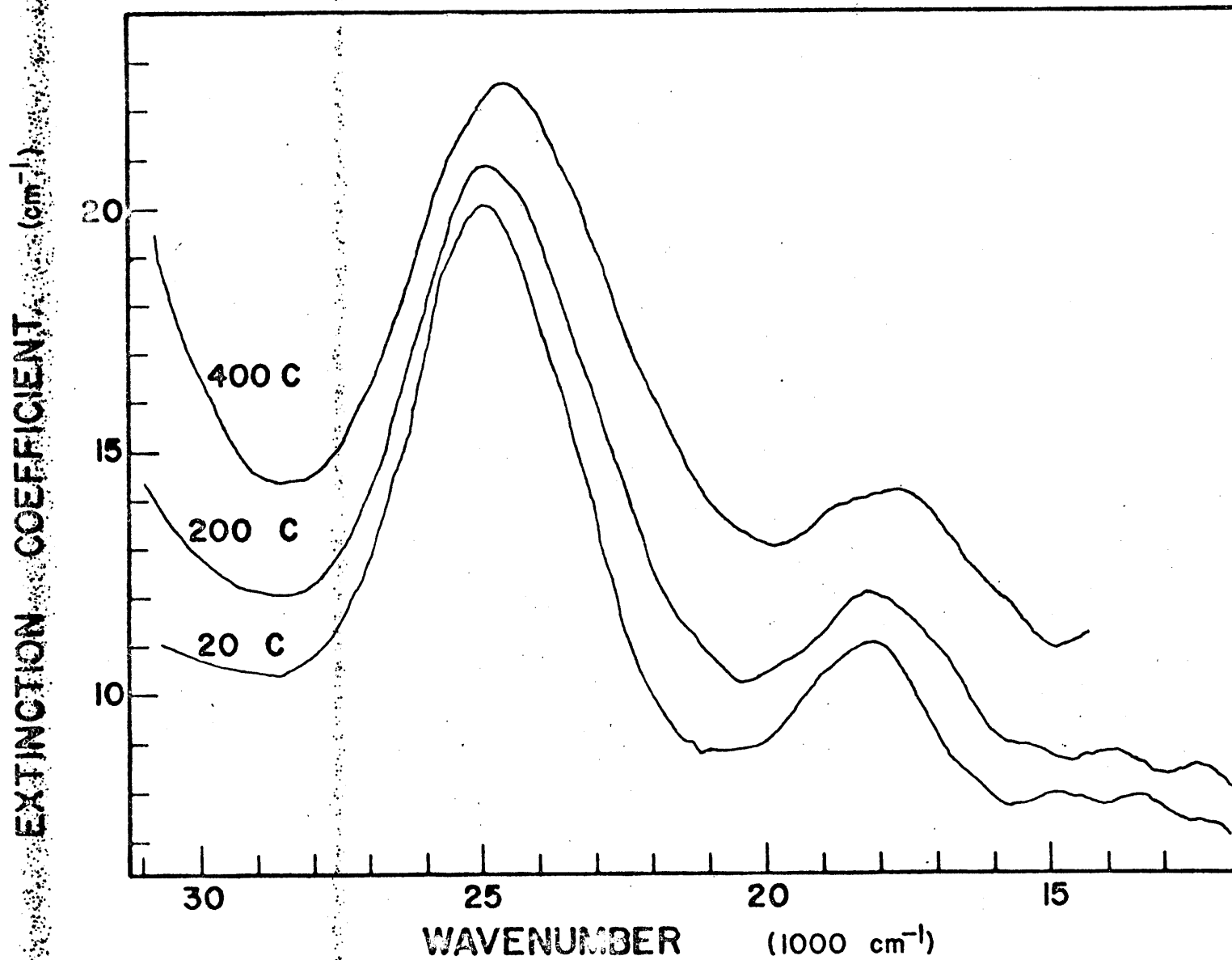
Figure 2. Absorption spectra of Cr^{3+}-corundum $(E||c)$ at 20C, 200C, and 400C
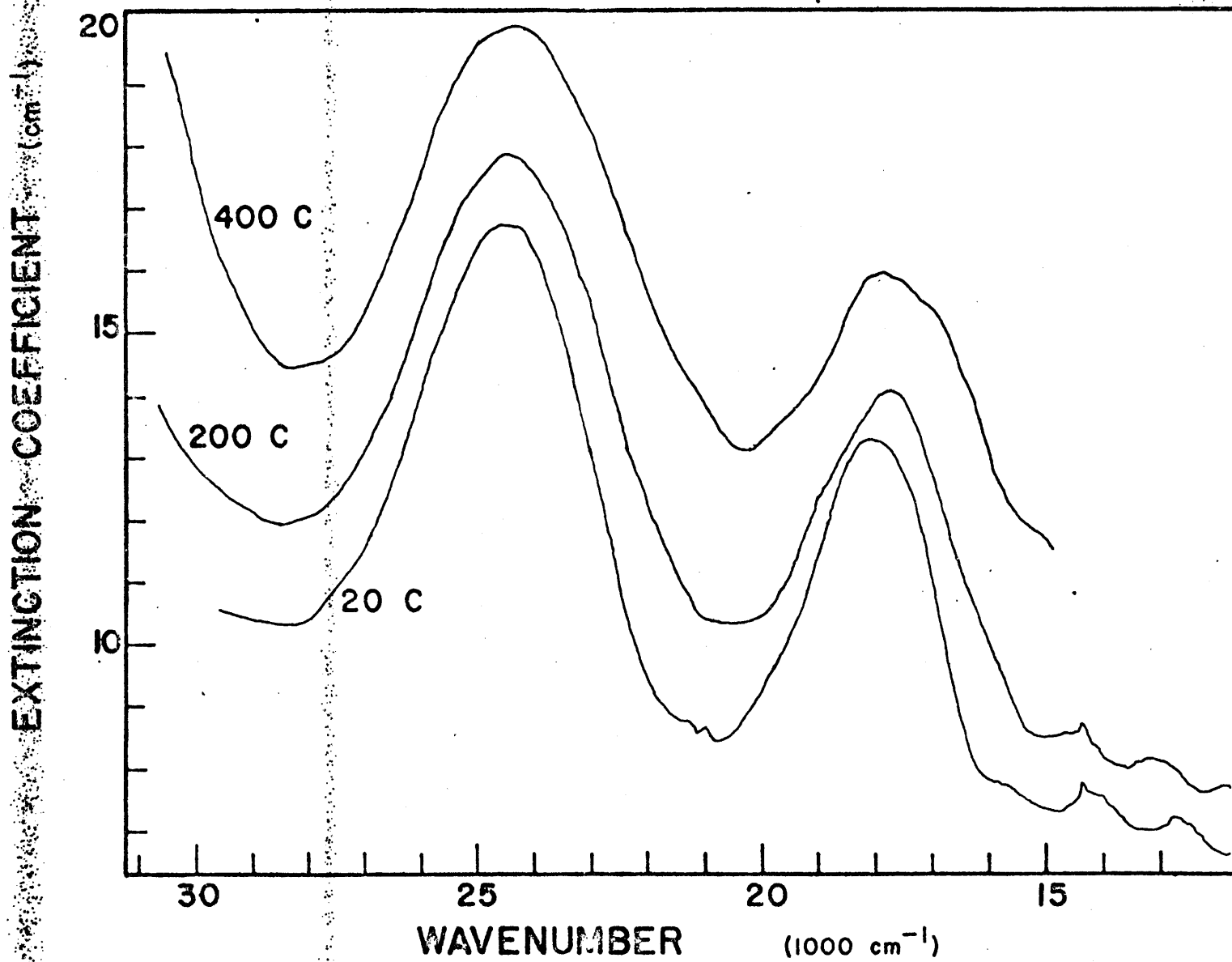
Figure 3.   Absorption spectra of Cr^{3+}-corundum ($E{\perp}c$) at 20C, 200C, and 400C
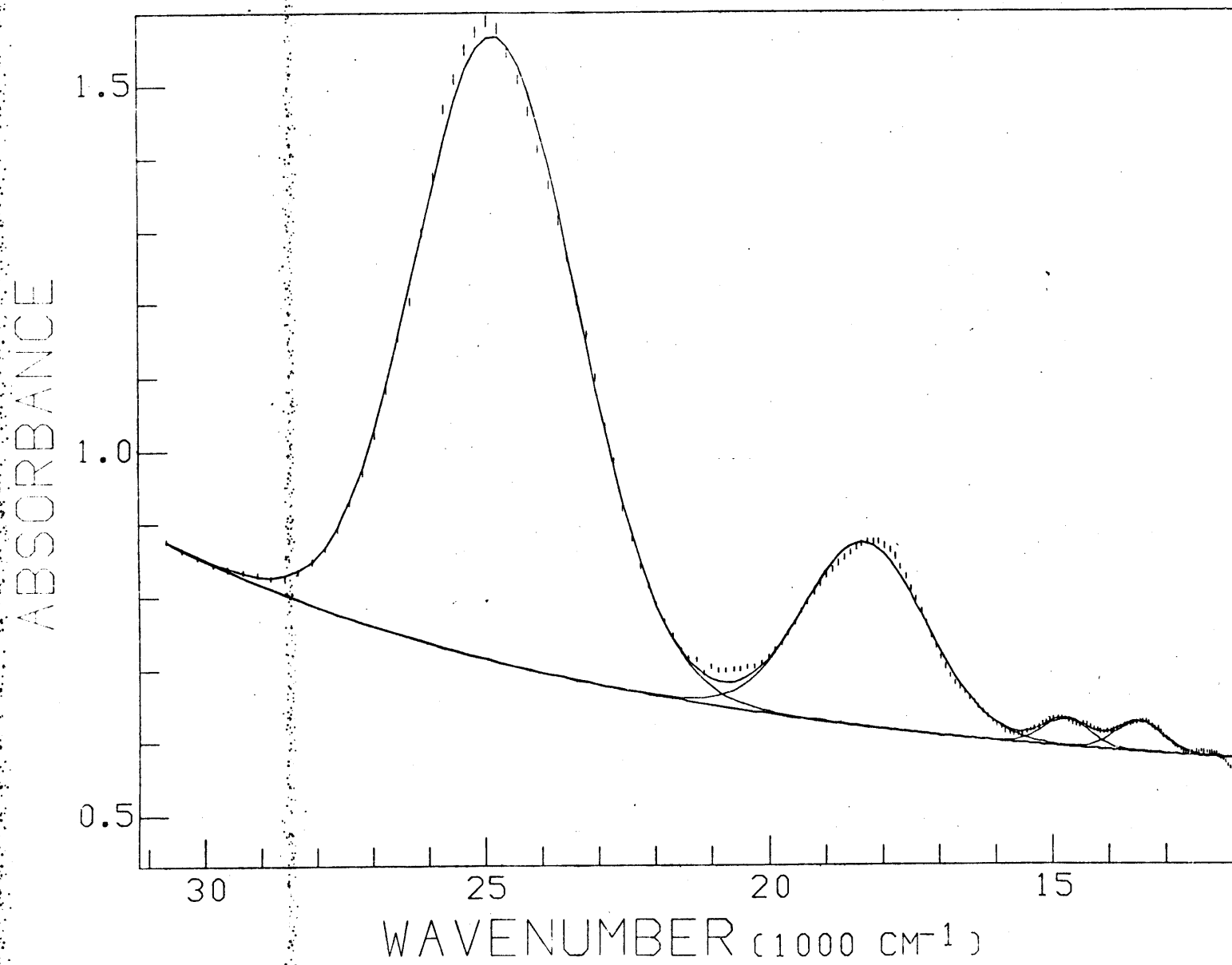
Figure 4.   20C spectrum of Cr^{3+}-corundum $(E||c)$, computer fit
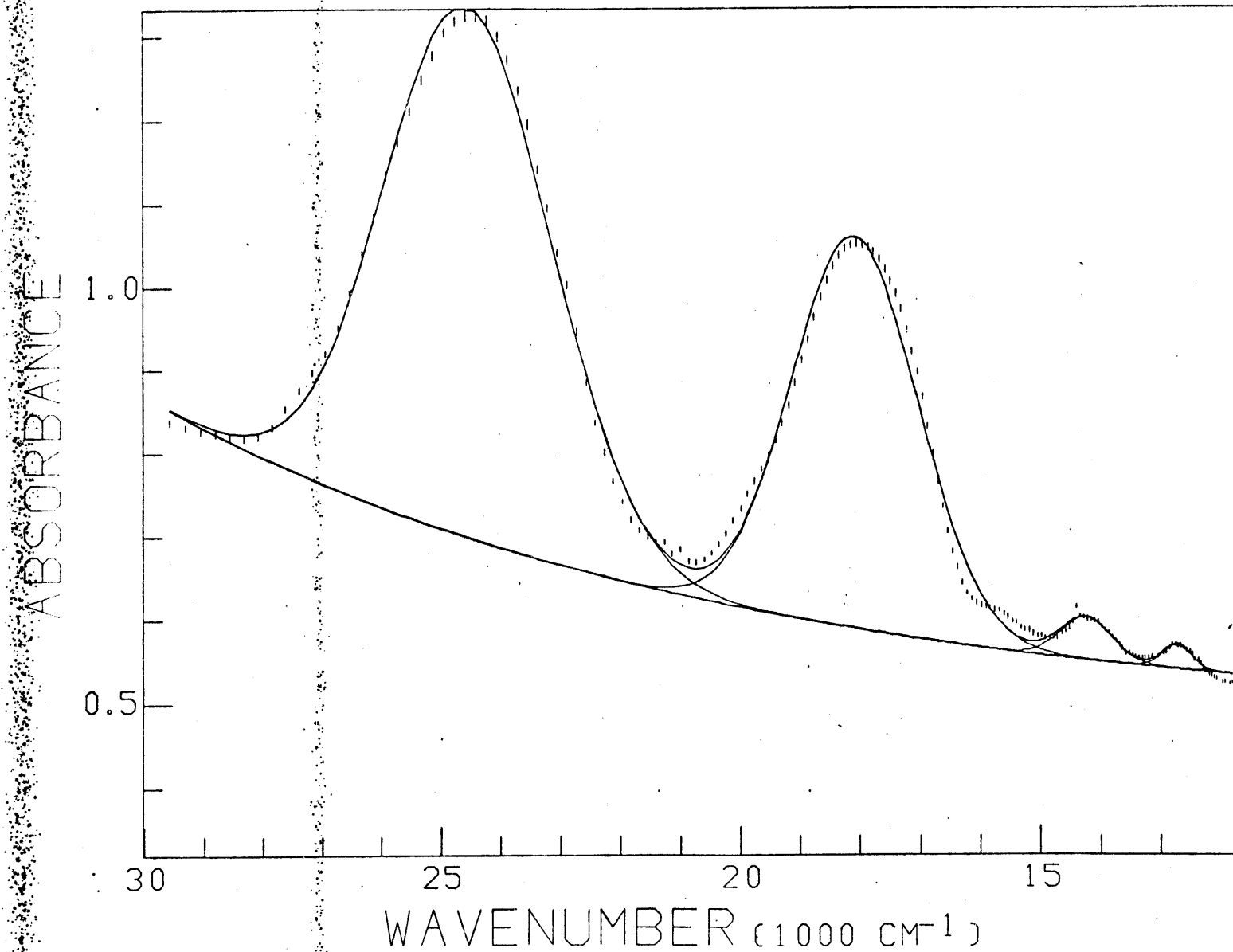
Figure 5. 20C spectrum of Cr^{3+}-corundum ($E\perp c$), computer fit

absorptions are obviously due to the spin-allowed Cr^{3+} transitions. The low energy bands cannot be explained presently. While the band at 14,500 cm^{-1} is at approximately the correct energy to be the Cr^{3+} $^4A_2 \to {}^2E$ transition, the band is too broad ($\sim$1000 cm^{-1} as compared to $\sim$200 cm^{-1}). The lower energy band does not correspond with any Cr^{3+} transition. The sample contains $\sim$0.10 wt.% FeO and this band could be due to Fe^{2+} spin-allowed $^5T_2 \to {}^5E$ transition. While the energy of the band is somewhat high for this transition, again the problem is the band width. It would be expected that $^5T_2 \to {}^5E$ Fe^{2+} band would be broader than the measured $\sim$1000 cm^{-1}. Also, the temperature dependence of the band is opposite to that expected for a Fe^{2+} crystal field band. The bands were fit in order to assure the correct determination of the baseline.

The absorption spectra parameters: band position (E), full width at half maximum (W), extinction coefficeint maximum (I), and integrated intensity (A) for each peak are presented in Tables 2 and 3 for the E $\parallel$ C and E$\perp$C spectra, respectively.

The spin-allowed Cr^{3+} bands in ruby shifted to lower energy by 330 cm^{-1} to 430 cm^{-1} over the temperature range 20C to 400C and broadened 40-85%. The increase in integrated intensity was found to be significantly greater than that measured by McClure (1962). The absorption bands increased in integrated intensity by 40-185%. The symmetry forbidden absorption band $^4A_2 \to {}^4A_1 (^4T_2)$ showed the greatest increase.

Table 2

Cr-corundum (E‖C) Absorption Spectra Parameters

	20C	100C	200C	300C	400C
baseline (abs)	0.4397(c)	0.5096(c)	0.656(1)	0.687(4)	0.72(2)
a (abs)	0.1105(7)	0.0547(6)	0.0027(4)	0.0008(1)	0.0005(2)
b (cm^{-2})	0.00146(1)	0.00206(1)	0.0054(1)	0.0069(2)	0.0078(3)
$^4A_2 \rightarrow {}^4A_2(T_1)$					
E (nm)	403	404	407	408	410
E (1000 cm^{-1})	24.790(4)	24.737(4)	24.584(5)	24.510(7)	24.396(7)
W (1000 cm^{-1})	3.36(1)	3.55(1)	4.16(2)	4.49(2)	4.80(3)
I (cm^{-1})	10.84(4)	10.90(4)	11.23(5)	11.90(6)	12.5(2)
A (1000 cm^{-2})	38.7(2)	41.2(2)	49.8(3)	56.9(4)	63.8(14)
$^4A_2 \rightarrow {}^4A_1(T_2)$					
E (nm)	546	548	550	554	559
E (1000 cm^{-1})	18.301(5)	18.249(6)	18.171(7)	18.056(9)	17.87(2)
W (1000 cm^{-1})	2.53(1)	2.61(2)	3.23(2)	4.05(4)	4.7(2)
I (cm^{-1})	3.18(2)	2.99(2)	3.49(2)	4.15(5)	4.9(3)
A (1000 cm^{-2})	8.57(6)	8.33(7)	11.98(9)	17.9(4)	24.3(22)
E (nm)	678	671	659		
E (1000 cm^{-1})	14.75(2)	14.90(3)	15.16(3)		
W (1000 cm^{-1})	0.98(5)	0.75(7)	0.49(9)		
I (cm^{-1})	0.47(2)	0.27(2)	0.17(2)		
A (1000 cm^{-2})	0.49(3)	0.22(2)	0.09(2)		
E (nm)	743	732	717	712	709
E (1000 cm^{-1})	13.46(2)	13.66(2)	13.94(2)	14.04(2)	14.10(13)
W (1000 cm^{-1})	0.98(5)	1.09(6)	0.99(5)	1.31(5)	1.1(2)
I (cm^{-1})	0.52(1)	0.45(1)	0.44(2)	0.92(4)	1.3(2)
A (1000 cm^{-2})	0.54(3)	0.52(3)	0.47(3)	1.23(7)	1.5(5)
R^2	598/163	779/159	1230/150	677/153	414/115

Table 3

Cr-Corundum ($E \perp C$) Absorption Spectra Parameters

	20C	100C	200C	300C	400C
baseline (abs)	0.330(c)	0.4095(c)	0.574(5)	0.679(1)	0.800(c)
a (abs)	0.1722(8)	0.0972(9)	0.021(3)	0.0011(2)	0.00014(2)
b (cm^{-2})	0.001266(7)	0.00173(1)	0.0034(2)	0.0066(2)	0.0092(2)

$^4A_2 \rightarrow {}^4E(T_1)$

	20C	100C	200C	300C	400C
E (nm)	407	409	411	412	413
E ($1000\ cm^{-1}$)	24.549(5)	24.473(5)	24.324(6)	24.294(8)	24.220(9)
W ($1000\ cm^{-1}$)	3.30(1)	3.63(1)	4.23(3)	4.70(2)	5.06(3)
I (cm^{-1})	8.07(3)	7.85(3)	8.51(6)	9.12(4)	9.45(4)
A ($1000\ cm^{-2}$)	28.3(1)	30.3(2)	38.3(5)	45.6(3)	50.8(3)

$^4A_2 \rightarrow {}^4E(T_2)$

	20C	100C	200C	300C	400C
E (nm)	553	556	559	561	566
E ($1000\ cm^{-1}$)	18.087(3)	17.989(3)	17.890(4)	17.811(5)	17.661(7)
W ($1000\ cm^{-1}$)	2.480(9)	2.702(9)	3.11(1)	3.32(1)	3.61(2)
I (cm^{-1})	5.93(2)	5.99(2)	5.91(3)	5.86(3)	5.79(2)
A ($1000\ cm^{-2}$)	15.66(7)	17.24(9)	19.5(2)	20.7(1)	22.24(10)

	20C	100C	200C	300C	400C
E (nm)	702	698	694	692	
E ($1000\ cm^{-1}$)	14.23(1)	14.32(1)	14.40(1)	14.45(2)	
W ($1000\ cm^{-1}$)	1.00(c)	1.03(3)	0.83(3)	0.88(6)	
I (cm^{-1})	0.64(2)	0.69(2)	0.68(2)	0.47(2)	
A ($1000\ cm^{-2}$)	0.68(2)	0.75(2)	0.59(2)	0.44(3)	

	20C	100C	200C	300C	400C
E (nm)	786	774	761	751	
E ($1000\ cm^{-1}$)	12.72(1)	12.91(1)	13.15(2)	13.32(2)	
W ($1000\ cm^{-1}$)	0.53(4)	0.76(4)	0.89(5)	0.78(4)	
I (cm^{-1})	0.36(2)	0.42(2)	0.47(2)	0.56(2)	
A ($1000\ cm^{-2}$)	0.22(2)	0.34(2)	0.44(3)	0.47(3)	
R^2	2205/155	1102/155	563/150	426/155	339/108

in integrated intensity. Plotted in Figure 6 are the integrated intensities of the bands normalized to the room temperature value.
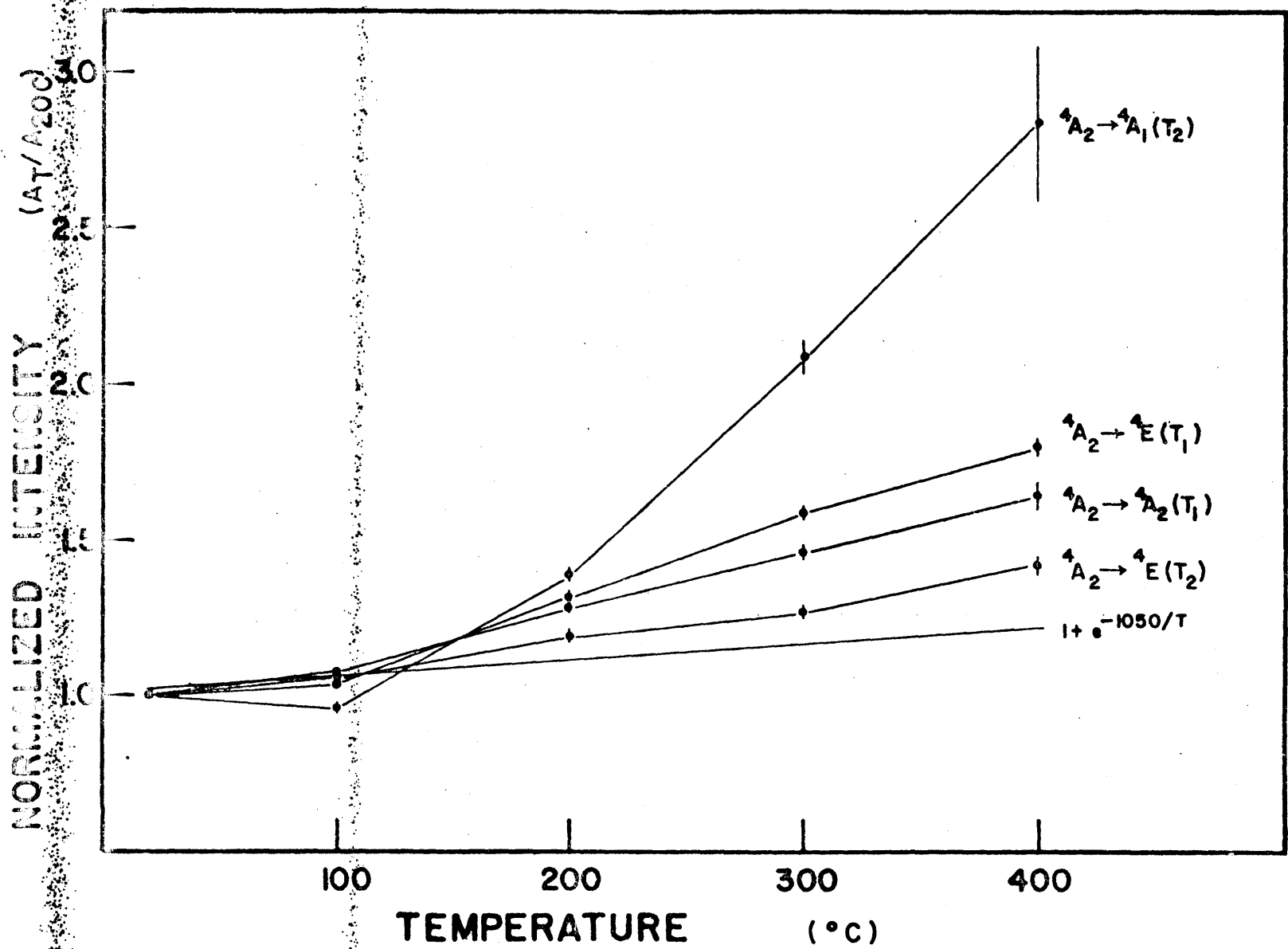
Figure 6. Temperature dependence of normalized intensities of Cr^{3+}-corundum bands

2. Emerald - Cr^{3+}-beryl

Cr^{3+} in beryl occupies the six-coordinate Al^{3+} site (M-O distance 1.907Å, Gibbs et al. (1968)) with site symmetry D_3. The absorption spectrum of Cr^{3+}-beryl has been measured by many workers and there has been little dispute concerning the assignment of the spectrum. Schmetzer et al. (1974) have summarized the results of previous workers as well as comparing the absorption spectra of synthetic and natural Cr-emeralds.

The spectral assignment of Cr-emerald is:

band (cm^{-1})	assignment	sharp (S) or broad (B)
14,700-14,800	$^4A_2 \rightarrow {}^2E$	S
15,100-15,150	$^4A_2 \rightarrow {}^2T_1$	S
15,500-15,550		
16,000-16,700	$^4A_2 \rightarrow {}^4T_2$	B
21,000-21,200	$^4A_2 \rightarrow {}^2T_2$	S weak
23,300-24,000	$^4A_2 \rightarrow {}^4T_1$	B

Wood (1965) reported a detailed crystal field analysis of emerald, and observed that the $^4T_1$ and $^4T_2$ states are not degenerate. This was attributed to "distortion of the equivalent electrostatic crystalline field and the Al^{3+} site", since the early structure determination of beryl (Bragg and West, 1926) found the Al^{3+} site to be essentially a regular octahedron. More recent structural investigation of beryl (Gibbs et al, 1968) has shown the Al^{3+} site to be sufficiently distorted

to cause the non-degeneracy of the Cr^{3+} states. Wood (1965) assigned the spin-allowed Cr^{3+} spectra of emerald as:

$^4T_1(36,982)$	^4E (41,320)
	$^4A_2(37,730)$
	$^4A_2(24,000)$
$^4T_1(24,038)$	^4E (23,000)
	^4E (16,750)
$^4T_2(16,180)$	$^4A_1(15,860)$
$^4A_2$	$^4A_2$
O_h	D_3
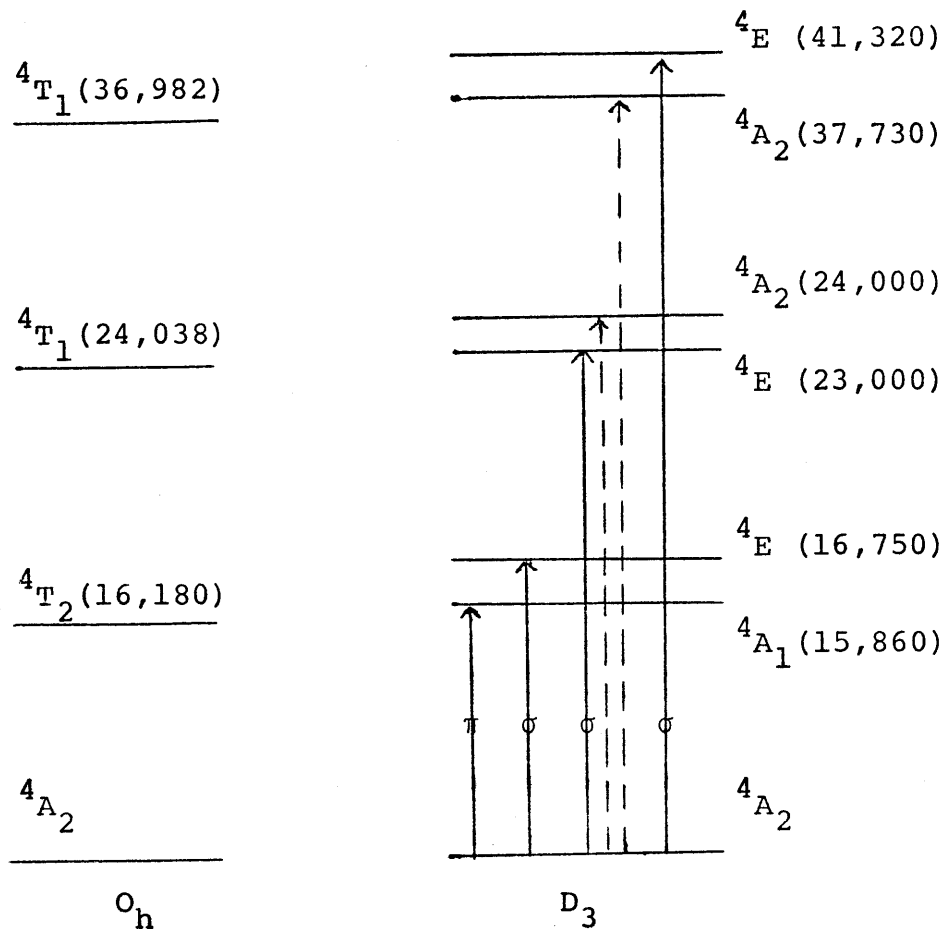
Considering site symmetry D_3, the only symmetry-allowed transitions are $^4A_2 \rightarrow ^4A_1$ (E ∥ C) and three $^4A_2 \rightarrow ^4E$ (E⊥C) transitions. Since the $^4A_2 \rightarrow ^4A_2$ transitions are not symmetry-allowed in either polarization, Wood invoked vibronic coupling to explain the presence of bands in the E ∥ C polarization at 24,000 cm^{-1} and 37,730 cm^{-1}.

The spin-forbidden bands observed by Wood (1965) were a $^4A_2 \rightarrow ^4E$ doublet at 14,686 cm^{-1} and 14,624 cm^{-1} (E ∥ C and E⊥C) a $^4A_2 \rightarrow ^4T_2$ singlet at 21,037 cm^{-1} (E⊥C) and the $^4A_2 \rightarrow ^2T_1$ transition which "appears as a group of at least five diffuse bands near 15,140 cm^{-1}" (E ∥ C and E⊥C).

Wood (1965) also reported the absorption spectra of emerald at 77K. He noted "little change in absorption intensity as the temperature is changed from 300° to 77K." In Figure 2 of Wood (1965) we observe that, while for the most part there was little intensity change in the bands which are symmetry-allowed, the spin-allowed band exhibiting the greatest intensity loss with decreased temperature was the $^4A_2 \to {}^4A_2$ (E ∥ C) which is symmetry-forbidden and must derive its intensity from vibronic coupling. The intensities of the spin-forbidden bands increase with decreased temperature.

Results

The polarized absorption spectra of a beryl containing 0.10 wt.% Cr_2O_3 were measured at five temperatures in the region 325-850 nm. The room temperature spectra are very similar to those presented by Wood (1965).

The E ∥ C spectra at 20C and 100C were fit to five Gaussian bands (Figure 7). The asymmetry of the low energy spin-allowed band is pronounced. Attempts to fit the absorption feature to a single band were unsuccessful. Since the fitting program is unable to accomodate skew in the band shape, the absorption feature was fit to a doublet. The necessity of fitting a doublet to this absorption feature makes comparison of band positions and widths difficult. As the bands broaden with temperature, the degree of overlap of the "doublet" increases until the overlap is too great to achieve convergence of the spectral parameters and therefore, at 390C, the width of the low energy band was constrained.
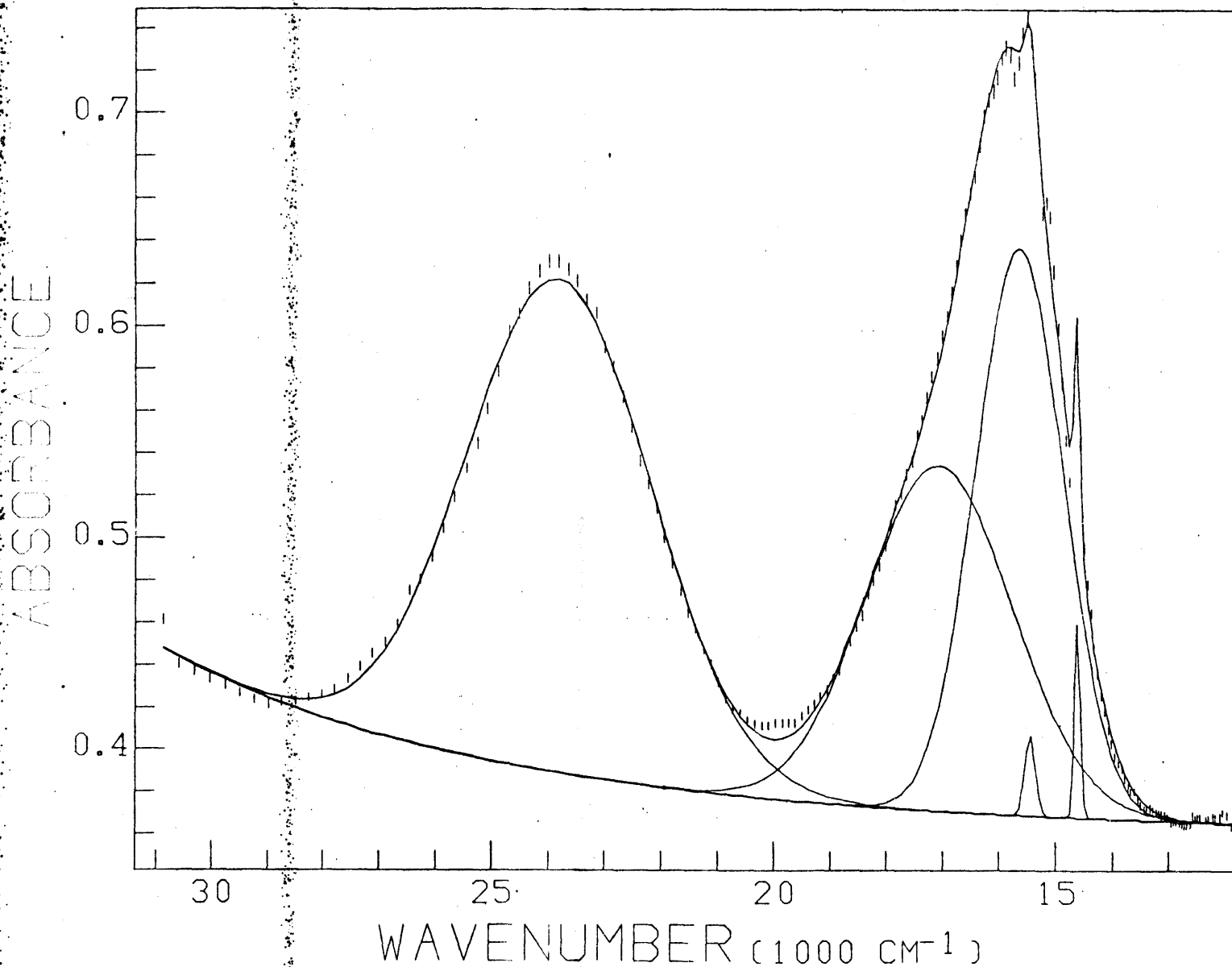
Figure 7. 20C spectrum of Cr^{3+}-beryl (E||c), computer fit

The spin-forbidden bands rapidly decrease in intensity
with temperature. Above 100C only the sharpest, most intense
band, $^4A_2 \rightarrow {}^4E$, was fit. To obtain a good visual fit of the
band, it was necessary to constrain the width of the band to
nearly the room temperature value in the high temperature
spectra. The band positions (E), widths (W), maximum extinction
coefficients (I) and integrated intensities (A) are reported
in Table 4.

The high energy band of the $E \perp C$ spectra was also
asymmetric, especially at low temperatures. The $E \perp C$ spectra
at 20C and 100C were fit to two peaks in this region (Figure 8).
An adequate fit to the absorption envelope can be achieved
with only a single band for the spectra obtained above 100C.
The spin-forbidden bands were not intense enough to permit
computer fitting, but peak positions determined from the original
spectra are reported along with the computer analyzed peak
parameters in Table 5.

The instrumental noise during the recording of the 390C
spectra was too great in the infrared region (700-850nm) to
allow measurement. Since the width and intensity parameters
are highly dependent on the baseline and the baseline
uncertainty increases dramatically when the spectra measurement
ends while still recording an absorption band, the discussion
will deal only with the 20C to 300C spectra.

The spin-allowed absorption bands in Cr-emerald all
shifted to lower energy by 260 to 410 cm^{-1} as temperature
increased from 20C to 300C (Figures 9 and 10). The band

Table 4

Cr-beryl (E ∥ C) Absorption Spectra Parameters

	20C	100C	200C	300C	390C
baseline (abs)	0.3528(c)	0.3739(4)	0.5103(c)	0.644(3)	0.640(c)
a (abs)	0.0089(4)	0.0000025(6)	0.0000018(c)	0.000009(2)	0.000008(c)
b (cm^{-2})	0.00249(5)	0.0116(3)	0.013(c)	0.0119(2)	0.0127(c)

$^4A_2 \rightarrow {}^4A_2(T_1)$

	20C	100C	200C	300C	390C
E (nm)	420	421	423	426	427
E (1000 cm^{-1})	23.813(6)	23.736(7)	23.657(7)	23.466(10)	23.445(10)
W (1000 cm^{-1})	3.87(2)	4.31(2)	4.59(2)	4.85(3)	4.99(3)
I (cm^{-1})	1.141(5)	1.333(6)	1.555(6)	1.851(14)	1.98(7)
A (1000 cm^{-2})	4.70(3)	6.11(2)	7.59(3)	9.56(10)	10.54(5)

$^4A_2 \rightarrow {}^4A_1(T_2)$

	20C	100C	200C	300C	390C
E (nm)	586	584	587	593	617
E (1000 cm^{-1})	17.06(8)	17.12(13)	17.02(20)	16.87(40)	16.2(4)
W (1000 cm^{-1})	3.05(9)	3.16(13)	3.33(19)	3.98(37)	4.4(4)
I (cm^{-1})	0.80(3)	0.79(5)	0.78(7)	0.81(15)	0.73(8)
A (1000 cm^{-2})	2.59(17)	2.66(26)	2.78(40)	3.42(96)	3.5(7)
E (nm)	640	643	649	654	659
E (1000 cm^{-1})	15.634(8)	15.56(2)	15.41(3)	15.28(3)	15.16(12)
W (1000 cm^{-1})	1.83(3)	2.04(4)	2.28(7)	2.65(15)	3.11(c)
I (cm^{-1})	1.31(6)	1.24(9)	1.12(13)	1.03(24)	0.78(16)
A (1000 cm^{-2})	2.55(16)	2.69(25)	2.71(39)	2.89(84)	2.6(5)

$^4A_2 \rightarrow {}^2T_1$

	20C	100C	200C	300C	390C
E (nm)	647	649			
E (1000 cm^{-1})	15.447(8)	15.406(12)	15.43	15.40	15.30
W (1000 cm^{-1})	0.21(2)	0.21(3)			
I (cm^{-1})	0.188(16)	0.119(15)			
A (1000 cm^{-2})	0.043(5)	0.026(4)			

$^4A_2 \rightarrow {}^2E$

	20C	100C	200C	300C	390C
E (nm)	685	686	688	691	691
E (1000 cm^{-1})	14.609(2)	14.574(2)	14.540(4)	14.483(8)	14.46(2)
W (1000 cm^{-1})	0.113(4)	0.146(6)	0.12(c)	0.12(c)	0.15(c)
I (cm^{-1})	0.457(15)	0.350(14)	0.238(16)	0.165(20)	0.09(2)
A (1000 cm^{-2})	0.058(2)	0.054(2)	0.030(2)	0.021(3)	0.014(4)
R^2	618/155	681/159	433/164	270/160	64/113
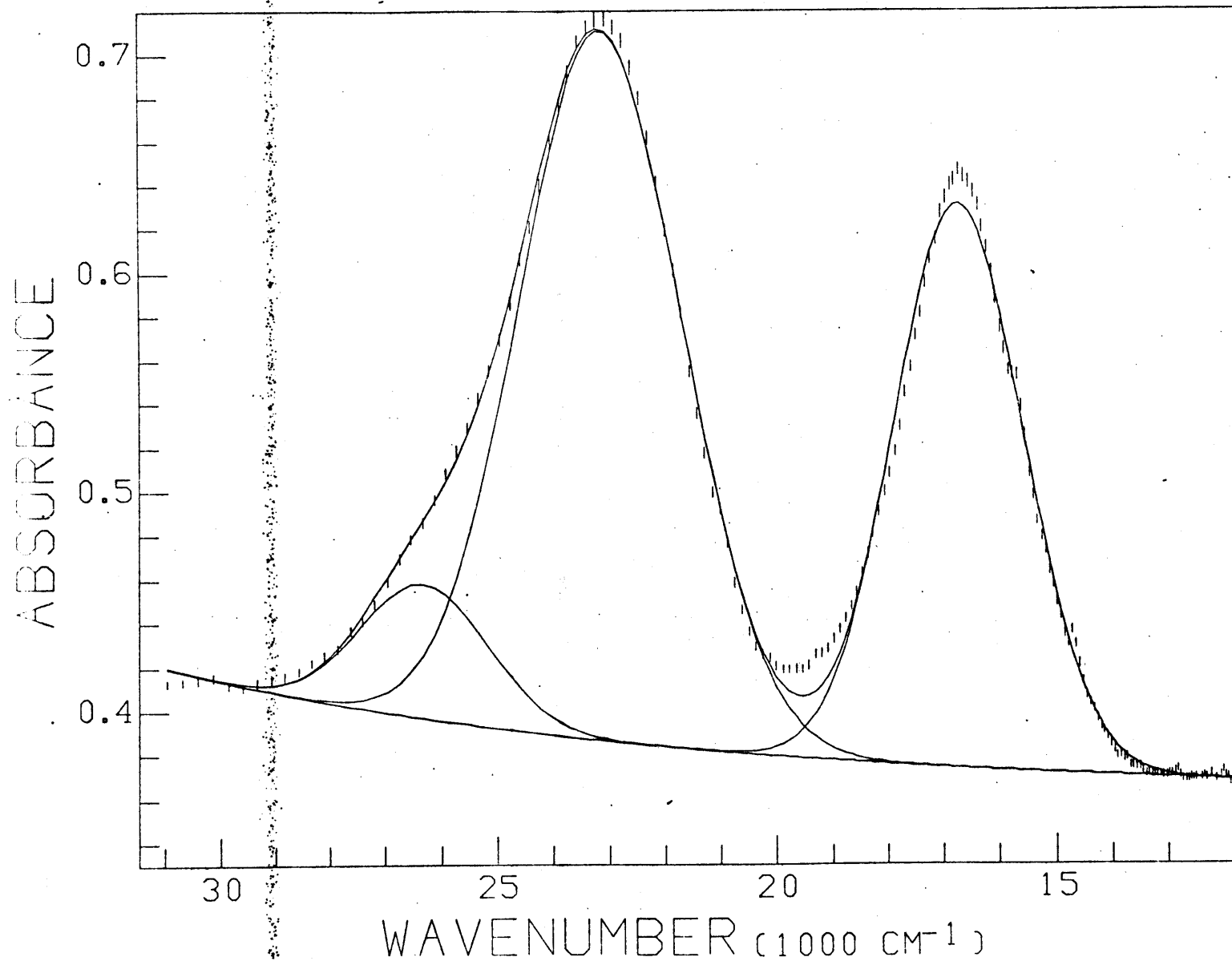
Figure 8.   20C spectrum of Cr^{3+}-beryl (E$\perp$c), computer fit

Table 5

Cr-beryl (E⊥C) Absorption Spectra Parameters

	20C	100C	200C	300C	390C
baseline (abs)	0.340(c)	0.365(c)	0.5068(5)	0.6405(7)	0.5705(c)
a (abs)	0.0241(3)	0.000169(c)	0.000018(3)	0.000034(4)	0.00089(11)
b (cm^{-2})	0.00125(2)	0.0065(c)	0.0102(2)	0.0099(1)	0.0073(1)
$^4A_2 \rightarrow ^4E(T_1)$					
E (nm)	380	374			
E $(1000\ cm^{-1})$	26.30(6)	26.70(5)			
W $(1000\ cm^{-1})$	2.67(10)	2.48(9)			
I (cm^{-1})	0.300(9)	0.230(8)			
A $(1000\ cm^{-2})$	0.85(5)	0.61(3)			
E (nm)	432	432	431	433	437
E $(1000\ cm^{-1})$	23.13(1)	23.12(1)	23.187(7)	23.077(8)	23.832(11)
W $(1000\ cm^{-1})$	3.41(2)	4.01(2)	4.46(2)	4.92(2)	5.72(4)
I (cm^{-1})	1.587(6)	1.686(5)	1.684(6)	1.820(7)	2.457(10)
A $(1000\ cm^{-2})$	5.76(5)	7.20(4)	7.99(3)	9.54(5)	14.97(14)
$^4A_2 \rightarrow ^4E(T_2)$					
E (nm)	598	600	607	614	629
E $(1000\ cm^{-1})$	16.717(3)	16.671(3)	16.473(5)	16.284(6)	15.889(9)
W $(1000\ cm^{-1})$	2.706(9)	2.916(8)	3.004(13)	3.176(17)	4.373(33)
I (cm^{-1})	1.261(4)	1.318(4)	1.190(5)	1.324(5)	1.826(5)
A $(1000\ cm^{-2})$	3.63(1)	4.09(1)	3.80(2)	4.48(3)	8.50(6)
R^2	1087/163	876/158	624/162	260/164	150/114
$^4A_2 \rightarrow ^2T$	15.71	15.67	15.67	15.64	
$^4A_2 \rightarrow ^2E$	14.70	14.64	14.64	14.62	14.70
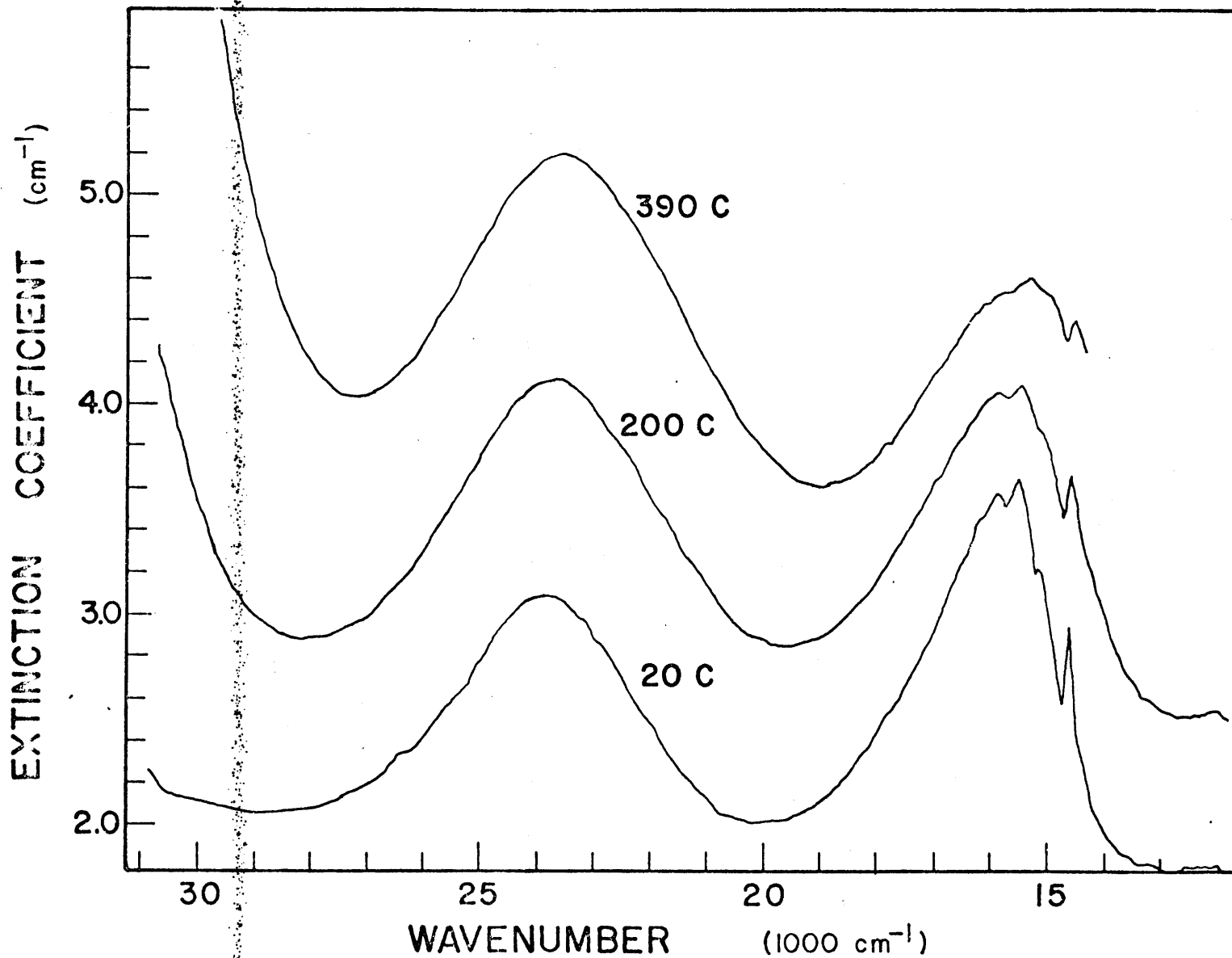
Figure 9. Absorption spectra of Cr^{3+}-beryl (E||c) at 20C, 200C, and 400C
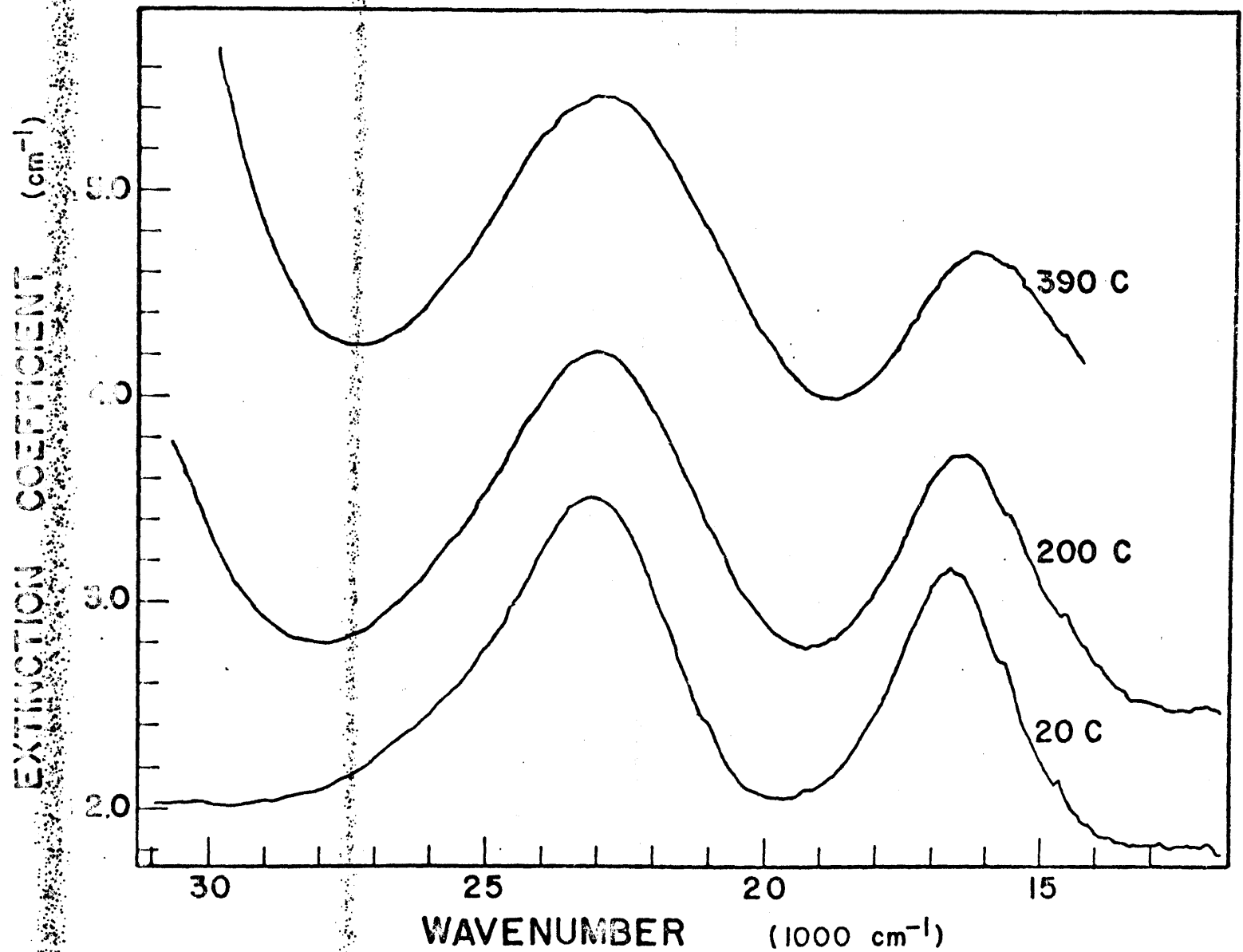
Figure 10. Absorption spectra of Cr^{3+}-beryl ($E \perp c$) at 20C, 200C, and 400C

widths increased approximately 25%, while the integrated intensities increases 25-125% over the same temperature range.

The $^4A_2 \rightarrow {}^4A_2(T_1)$ band (E ∥ C) shows the largest increase in intensity (4700 cm^{-2} to 10,500 cm^{-2}, 124%). This band is the only one which is symmetry-forbidden and vibronic coupling must be invoked to explain the absorption intensity. The large temperature dependence of the intensity of this band, as measured here and observed in the 77K spectra of Wood (1965), indicates that a major factor contributing to the change in intensity of absorption bands with temperature is the population of the vibrational levels of the cation.

The spin-forbidden absorption band $^4A_2 \rightarrow {}^2E$ also shifted to lower energy by 150 cm^{-1} as the temperature increased from 20C to 300C. The extinction coefficient maximum (peak height) decreased to approximately one-fifth the room temperature value.

3. Chrome diopside

Cr^{3+} occupies the distorted octahedral Ml site in diopside. The polarized visible-near infrared absorption spectra of chrome diopside (Mao et al., 1972; Schmetzer and Medenbach, 1974; and Boksha et al., 1974) show three prominent, broad bands. The band at 9400 cm^{-1} is attributed to Fe^{2+} on the Ml site, while the bands at 14,810 cm^{-1} and 21,970 cm^{-1} are due to the $^4A_2 \rightarrow {}^4T_2$ and $^4A_2 \rightarrow {}^4T_1$ transitions of Cr^{3+}, respectively. Narrow bands at 14,610 and 15,240 cm^{-1} are attributed to the spin-forbidden Cr^{3+} transitions $^4A_4 \rightarrow {}^2E$ and $^4A_4 \rightarrow {}^2T_2$, respectively (Boksha et al., 1974).

No attempt has been made to assign the absorption spectra to transitions arising from splitting of the $^4T_1$ and $^4T_2$ terms by the actual site symmetry of C_2. The polarized absorption spectra of Mao et al. (1972) show differences in the energy of the peak maxima in the different polarizations of the high energy $^4A_2 \rightarrow {}^4T_1$ bands and distinct asymmetry of the band possibly due to two highly overlapped bands in the β and γ polarizations. This indicates splitting of the $^4T_1$ state. However assignment of the spectra may not be possible due to the high degree of overlap of the bands and the many symmetry-allowed transitions in C_2 symmetry.

The crystal structure of diopside has been determined at various temperatures up to 1000C (Cameron et al., 1973). In general, the Si-O bond lengths do not increase with temperature while the mean M-O distances for both the

6-coordinated (M1) and 8-corrdinated (M2) sites show relatively large increases. Mean M1-O distance and the volume of the M1 octahedron increase linearly with increased temperature. The O-M1-O angles change less than two degrees over the temperature range measured (20-1000C) and less than one degree to 400C. Change in distortion of the M1 site as measured by the increase in quadratic elongation or the variance of octahedral angles (Robinson et al., 1971) is slight (less than 0.2% and 6%, respectively).

Results

The polarized absorption spectra of a diopside crystal containing 1.34 wt. % Cr_2O_3 and 2.04 wt. % FeO were recorded at five temperatures from 20C to 390C in the region 320nm to 850nm. Since the object of the study was to observe the temperature dependence of the Cr^{3+} bands, the band at 9400 cm^{-1} which has been attributed to Fe^{2+} was not measured. The α- and γ-polarized spectra (Figures 11 and 12) were fit to two bands at 22,100 cm^{-1} and 15,200 cm^{-1}. Spectral parameters are reported in Tables 6 and 7. A small sharp band at 14,500 cm^{-1} was observed in both the α and γ spectra but was not fit because of its small intensity. Three broad absorption bands were observed in the β-polarized spectra on a strong absorption edge (Figure 13). The band at ~26,000 cm^{-1}, which is clearly present at 20C, becomes much less pronounced at 400C (Figure 14). The band may be due to the splitting of the $^4T_1$ state by the C_2 site
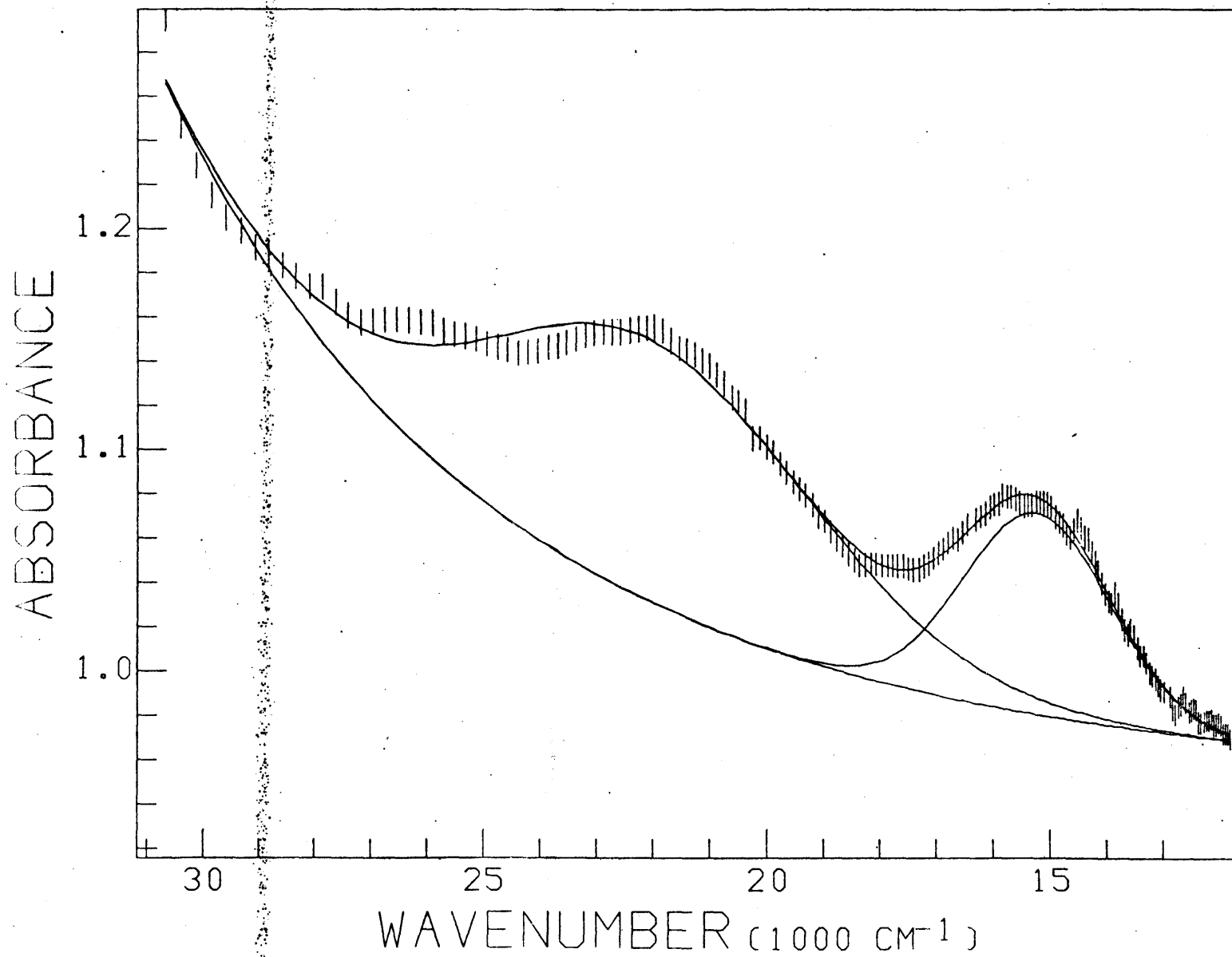
Figure 11. 20C spectrum of Cr^{3+}-diopside (α), computer fit
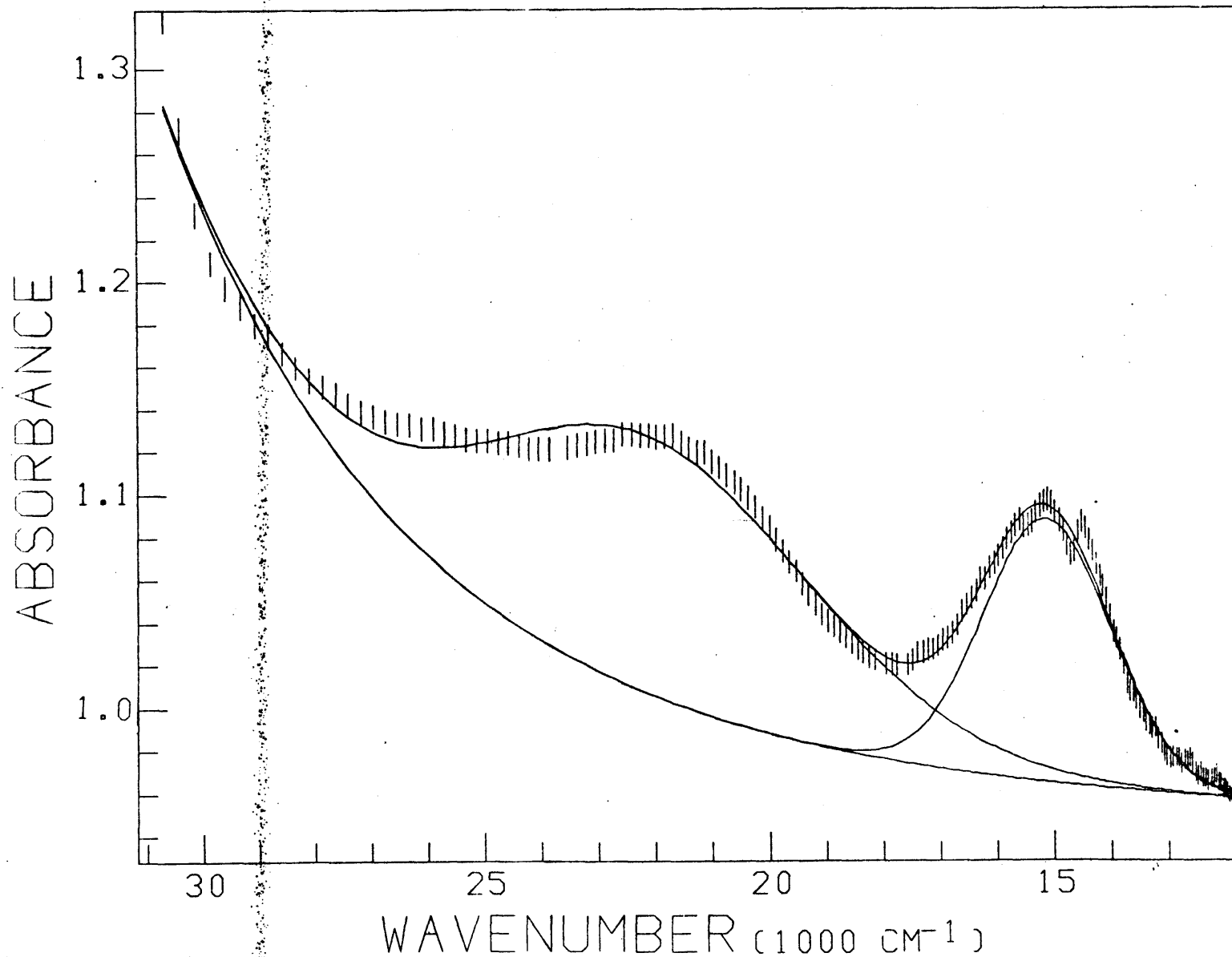
Figure 12. 20C spectrum of Cr^{3+}-diopside (γ), computer fit

58

Table 6

Cr-diopside (α) Absorption Spectra Parameters

	20C	100C	200C	300C	400C
baseline (abs)	0.9254(c)	0.960(c)	1.270(c)	1.3278(c)	1.400(c)
a (abs)	0.0305(14)	0.0065(10)	0.0027(7)	0.00054(16)	0.00054(14)
b (cm^{-2})	0.00256(5)	0.00415(17)	0.00511(29)	0.00711(31)	0.00727(27)
$^4A_2 \rightarrow {}^4T_1$					
E (nm)	452	448	445	446	443
E ($1000\ cm^{-1}$)	22.12(5)	22.31(5)	22.34(7)	22.41(8)	22.56(8)
W ($1000\ cm^{-1}$)	6.90(14)	7.39(17)	7.64(22)	8.60(26)	8.47(21)
I (cm^{-1})	4.88(11)	5.76(16)	6.91(19)	8.30(13)	8.23(13)
A ($1000\ cm^{-1}$)	35.9(12)	45.3(21)	56.1(28)	76.0(29)	74.2(26)
$^4A_2 \rightarrow {}^4T_2$					
E (nm)	657	663	664	672	661
E ($1000\ cm^{-1}$)	15.23(3)	15.08(3)	15.07(3)	14.88(8)	15.14(5)
W ($1000\ cm^{-1}$)	3.05(7)	3.07(7)	3.00(7)	3.36(24)	2.50(14)
I (cm^{-1})	3.75(7)	3.55(7)	3.71(8)	3.94(11)	3.44(10)
A ($1000\ cm^{-1}$)	12.2(4)	11.6(4)	1.18(4)	14.1(12)	9.2(6)
R^2	137/166	99/167	30/159	23/99	20/112

Table 7

Cr-diopside (γ) Absorption Spectra Parameters

	20C	100C	205C	300C	400C
baseline (abs)	0.938(4)	0.961(2)	1.022(3)	1.150(c)	1.30(c)
a (abs)	0.012(3)	0.0028(7)	0.0004(1)	0.00021(7)	0.0008(4)
b (cm^{-2})	0.0036(2)	0.0051(2)	0.0074(3)	0.0084(4)	0.0072(5)
$^4A_2 \rightarrow {^4T_1}$					
E (nm)	451	447	442	443	453
E (1000 cm^{-1})	22.16(7)	22.39(7)	22.63(8)	22.52(9)	22.07(14)
W (1000 cm^{-1})	6.87(20)	7.36(18)	9.13(20)	11.85(34)	14.08(60)
I (cm^{-1})	4.98(16)	5.81(14)	8.11(15)	13.39(15)	20.54(30)
A (1000 cm^{-2})	36.4(21)	45.5(20)	78.8(28)	168.8(57)	307.8(100)
$^4A_2 \rightarrow {^4T_1}$					
E (nm)	661	668	677	690	697
E (1000 cm^{-1})	15.13(2)	14.96(2)	14.77(2)	14.49(8)	14.35(11)
W (1000 cm^{-1})	2.64(4)	2.76(5)	2.99(7)	3.47(19)	3.69(25)
I (cm^{-1})	5.07(7)	4.93(8)	5.39(10)	7.18(24)	8.92(54)
A (1000 cm^{-2})	14.2(3)	14.5(4)	17.2(6)	26.6(22)	35.0(43)
R^2	243/163	160/164	162/162	47/112	9/112

60
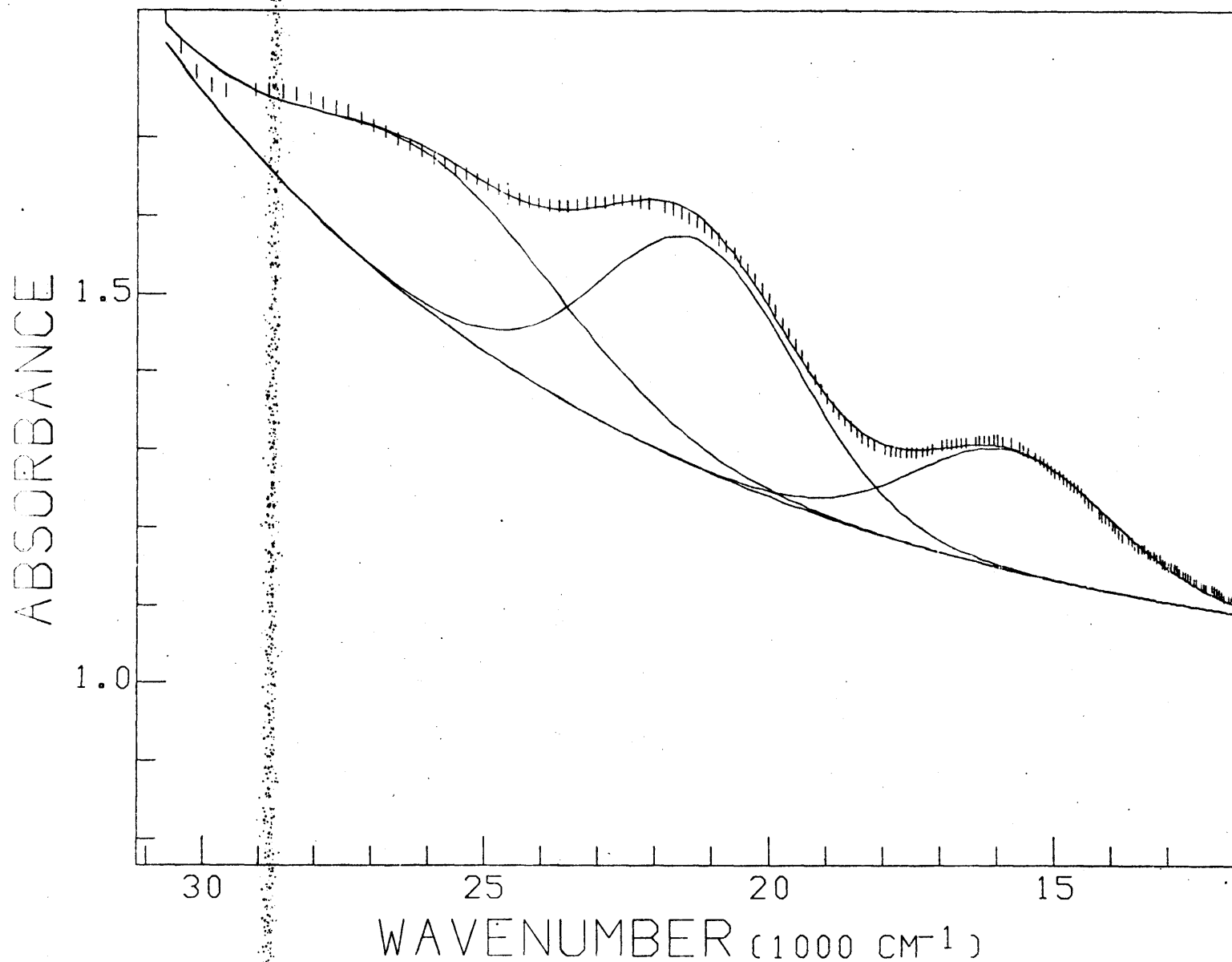
Figure 13.   20C spectrum of Cr^{3+}-diopside (β), computer fit
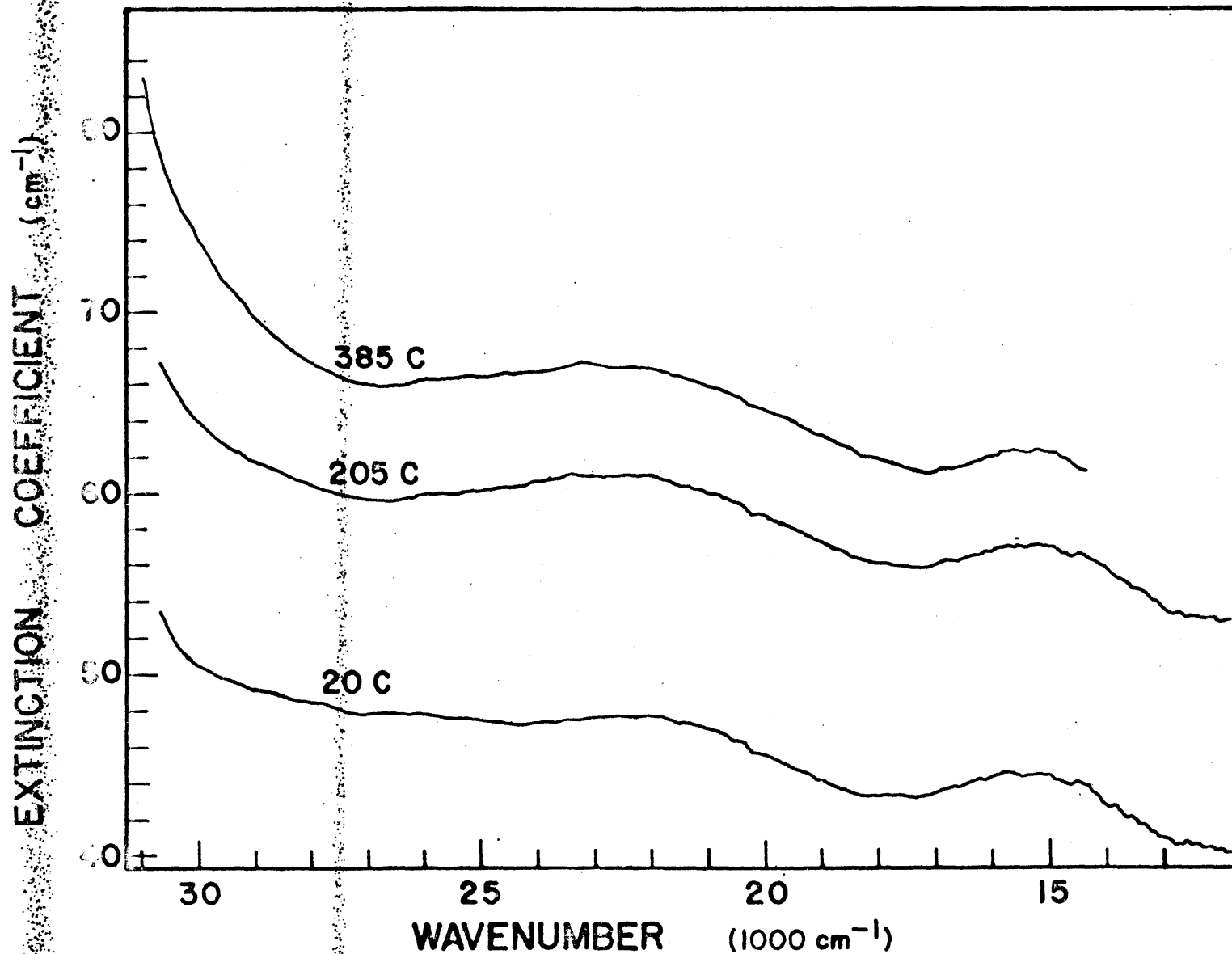
Figure 14. Absorption spectra of Cr^{3+}-diopside (α) at 20C, 200C, and 400C

symmetry or to an inconsistancy of the baseline which has
a dramatic change in slope in this region. The spectral
parameters are reported in Table 8, but due to the difficulties
in interpretation, the β-polarized spectra will not be
discussed further.

The α- and γ-polarized spectra show very similar
temperature dependencies (Figures 15 and 16). The low
energy, $^4A_2 \rightarrow {}^4T_2$ band moves to lower energy by approximately
400 cm^{-1} and broadens 5 to 20% over the temperature range
20C to 400C. The high energy band moves to higher energy
with increased temperature. This departure from what was
observed in emerald and ruby is probably due to the larger
site occupied by Cr^{3+}.

Since it was not possible to measure the spectra in
the region 700 to 850nm at 300C and 400C, the fit parameters
have much higher uncertainties than is desirable. Both
Cr^{3+} bands are relatively weak as compared with the absorption
edge. This artificially broadens the bands and increases
their intensities as the accurate fitting of the baseline
assumes more importance. In particular the widths of the
high energy bands at 20C are 6900 cm^{-1} as compared to
approximately 4500 cm^{-1} as measured by Mao et al. (1972).
The degree of influence of the absorption edge in the visible
region spectra differs widely between samples as evidenced
by the published spectra, possibly due to differences in
the clarity of the samples or the concentration of iron.

Table 8

Cr-diopside (β) Absorption Spectra Parameters

	20C	100C	200C	300C	400C
baseline (abs)	0.775(c)	0.80(c)	0.87(c)	1.15(c)	1.28(c)
a (abs)	0.255(c)	0.255(c)	0.272(c)	0.0051(c)	0.0076(c)
b (cm^{-2})	0.0015(c)	0.0015(c)	0.0015(c)	0.0055(c)	0.005(c)
$^4A_2 \rightarrow {}^4T_1$					
E (nm)	387	387	407	373	382
E (1000 cm^{-1})	25.9(1)	25.8(2)	24.5(4)	26.8(1)	26.2(1)
W (1000 cm^{-1})	5.6(3)	4.8(3)	6.9(5)	4.8(4)	4.1(4)
I (cm^{-1})	7.8(2)	7.1(3)	12.5(8)	9.1(20)	6.6(15)
A (1000 cm^{-2})	46.(3)	36.(3)	92.	46.	29.(9)
E (nm)	471	469	485	464	467
E (1000 cm^{-1})	21.24(6)	21.32(8)	20.6(1)	21.5(2)	21.4(1)
W (1000 cm^{-1})	4.1(1)	4.6(2)	4.5(3)	8.2(6)	7.3(5)
I (cm^{-1})	11.4(4)	12.6(3)	11.7(19)	25.1(3)	19.9(2)
A (1000 cm^{-2})	50.(3)	26.(3)	56.	220.	155.
$^4A_2 \rightarrow {}^4T_2$					
E (nm)	636	636	641	668	659
E (1000 cm^{-1})	15.73(3)	15.72(4)	15.59(6)	14.97(5)	15.16(7)
W (1000 cm^{-1})	4.05(6)	3.94(6)	4.78(9)	4.1(3)	4.0(3)
I (cm^{-1})	6.03(7)	6.32(8)	10.0(1)	10.2(8)	7.5(6)
A (1000 cm^{-2})	26.0(5)	26.5(6)	51.(1)	45.(6)	32.(4)
R^2	132/153	138/163	40/154	51/113	117/117
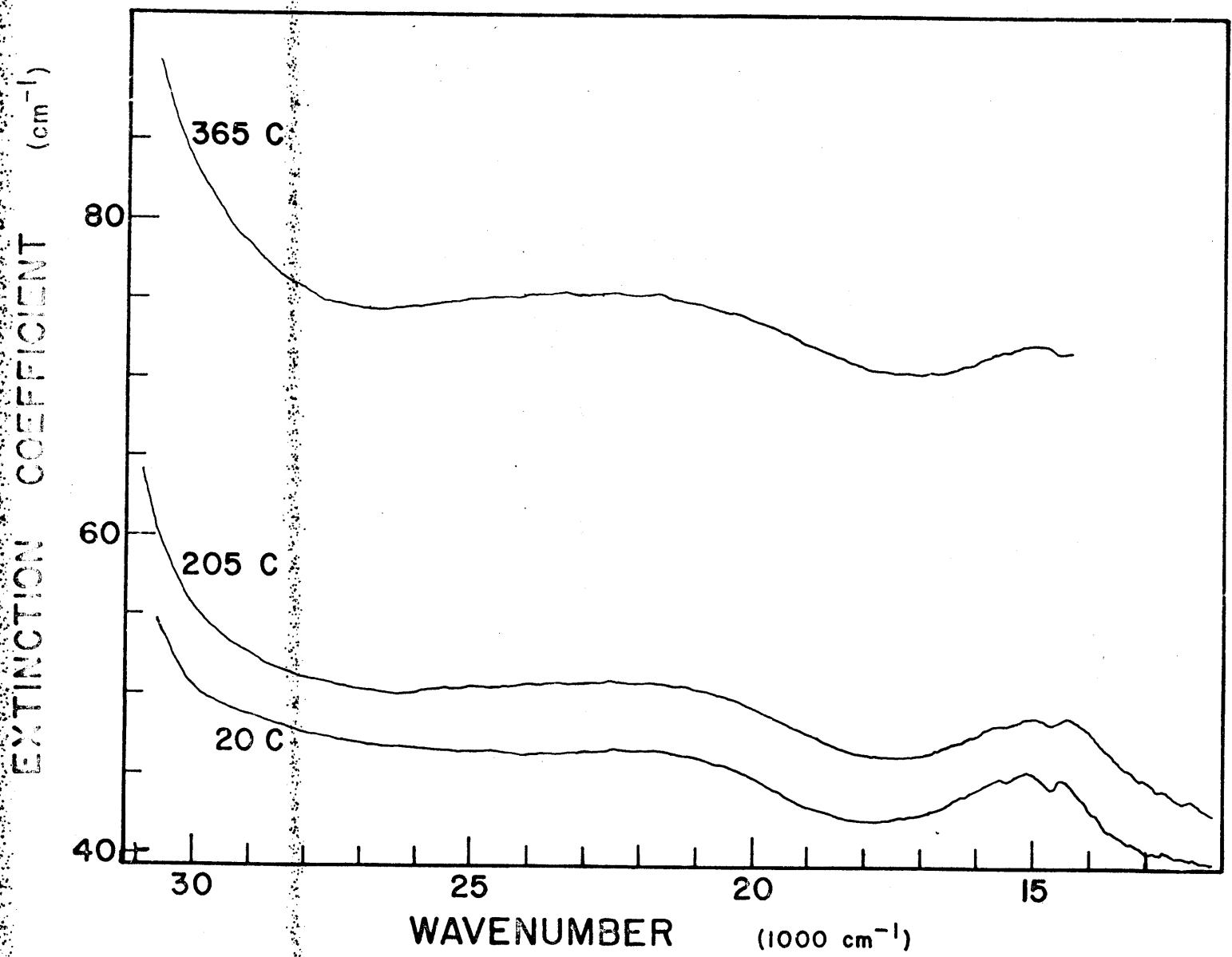
Figure 15.   Absorption spectra of Cr^{3+}-diopside (γ) at 20C, 200C, and 400C
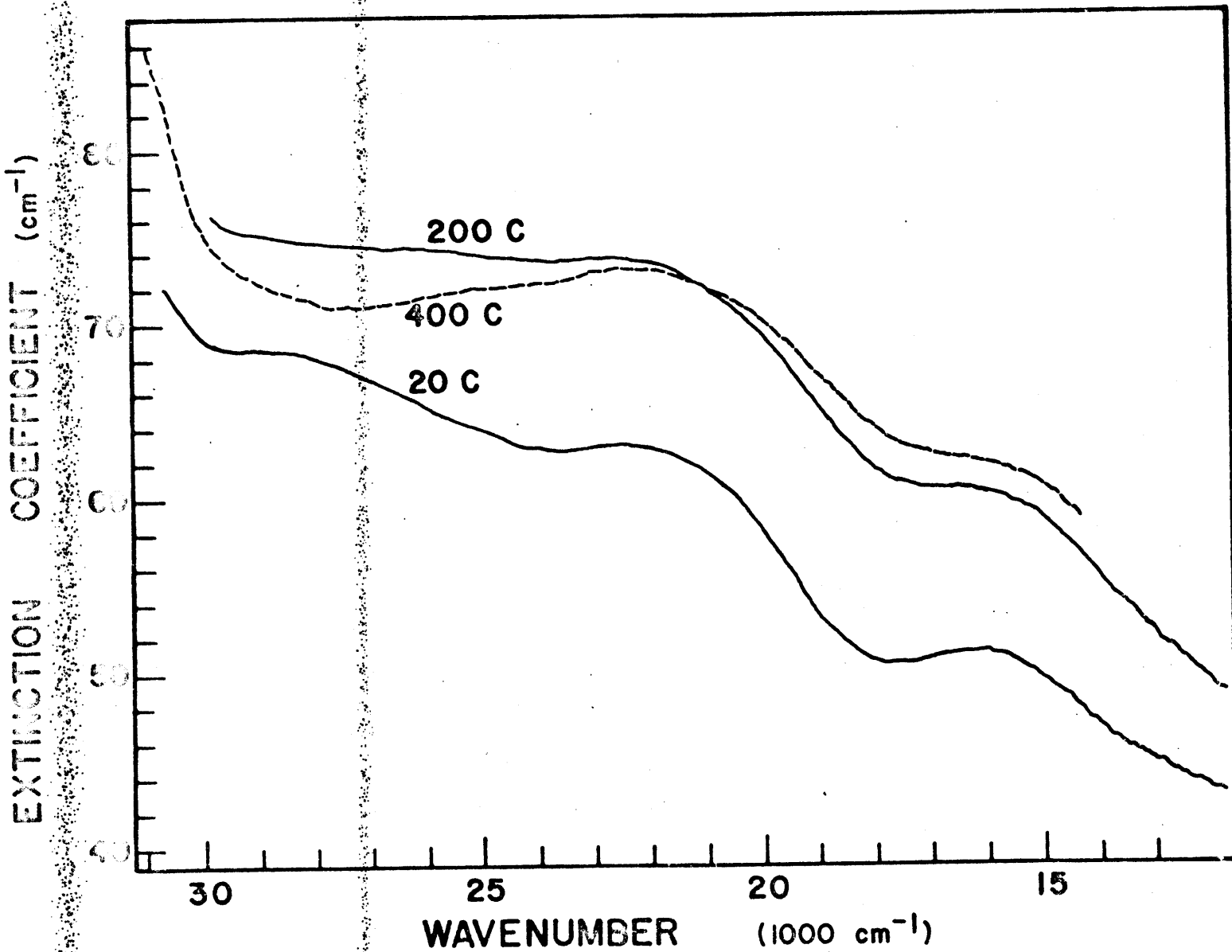
Figure 16. Absorption spectra of Cr^{3+}-diopside (β) at 20C, 200C, and 400C

The intensities of the absorption bands also depend upon the accurate fitting of the absorption edge. As the high energy band broadens, the low energy limb of the band encroaches on the $^4A_2 \rightarrow {}^4T_2$ band. As a result the $^4A_2 \rightarrow {}^4T_2$ band in the α-polarized spectra showed a decrease in integrated intensity with temperature while the total intensity due to Cr^{3+} increased 80%. The drastic increase in intensity of the γ-polarized spectra probably reflects the lack of definition of the baseline more than the actual increase in Cr^{3+} absorption intensity.

4. Cr-Kyanite

The kyanite structure contains four crystallographically distinct distorted Al^{3+} octahedra with mean M-O idstances of 1.897Å to 1.918Å and variance of octahedra angles of 40.8 to 55.7°(Burnham, 1963). Langer and Seifert (1971) synthesized Cr^{3+}-bearing kyanite containing up to 25 mole % of the theoretical endmember Cr_2SiO_5, and concluded from x-ray powder data that Cr^{3+} occurs mainly in the Ml and M2 sites.

Langer and Abu-Eid (1977) reported the E ∥ C spectrum of a synthetic Cr^{3+}-bearing kyanite microcrystal $(Al_{1.7}Cr_{0.3}SiO_5)$. The spectrum exhibits three broad bands near 16,000, 24,100 and 29,900 cm^{-1}, with splitting of the 16,000 cm^{-1} band. Langer and Abu-Eid assigned the 16,000 cm^{-1} and 24,100 cm^{-1} bands to the $^4A_2 \rightarrow {}^4T_2$ and $^4A_2 \rightarrow {}^4T_1$ transitions of Cr^{3+}, respectively and attributed the splitting of the 16,000 cm^{-1} band to splitting of the $^4T_2$ state by the low symmetry of the Al sites or to absorption by Cr^{3+} in different Al sites. No definite assignment was made of the 29,900 cm^{-1} band. They speculated that it may be due to $^4A_2 \rightarrow {}^4T_1$ (P) band, but from the energy of the $^4A_2 \rightarrow {}^4T_1$ (F) band, the band at 29,900 cm^{-1} appears to be approximately 2000 cm^{-1} too low.

Langer (1976) reported the diffuse reflectance spectra of a suite of synthetic Cr^{3+}-bearing kyanites and identified bands due to the spin-forbidden $^4A_2 \rightarrow {}^2E$ and $^4A_2 \rightarrow {}^2T_1$ transitions at 14,100 cm^{-1} and 14,450 cm^{-1} respectively.

Results

A natural blue-green kyanite containing 0.65 wt.% Cr_2O_3 and 0.12 wt.% FeO was used to measure the polarized absorption spectra at four temperatures from 20C to 300C. Due to experimental difficulties, the spectra are not easy to interpret.

The β- and γ-polarized spectra were obtained using a single section cut parallel to the perfect (100) cleavage. Probably as a result of light scattering, the Cr^{3+} absorption bands appear as weak bands superimposed on a strong absorption edge (Figures 17 and 18). As was the case for the chromediopside, the fit of the absorption edge is critical to the determination of the spectral parameters. Since the function chosen for the absorption edge assumes that it is due to another, more intense Gaussian band in the ultraviolet, the function may not be a reasonable choice if the edge is due to light scattering. Also, as shown in Figure 19 the slope of the absorption edge changed radically during the recording of the 200C spectra in both the β- and γ-polarizations and then returned to approximately that of the lower temperature spectra at 300C. No explanation for this is forthcoming at this time. In the α-polarized spectra the absorption bands are clearly defined (Figure 20). However, the lack of a measured baseline hampered the fitting procedure somewhat. Fit spectral parameters are presented in Tables 9 to 11, and fit 20C spectra are presented in Figures 21 to 23. Overall, the kyanite spectra exhibit trends similar to those observed in the other Cr^{3+} spectra.
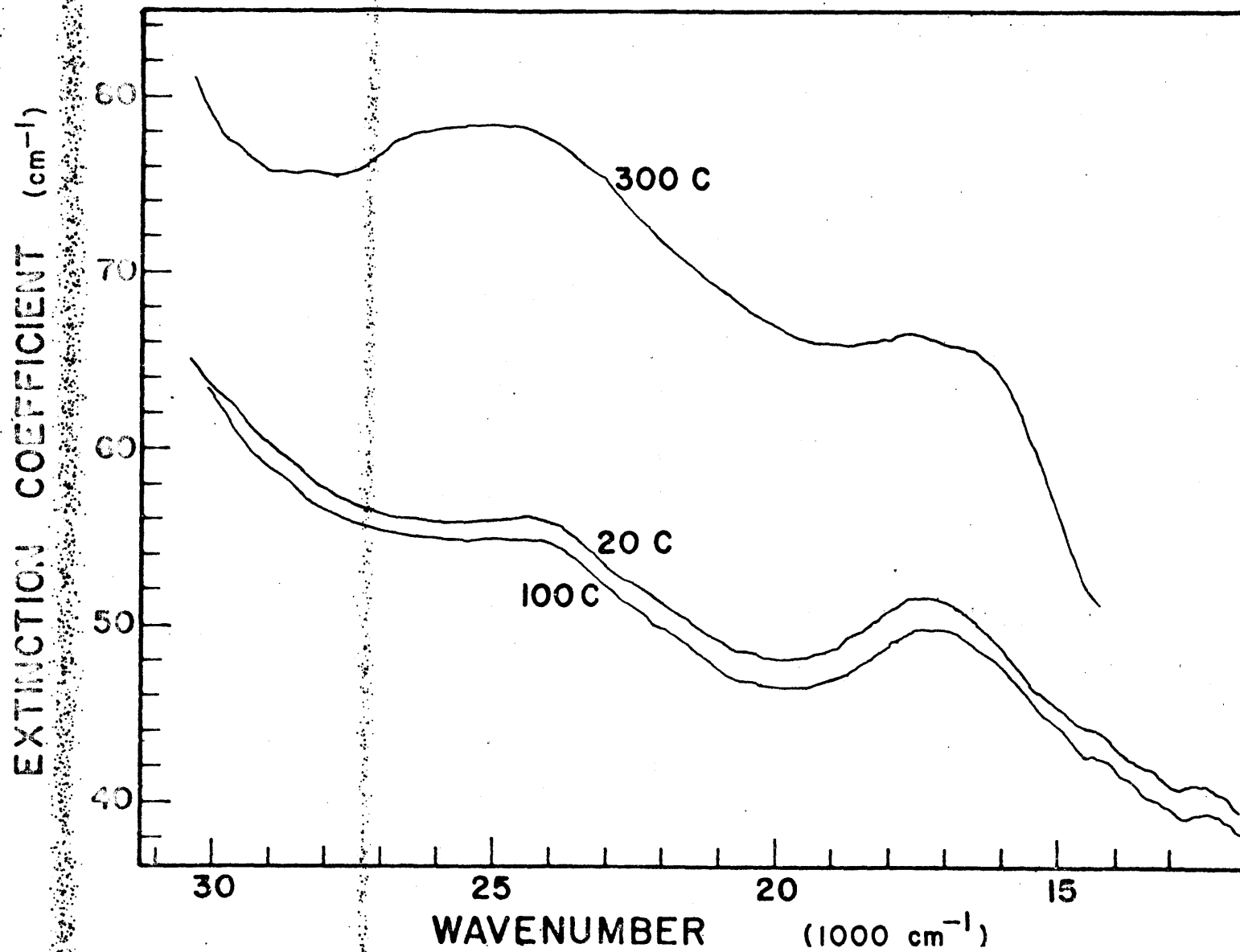
Figure 17. Absorption spectra of Cr^{3+}-kyanite (β) at 20C, 100C, and 300C
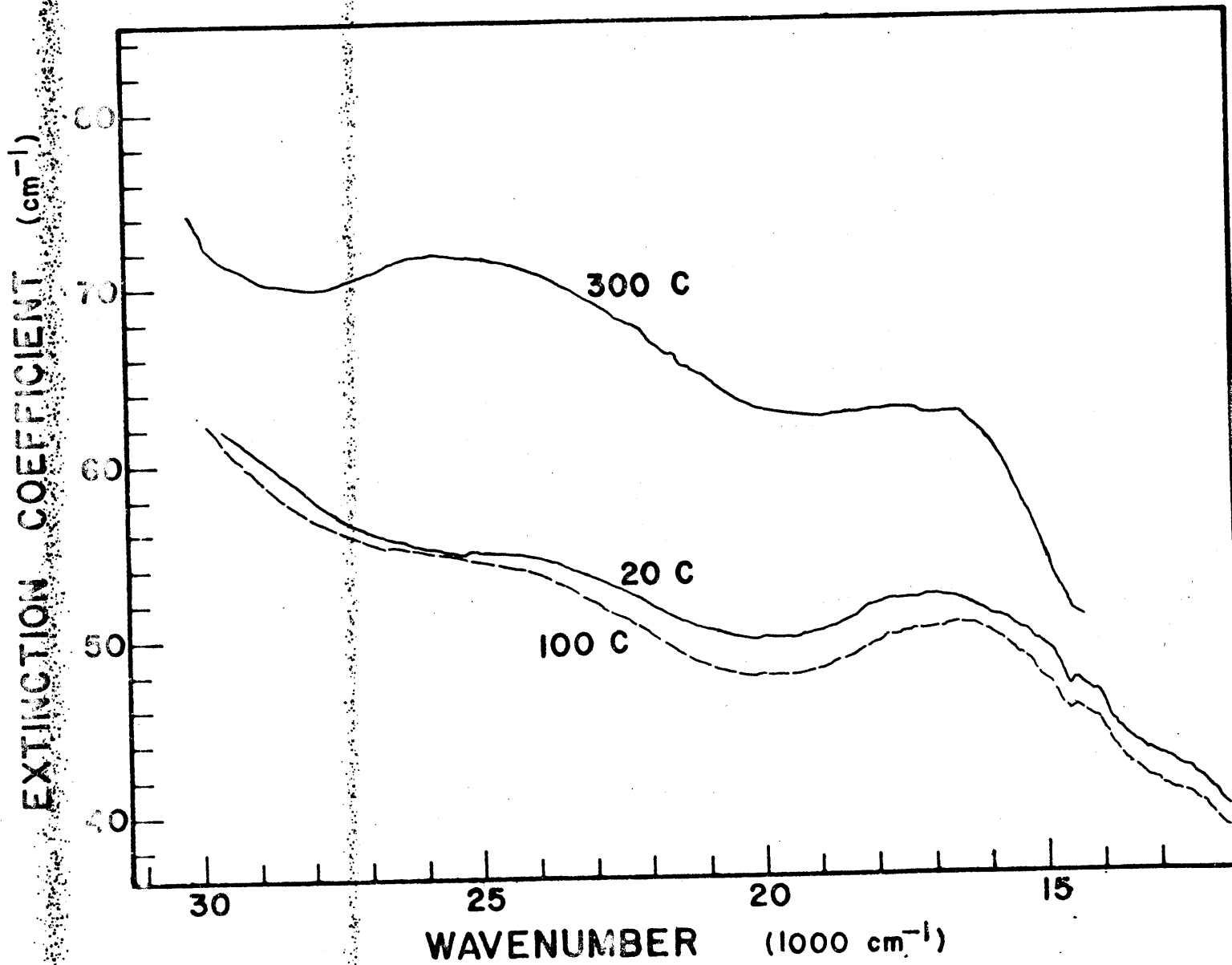
Figure 18. Absorption spectra of Cr^{3+}-kyanite (γ) at 20C, 100C, and 300C
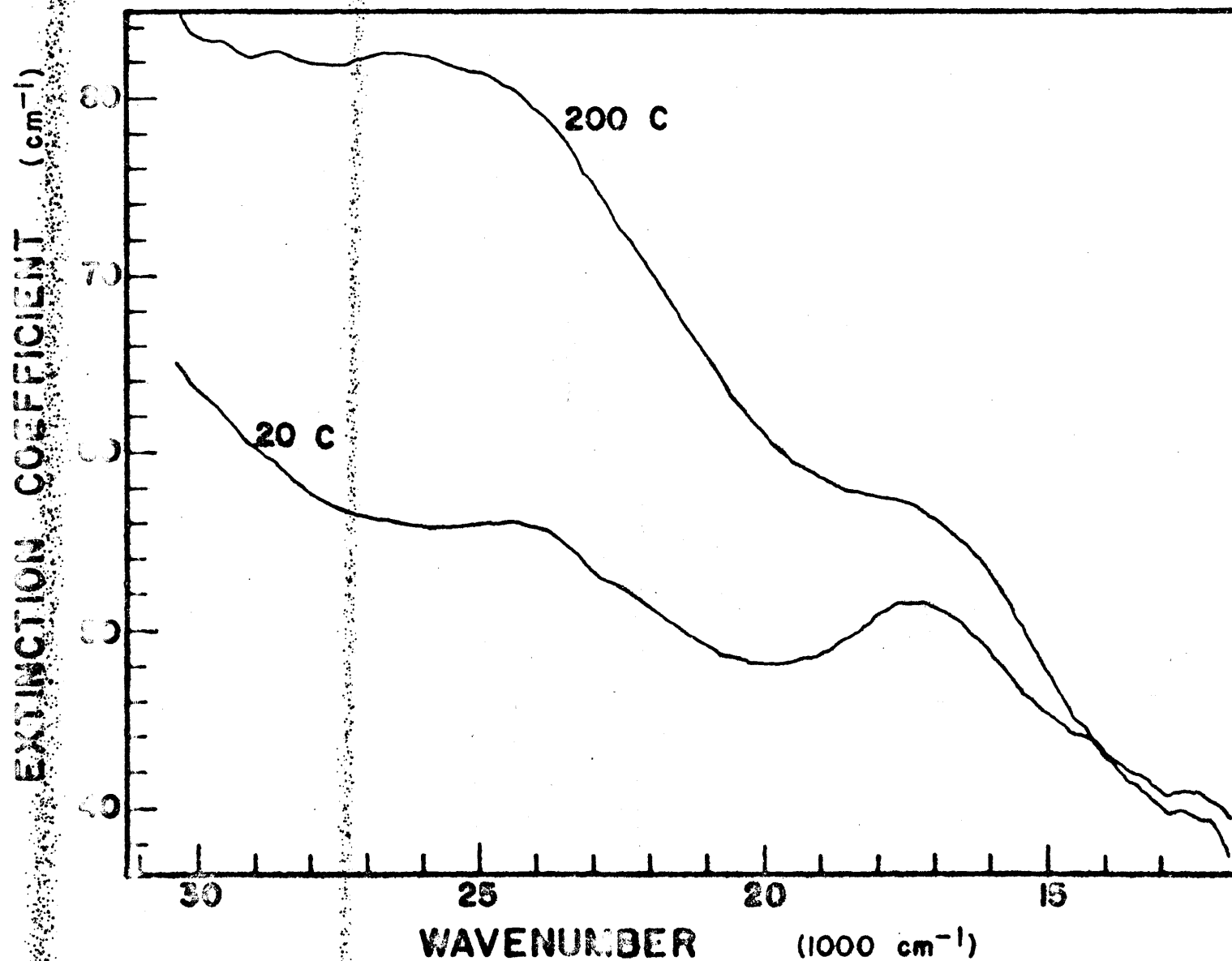
Figure 19. Absorption spectra of Cr^{3+}-kyanite (β) at 20C and 200C
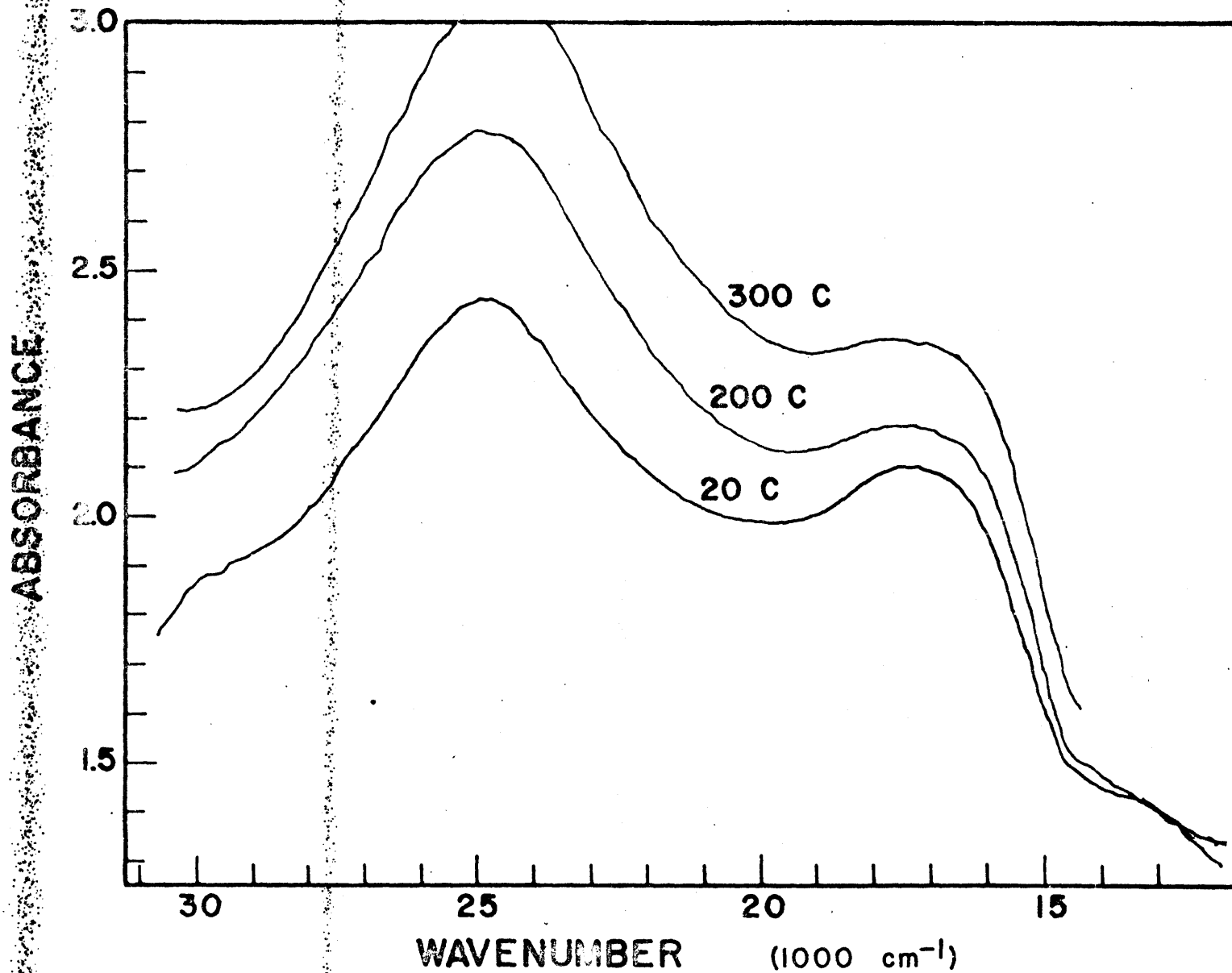
Figure 20.   Absorption spectra of Cr^{3+}-kyanite (α) at 20C, 200C, and 300C

Table 9

Cr-Kyanite (α) Absorption Spectral Parameters

	20C	100C	200C	300C
baseline (abs)	0.85(c)	0.85(c)	0.85(c)	0.95(c)
a (abs)	0.457(2)	0.482(3)	0.400(3)	0.2806(c)
b (cm^{-2})	0.00057(2)	0.00059(3)	0.00094(2)	0.00156(c)
$^4A_2 \rightarrow {}^4T_1$				
E (nm)	409	406	409	416
E (1000 cm^{-1})	24.44(2)	24.64(3)	24.45(2)	24.04(1)
W (1000 cm^{-1})	7.79(8)	8.30(10)	8.07(8)	6.92(3)
I (abs)	0.875(5)	0.919(8)	1.167(6)	1.369(4)
A (1000 abs/cm)	7.25(10)	8.12(16)	10.03(14)	10.08(4)
$^4A_2 \rightarrow {}^4T_2$				
E (nm)	581	586	586	583
E (1000 cm^{-1})	17.22(1)	17.06(1)	17.07(1)	17.15(1)
W (1000 cm^{-1})	3.79(2)	3.89(3)	4.05(3)	4.52(3)
I (abs)	0.662(4)	0.635(4)	0.721(4)	0.923(4)
A (1000 abs/cm)	2.67(3)	2.63(3)	3.11(3)	4.44(4)
R^2	1880/131	1550/130	2000/136	1560/91

74

Table 10

Cr-Kyanite (β) Absorption Spectral Parameters

	20C	100C	200C	300C
baseline (abs)	0.65(c)	0.68(c)	0.25(c)	0.80(c)
a (abs)	0.182(1)	0.124(1)	0.491(1)	0.143(c)
b (cm^{-2})	0.00154(1)	0.00188(1)	0.00120(1)	0.00207(c)
$^4A_2 \rightarrow {}^4T_1$				
E (nm)	423	421	413	429
E (1000 cm^{-1})	23.65(3)	23.74(3)	24.23(3)	23.32(2)
W (1000 cm^{-1})	4.40(8)	4.82(9)	8.45(12)	7.25(7)
I (cm^{-1})	5.5(1)	6.3(1)	22.8(3)	19.5(2)
A (1000 cm^{-2})	25.9(7)	32.5(8)	205.(4)	151.(2)
$^4A_2 \rightarrow {}^4T_2$				
E (nm)	585	589	595	591
E (1000 cm^{-1})	17.09(2)	16.97(2)	16.80(2)	16.93
W (1000 cm^{-1})	4.05(5)	4.09(5)	3.98(5)	4.02(4)
I (cm^{-1})	8.2(1)	8.3(1)	10.2(2)	15.7(2)
A (1000 cm^{-2})	35.3(6)	36.3(6)	43.(1)	67.(1)
χ^2	236/146	145/140	177/150	847/113

Table 11

Cr-Kyanite (γ) Absorption Spectral Parameters

	20C	100C	200C	300C
Baseline (abs)	0.64(7)	0.68(c)	0.25(c)	0.80(c)
a (abs)	0.16(6)	0.115(3)	0.485(2)	0.1676(c)
b (cm^{-2})	0.0017(3)	0.00197(3)	0.00116(1)	0.00173(c)
$^4A_2 \rightarrow {}^4T_1$				
E (nm)	431	425	408	433
E (1000 cm^{-1})	23.22(7)	23.55(5)	24.48(5)	23.09(3)
W (1000 cm^{-1})	5.1(3)	5.72(15)	8.8(2)	7.46(10)
I (cm^{-1})	5.4(6)	6.0(2)	19.1(3)	13.7(1)
A (1000 cm^{-2})	29.(5)	36.5(13)	179.(5)	109.(2)
$^4A_2 \rightarrow {}^4T_2$				
E (nm)	603	607	610	593
E (1000 cm^{-1})	16.58(3)	16.46(2)	16.40(3)	16.86(2)
W (1000 cm^{-1})	5.58(10)	5.08(8)	4.52(7)	3.78(5)
I (cm^{-1})	10.5(3)	10.1(1)	9.2(2)	11.8(2)
A (1000 cm^{-2})	62.(2)	54.4(15)	44.2(13)	47.7(10)
R^2	120/136	122/147	319/157	572/102
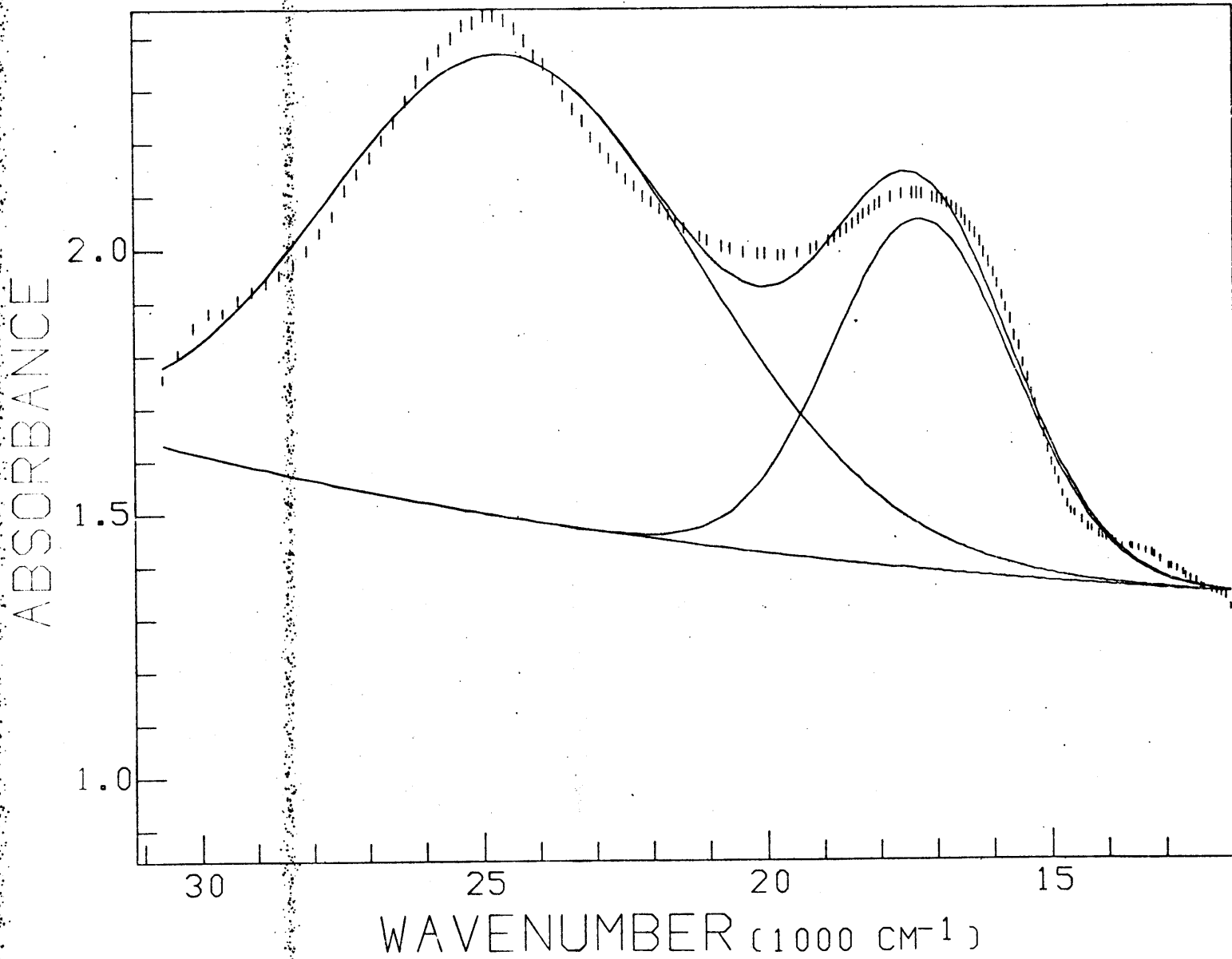
Figure 21.   20C spectrum of Cr^{3+}-kyanite (α), computer fit
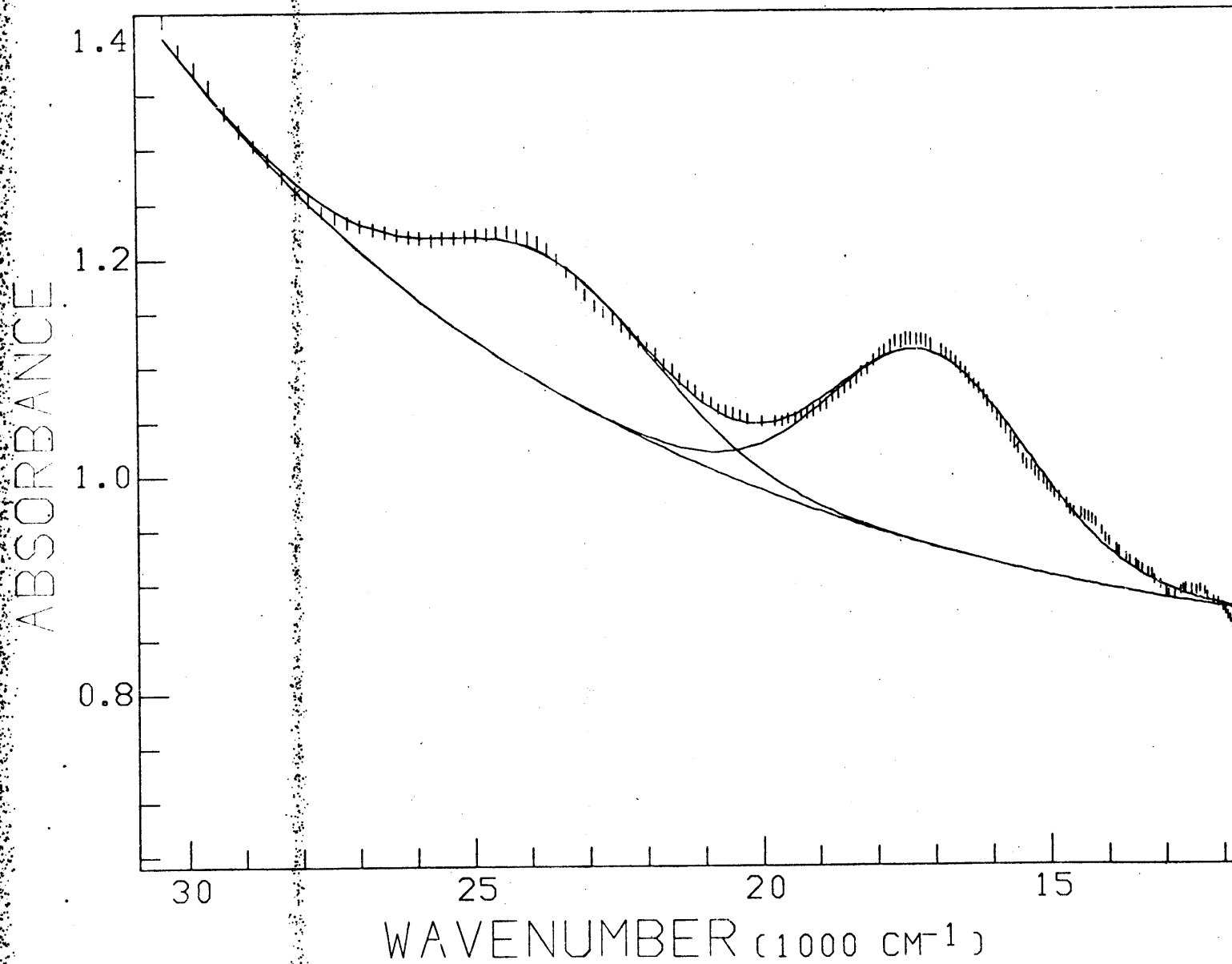
Figure 22.   20C spectrum of Cr^{3+}-kyanite (ß), computer fit
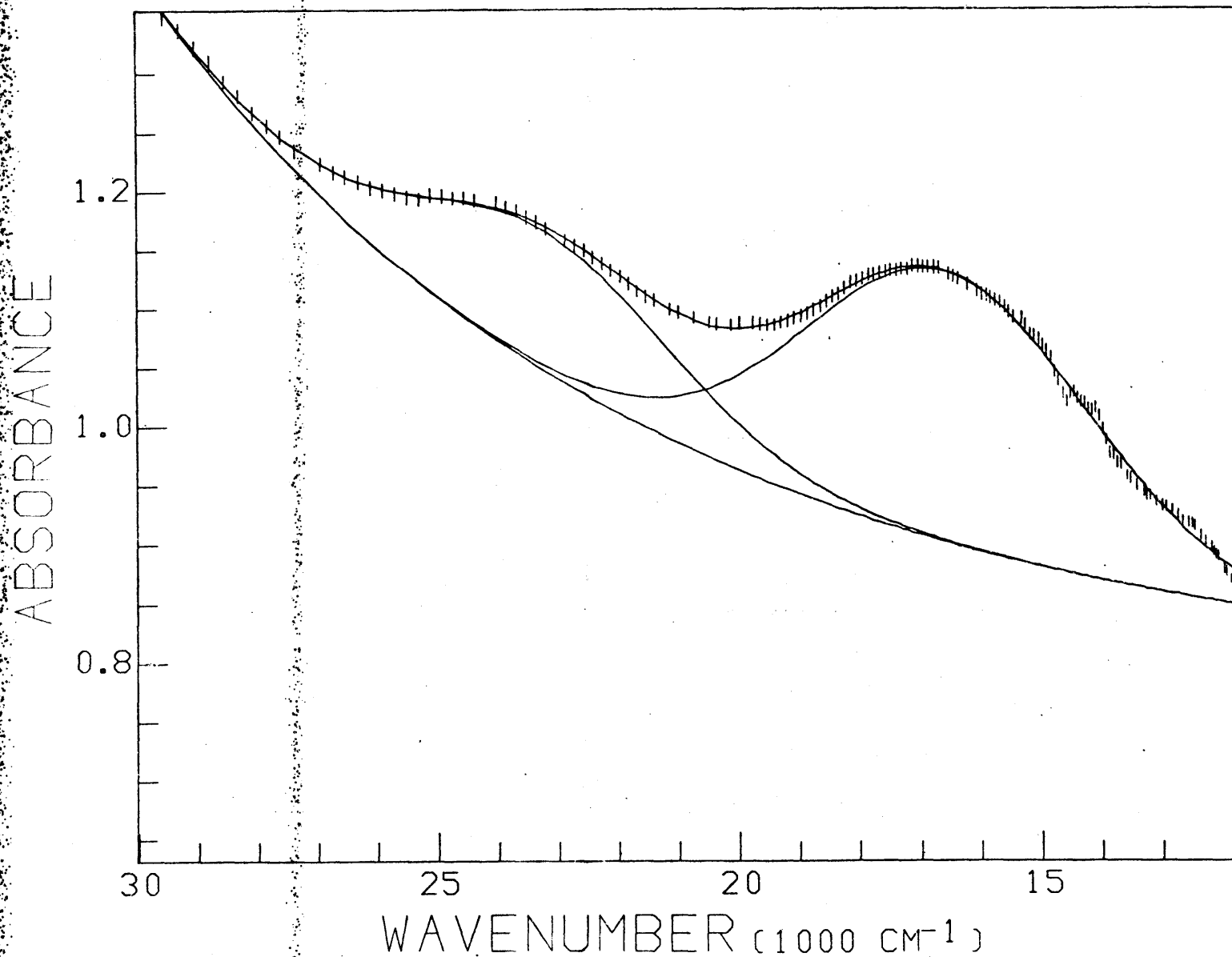
Figure 23. 20C spectrum of Cr^{3+}-kyanite (γ), computer fit

Both bands broaden and increase in integrated intensity, when the extreme breadth of the high energy band in the β- and γ-polarizations is taken into consideration. The bands shift to lower energy although the magnitude of the shifts and, therefore, the change in the B Racah parameter are uncertain.

Clearly the high temperature absorption spectra of Cr^{3+} in kyanite should be remeasured. Care must be taken to ensure the maximum optical clarity of the sample. Also, since the chosen function for the absorption edge does not appear to be adequate in this instance, another function may be required in order to fit the data.

CHAPTER 6

d^6-Minerals: Fe^{2+}

Fe^{2+} is commonly in solid solution with Mg^{2+} occupying distorted octahedral sites in minerals with mean metal-oxygen distances of 2.1 to 2.2Å. In a perfect octahedral site, the ^5D ground term of Fe^{2+} is split into two crystal field states, $^5T_{2g}$ (ground state) and ^5E_g. Since Fe^{2+} has a single paired d-electron, it preferentially occupies sites which are distorted from regular octahedra. This allows the single paired electron to occupy a lower energy level resulting from splitting of the $^5T_{2g}$ state by the lower site symmetry. The lower site symmetry also commonly causes the splitting of the higher energy ^5E_g states. The visible-near infrared absorption spectra of Fe^{2+} occupying a distorted octahedral site usually consist of a doublet centered near 10,000 cm^{-1}. The temperature dependence of Fe^{2+} on the distorted octahedral sites in olivine and orthopyroxene have been investigated (Burns, 1965; Fukao et al., 1968; and Sung et al., 1977) and was discussed in Chapter 3.

Fe^{2+} can also occupy sites with other than six coordinating ligands. The temperature dependence of the absorption spectrum of Fe^{2+} on the distorted cubic site in almandine garnet was reported by White and Moore (1972). The temperature dependence of the almandine spectra has here been extended to 400C. The absorption spectra

of Fe^{2+} on a distorted tetrahedral site in staurolite and occupying a site of unknown coordination in the channel of beryl were investigated over a range of temperatures from 20C to 300C. The compositions and sources of the Fe^{2+} minerals used are reported in Figure 12.

Table 12

Fe^{2+}-Minerals Chemical Compsotions and Sources

	Staurolite	Almandine	Fe-Beryl
SiO_2	27.48(26)	37.30(22)	66.82(18)
TiO_2	0.51(2)	0.08(5)	0.0
Al_2O_3	53.92(54)	20.95(11)	18.45(8)
Cr_2O_3	0.0	0.04(2)	0.0
MgO	2.23(3)	5.38(6)	0.0
CaO	0.0	1.39(4)	0.0
MnO	0.25(3)	1.08(30)	0.0
FeO	13.46(8)	32.89(15)	0.20(1)
Na_2O	0.0	0.02(2)	0.04(2)
K_2O	0.0	0.0	0.01(1)
Total:	97.86	99.66*	85.59**

* also 0.54(13) wt.% V_2O_5

**also 0.07(2) wt.% Cs_2O

| Staurolite	HVD #86370 Tessin, Switzerland α-γ section 0.0168(2) cm
Almandine	HVD # Fort Wrangell, Alaska random section 0.0186(2) cm
Fe-Beryl	HVD #102153 Minas Gerais, Brazil ω-ϵ section 0.2748(2) cm

1. Almandine Garnet

The absorption spectrum of Fe^{2+} on the distorted cubic site in almandine garnet has been measured by several workers (Clark, 1957; Burns, 1970; Moore and White, 1972; White and Moore, 1972; and Runciman and Sengupta, 1974). The spectrum consists of a very complex absorption envelope in the visible region comprised of approximately eight to fifteen weak, sharp bands and three relatively intense, broad bands in the near-infrared region. Moore and White (1972) attributed the weak bands in the visible region to spin-forbidden transitions of Fe^{2+} on the 8-coordinate site. Assignment of the bands to specific Fe^{2+} (VIII) transitions is difficult due to the large number of possible energy levels which result from the distortion of the site.

Assignment of the three intense, broad bands in the near-infrared to specific spin-allowed transitions of Fe^{2+} (VIII) has generated some controvery. Considering the actual D_2 distorted cubic site symmetry, the crystal field states are ^5A and $^5B_1$ arising from the cubic ground state ^5E_g and $^5A_1$ $^5B_2$ and $^5B_3$ arising from the $^5T_{2g}$ excited state. From symmetry considerations, the ^5A (ground state)$\rightarrow$ $^5B_1$, $^5B_2$, $^5B_3$ transitions are allowed, while the $^5A \rightarrow ^5A$ transition is not. White and Moore (1972) assigned the near-infrared region of the spectrum to transitions including the $^5A \rightarrow ^5A$ transition by invoking vibronic coupling to explain the band's non-zero intensity. Runciman and Sengupta (1974) calculated the energy levels of the spin-allowed Fe^{2+}

transitions using a point charge model which included the
influence of next-nearest neighbor silicon atoms. Their
assignment differs dramatically from that of White and Moore.
Both assignments can be summarized:
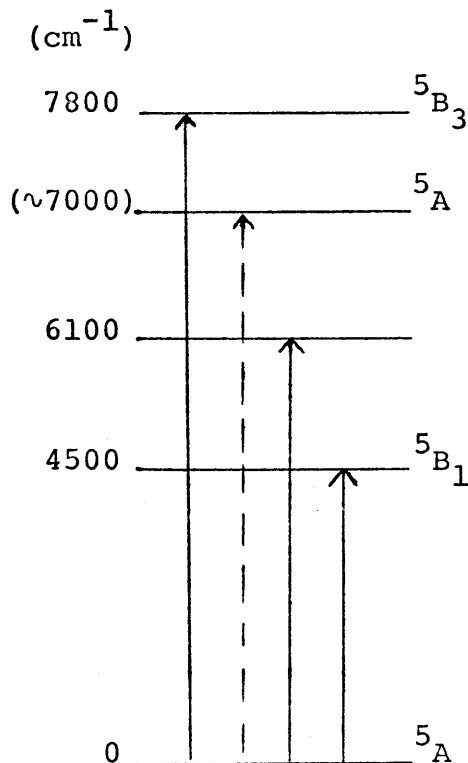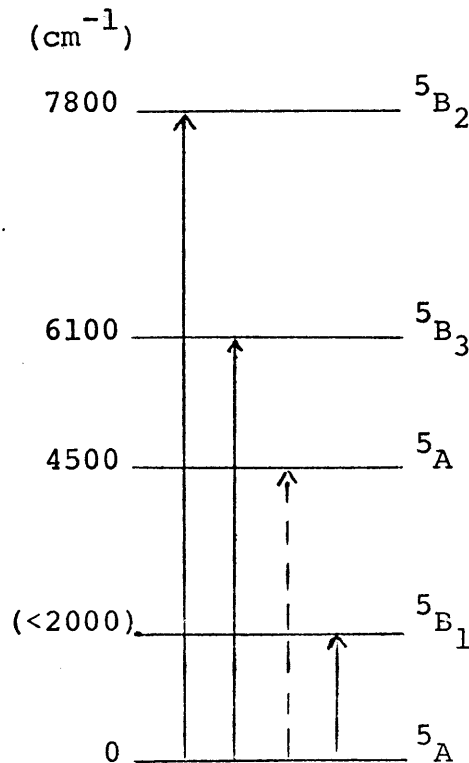
Runciman and Sengupta   White and Moore

Mössbauer spectroscopic data presented by Huggins (1975)
strongly supports the assignment of White and Moore. Huggins
determined that the splitting of the ^5E_g cubic ground state
by the D_2 symmetry is on the order of 1100 ± 50 cm^{-1}. The
absorption band arising from the $^5A \rightarrow {}^5B_1$ transition would
lie lower in energy than White and Moore were able to measure,
and not at 4500 cm^{-1} as suggested by Runciman and Snegupta.
White and Moore also measured
the absorption spectra of almandine over the temperature range

78K to 490K. They noted slight shifts in wavelength: the bands at 4400 cm^{-1} moved to lower energy while the bands at 5900 cm^{-1} and 7600 cm^{-1} shifted to higher energy. All three bands increased in intensity, with the symmetry-allowed 7600 cm^{-1} band exhibiting the greatest increase.

The crystal structure of the magnesium end-member garnet pyrope, has been determined at temperatures up to 750C by Meagher (1975). The {X} 8-coordinate site increased in mean M-O distance by approximately 0.5% over the temperature range 25C to 350C. The distortion of the site increased to a somewhat greater degree as the longer Mg(2)-O(4) distances increased at a greater rate than the Mg(1)-O(4) distances due to rotation of the edge-shared and corner-shared silica tetrahedra. The variance of cubic angles $(= \sum_{i=i}^{12} (\theta_i - 70.5)^2 / 11)$ increased from 3.81 to 4.21 ($\sim$10%) over the temperature range 25C to 350C.

Results

The absorption spectra in the region (350nm to 2500nm) of an almandine containing 32.9 wt % FeO were measured at five temperatures from 20C to 400C (Figure 24). Due to the complexity of the spectrum in the visible region, only the three spin-allowed bands were fit (Figure 25). The results of the fitting procedure are summarized in Table 13.

The temperature dependence of the almandine spectrum presented here is similar to that observed by White and Moore (1972). The spin-allowed bands broadened, shifted in energy
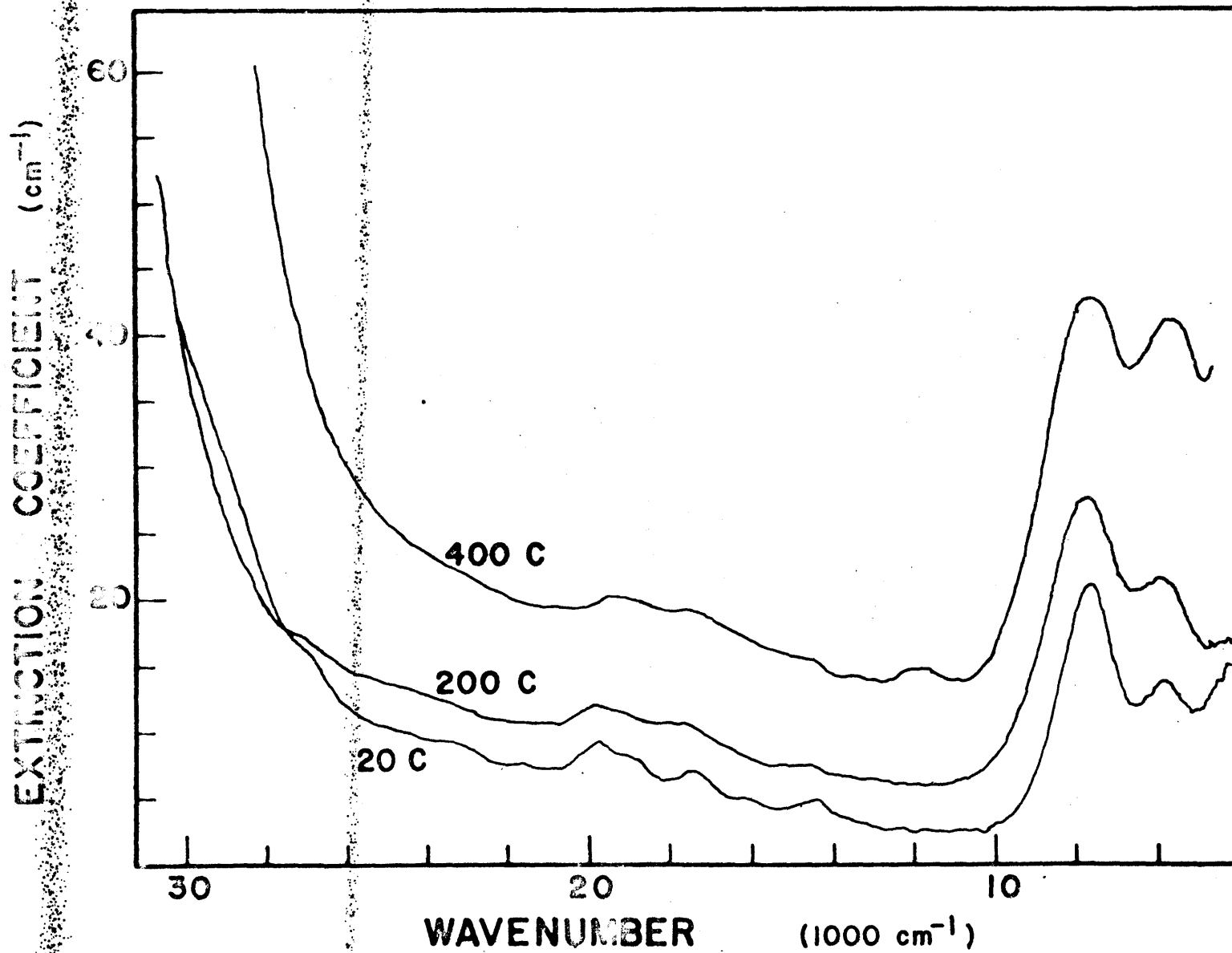
Figure 24. Absorption spectra of almandine garnet at 20C, 200C, and 400C
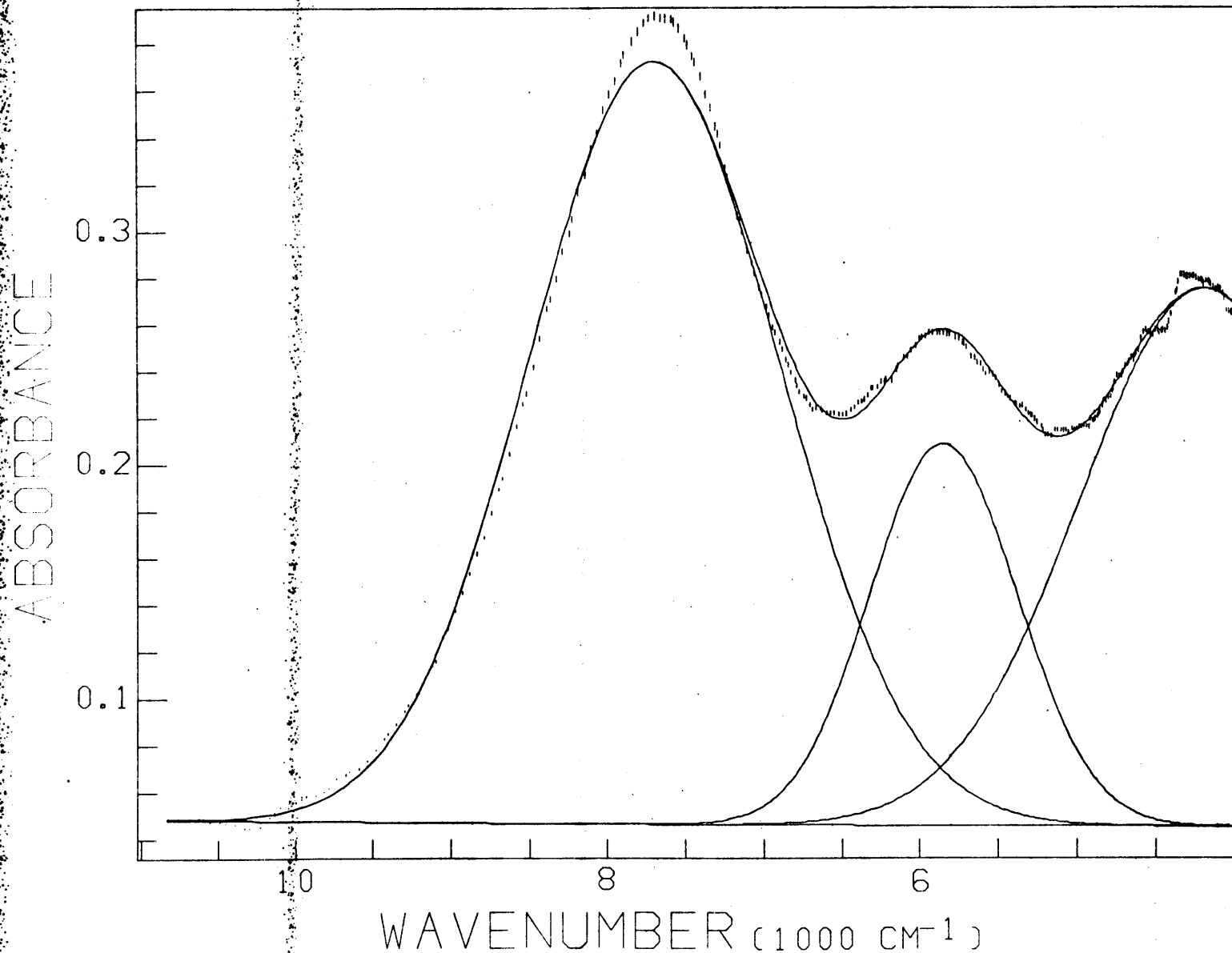
Figure 25.   20C spectrum of almandine garnet, computer fit

Table 13

Almandine Absorption Spectra Parameters

	20C	100C	200C	300C	400C
baseline (abs)	0.0414(1)	0.0759(1)	0.1224(2)	0.1643(5)	0.235(c)
a (abs)	0.0034(c)	0.00175(c)	0.000194(c)	0.000359(c)	0.000655(c)
b (cm^{-2})	0.006(c)	0.00623(c)	0.008957(c)	0.00883(c)	0.0091(c)
$^5A \rightarrow {}^5B_2$					
E (nm)	1300	1296	1286	1290	1312
E (1000 cm^{-1})	7.695(1)	7.719(1)	7.778(2)	7.754(3)	7.621(3)
W (1000 cm^{-1})	1.888(2)	2.047(3)	2.275(5)	2.454(8)	2.710(5)
I (cm^{-1})	17.5(2)	18.5(2)	20.7(2)	22.6(2)	30.2(3)
A (1000 cm^{-2})	35.3(4)	40.3(4)	50.1(6)	59.0(7)	87.3(10)
$^5A \rightarrow {}^5B_3$					
E (nm)	1710	1732	1712	1761	1756
E (1000 cm^{-1})	5.847(2)	5.774(3)	5.842(5)	5.676(7)	5.693(2)
W (1000 cm^{-1})	1.109(6)	1.224(7)	1.26(1)	1.46(2)	1.255(4)
I (cm^{-1})	8.8(1)	9.8(1)	9.8(3)	14.0(2)	17.5(2)
A (1000 cm^{-1})	10.3(2)	12.8(2)	13.2(6)	21.7(5)	23.4(3)
$^5A \rightarrow {}^5A$					
E (nm)	2396	2337	2416	2391	2410
E (1000 cm^{-1})	4.174(4)	4.279(3)	4.14(1)	4.182(6)	4.15(c)
W (1000 cm^{-1})	1.89(2)	1.54(2)	2.39(11)	1.35(3)	1.90(c)
I (cm^{-1})	12.4(1)	7.71(8)	10.3(1)	13.5(2)	25.8(c)
A (1000 cm^{-1})	24.9(4)	12.6(2)	26.2(13)	19.4(6)	52.2(c)
R^2	1860/270	3111/302	1729/303	593/275	1045/256

slightly and intensified dramatically. Unlike the spectra of

ruby and emerald, the symmetry-forbidden absorption band

of almandine (4200 cm^{-1}) did not increase in intensity at

a greater rate than the symmetry-allowed bands. The band

exhibiting the greatest increase in intensity was the high

energy 7700 cm^{-1} band. The ~145% increase in band intensity

was partially due to the increase in band width, but the

peak height also increased approximately 65%. The relative

peak heights of the three bands remained unchanged with

increased temperature. There are two possible explanations

for the difference between the effect of temperature on symmetry-

allowed and symmetry-forbidden transitions in the Cr^{3+}-minerals

and Fe^{2+} in almandine. A large degree of vibronic coupling

may be responsible for the intensity of all three

spin-allowed Fe^{2+} bands in almandine, in which case,

increasing the population of vibrational levels above the

ground state would equally increase the intensity of all

the bands. Alternatively, the increase in distortion of

the site, as evidenced by the increase in the variance of

site angles, could be the controlling factor in determining

the intensity, since site distortion changes appear to be

responsible for the decrease in absorption intensity with

temperature for Fe^{2+} on the M2 site in olivine. Until more

data are available on both crystal structures and absorption

spectra at elevated temperatures, it is impossible to

distinguish between the two explanations.

2. Staurolite

Fe^{2+} is located in a distorted tetrahedral site with an average M-O distance of 1.95Å in staurolite. Staurolite is monoclinic and the Fe^{2+}-site has point symmetry C_s (Náray-Szabó and Sasvári, 1958). The crystal field ground state of a d^6 ion occupying a regular tetrahedron is ^5E. The lower site symmetry of the site in staurolite causes splitting of both the ^5E ground state and the $^5T_2$ excited state.

Bancroft and Burns (1967) measured the polarized absorption spectra of staurolite. Each polarized spectrum contained an intense absorption in the region 4500-7100 cm^{-1}. The β- and α-polarized spectra consisted of very broad doublets while the γ-polarized spectra apparently contained a single broad band. Dickson and Smith (1976), in an attempt to identify spin-forbidden bands due to tetrahedral Fe^{2+} measured the spectra of staurolite at 77K. The intensity of the spin-allowed band was too great to allow them to measure the bands. The absorption edge due to the Fe^{2+} spin-allowed bands receded into the infrared as the temperature decreased.

Results

A staurolite crystal containing 13.46 wt.% FeO was cut parallel to the (010) face. In order to measure the zenith of the intense absorption bands near 5000 cm^{-1}, it was necessary to measure the unpolarized spectrum since the infrared polarizer used did not polarize light in the region 2150nm to 2500nm. The spectrum was measured at four temperatures to

300C (Figure 26). At 300C the peak maximum was more intense than could be measured by the Cary 17, so only the 20C, 100C, and 200C spectra were curve fit to a single band (Figure 27). The results are presented in Table 14.

The extreme intensity of the absorption in the region 1700 nm to 2500nm made the uncertainties in peak parameters great. The band shifted slightly to higher energy by 150 cm^{-1} between 20C and 200C. The bands did not broaden significantly. The peak intensity measured was at the limit of the capabilities of the Cary 17 and changes were difficult to measure. The band showed little change in integrated intensity to 200C, but was off scale at 300C.

The shift to higher energy of the peak maximum is counter to what is expected for an expanding site. This probably indicates that the site distortion changes with temperature. A more detailed study involving measurement of polarized spectra would be necessary to confirm this.
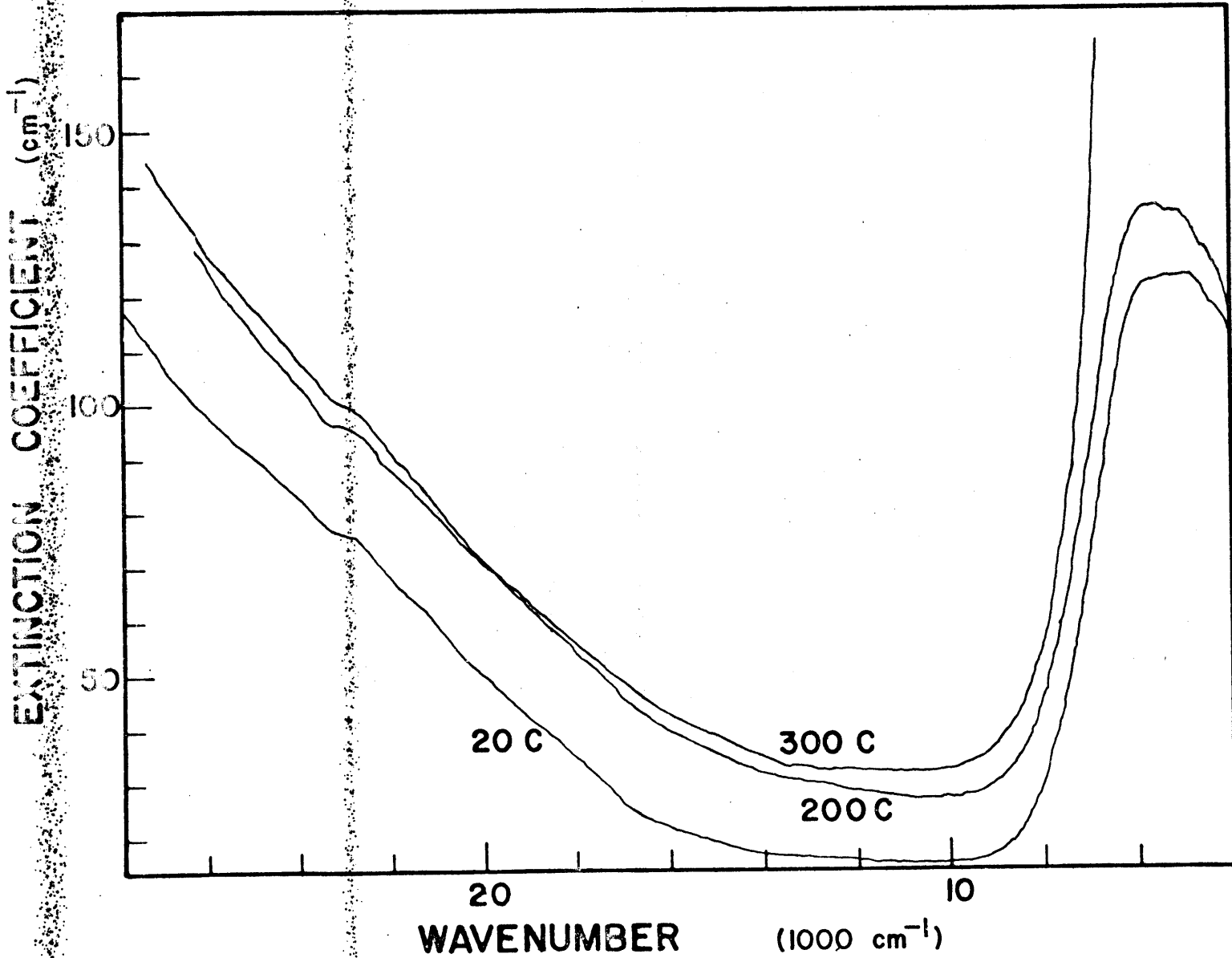
Figure 26. Unpolarized absorption spectra of staurolite at 20C, 200C, and 300C
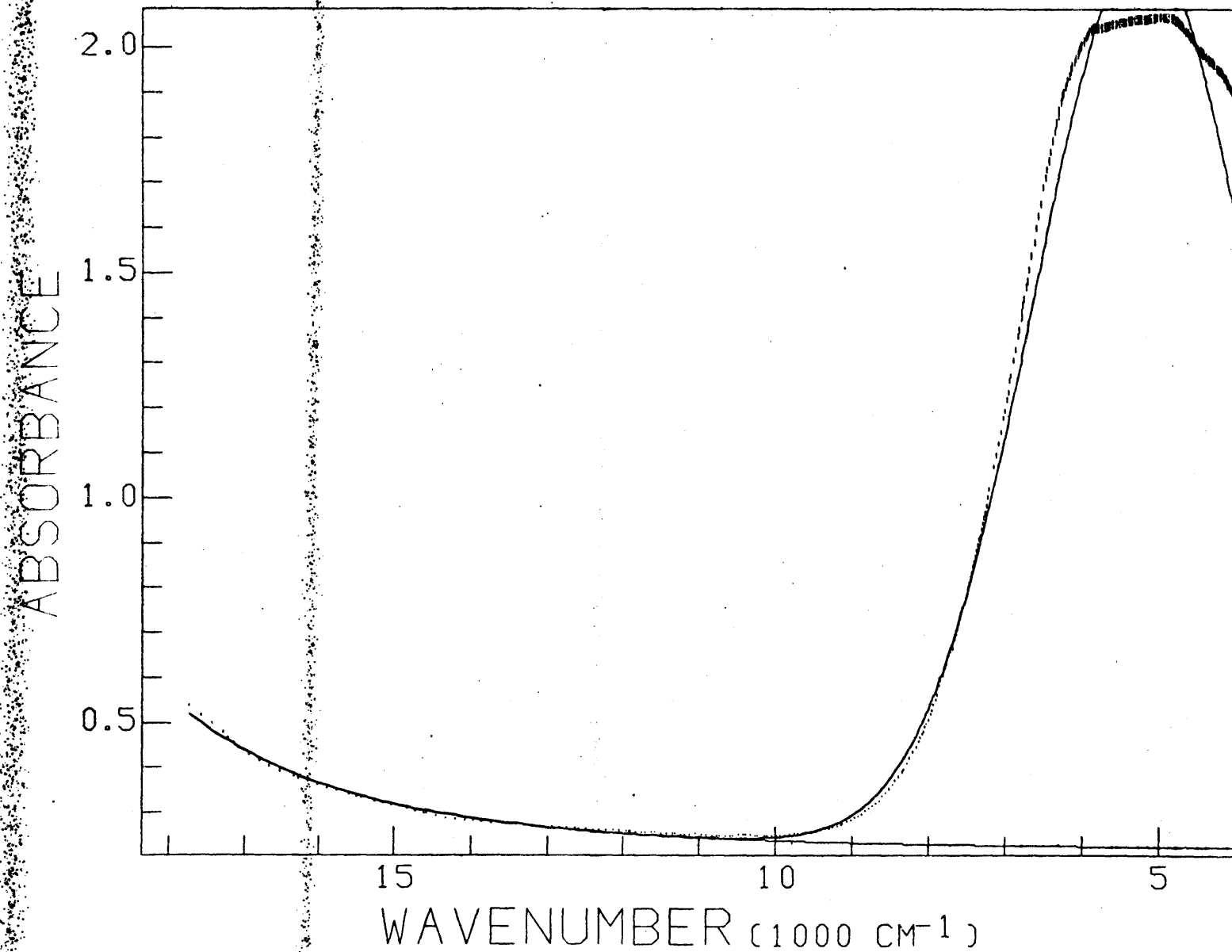
Figure 27.   20C spectrum of staurolite, computer fit

Table 14

Staurolite Absorption Spectral Parameters

	20C	100C	200C
baseline (abs)	0.2137(6)	0.2073(14)	0.3659(8)
a (abs)	0.0072(2)	0.0224(7)	0.0390(5)
b (cm^{-2})	0.01193(9)	0.00939(9)	0.00876(5)
$^5E \rightarrow {}^5T_2$			
E (nm)	1926	1899	1874
E $(1000\ cm^{-1})$	5.193(1)	5.265(1)	5.335(1)
W $(1000\ cm^{-1})$	3.392(2)	3.430(3)	3.397(2)
I (cm^{-1})	119.(1)	122.(1)	122.(1)
A $(1000\ cm^{-2})$	430.(5)	445.(5)	440.(5)
R^2	30880/330	22020/292	46500/363

3. Fe-Beryl

Iron has been shown to occupy two distinct types of sites in beryl (Wood and Nassau, 1968; Goldman et al., 1978). Fe^{2+} on the distorted octahedral Al^{3+} site gives rise to two bands at ~820nm and ~970nm in the E ∥ c absorption spectrum. The E⊥c absorption spectrum is dominated by a relatively intense band at ~820nm. This band and a weak band in the E ∥ c spectrum at ~2200nm have been assigned by Goldman et al. (1978) to Fe^{2+} on an undefined site in the channels of beryl based upon the intensity of the 820nm band and the large site size and distortion indicated by the positions of the bands.

The structure of beryl consists of six-membered rings of silica tetrahedra bridged by beryllium tetrahedra and aluminum octahedra so as to form channels which extend through the structure (Gibbs et al., 1968). Cations and water can occupy the channel either at the level of the silica rings or in the larger cavity at the level of the Al^{3+}, Be^{2+} sites. Duncan and Johnston (1974) proposed that Fe^{2+} occupies a five-coordinate site in the channels of structurally similar cordierite, based on single crystal Mössbauer spectroscopy. The Fe^{2+} is coordinated by four oxygen ions of the walls of the channel and a water molecule.

Results

The polarized absorption spectra of a pale green beryl containing 0.20 wt.% Fe were measured over the temperature range 20C to 300C. The E ∥ c spectrum indicated that there

was no octahedral site iron present in the sample (Figure 28).
The $E \perp c$ spectra (Figure 29) were fit to a single band at
12,450 cm^{-1} (Figure 30) after the sections of the spectra
containing water vibrational bands were removed. It was not
possible to measure the 4500cm^{-1} band ($E \parallel c$) because the
polarizers used do not polarize light in the region 2150 nm
to 2500 nm.

The 12,400 cm^{-1} band showed no change in energy to 300C.
The band broadened slightly and lost approximately 20% of
its integrated intensity. The reason for the loss in
absorption intensity is not clear. An overall expansion
of the site would result in a shift in peak position.
The loss in intensity may be due to changes in the population
of the vibrational energy levels or to the total breakdown
of the channel site.
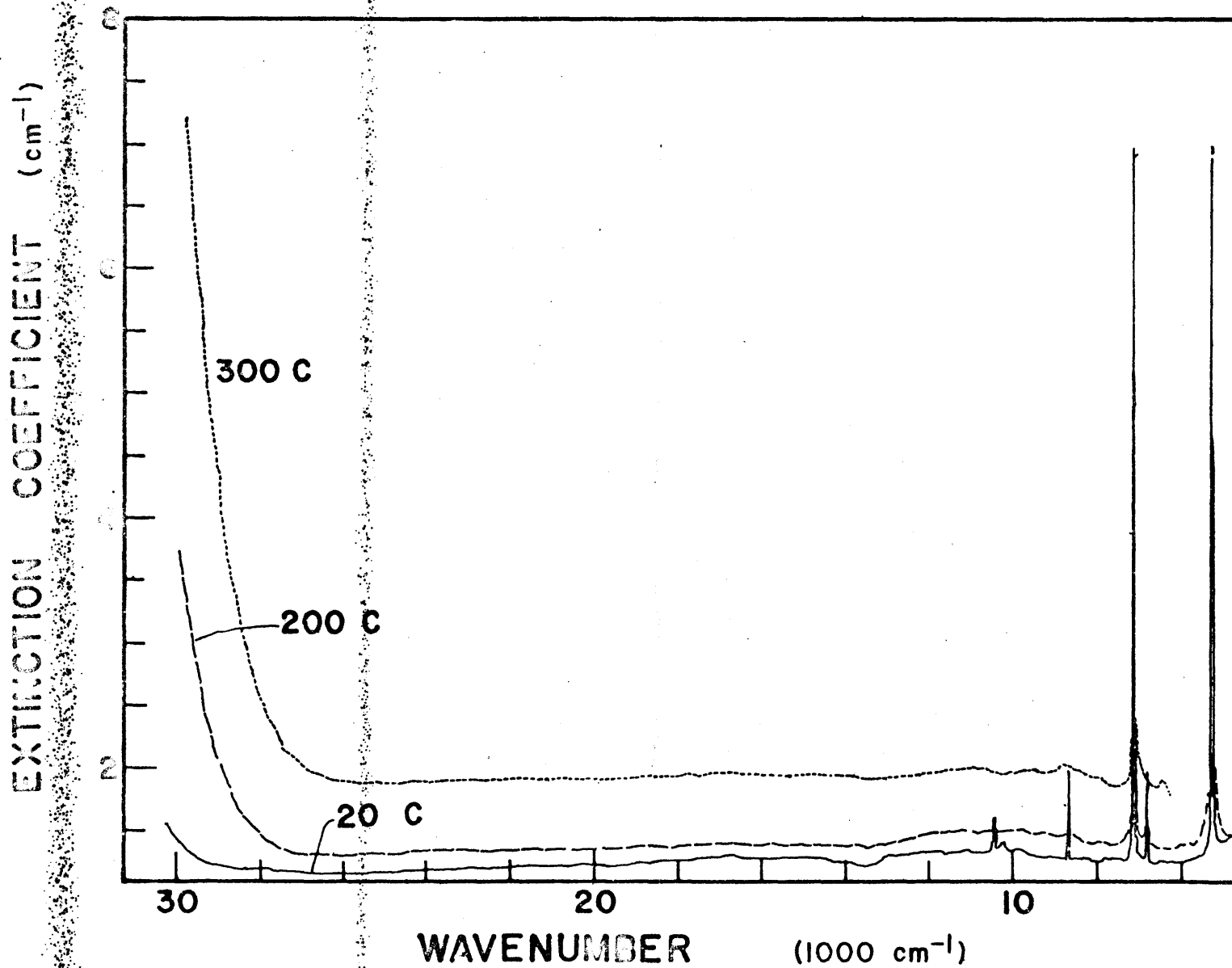
Figure 28. Absorption spectra of Fe^{2+}-beryl (E||c) at 20C, 200C, and 300C
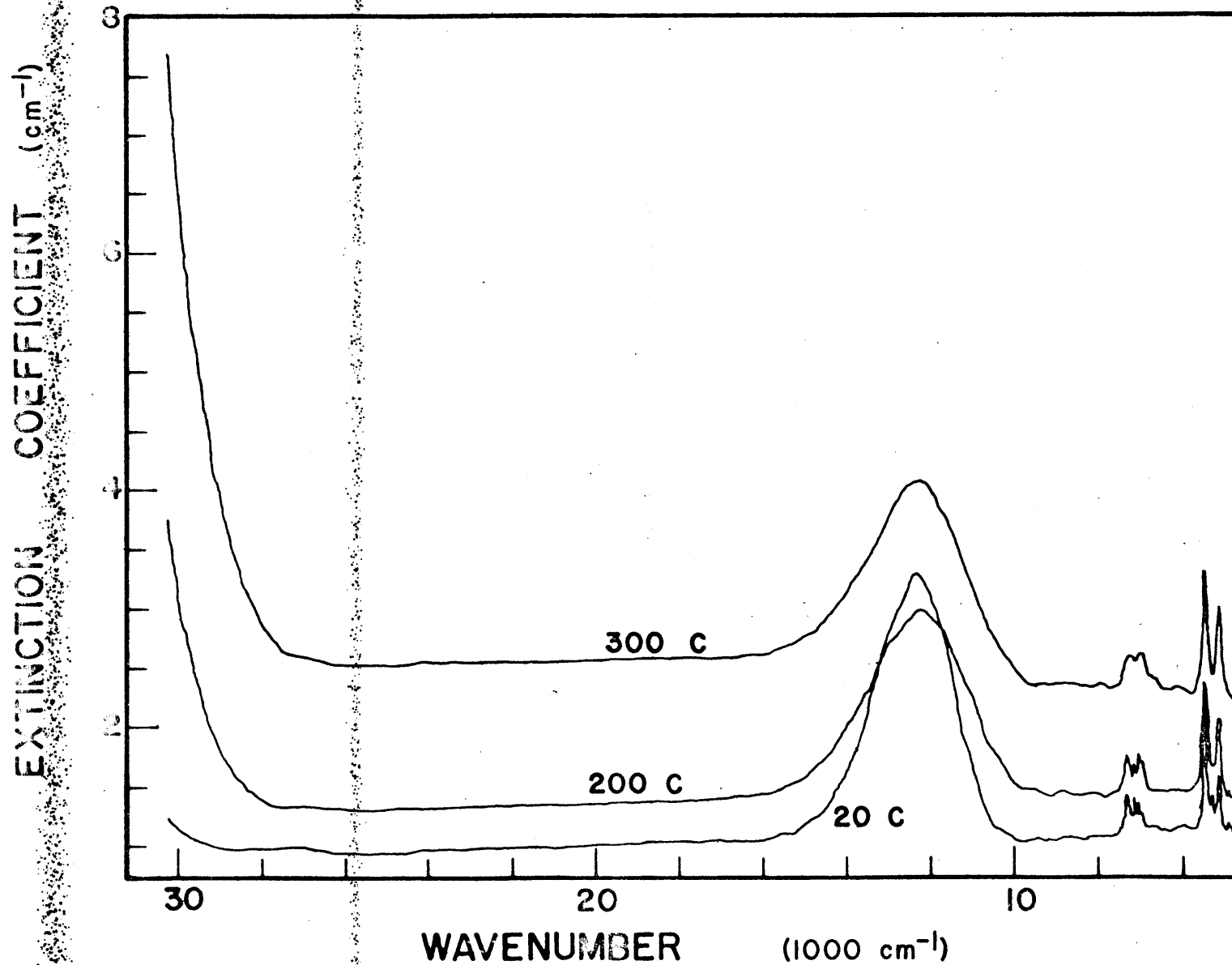
Figure 29.   Absorption spectra of Fe^{2+}-beryl (E||c) at 20C, 200C, and 300C
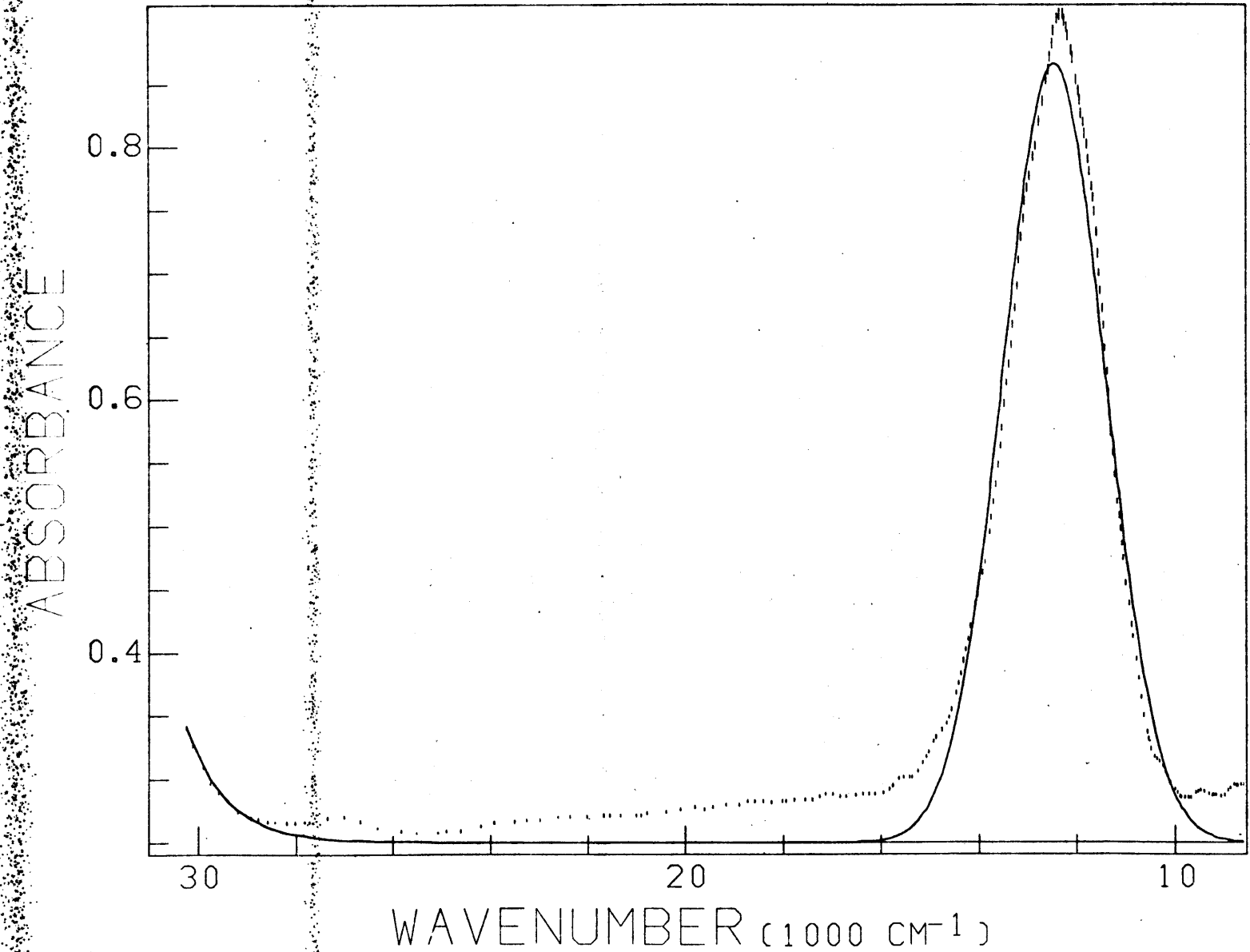
Figure 30. 20C spectrum of Fe^{2+}-beryl (E$\perp$c), computer fit

Table 15

Fe-beryl (E$\perp$C) Absorption Spectra Parameters

	20C	100C	200C	300C
baseline (abs)	0.25(c)	0.32(c)	0.3721	0.6754(4)
a (abs)	$7.17(7) \times 10^{-10}$	$1.11(6) \times 10^{-10}$	$2.6(2) \times 10^{-11}$	$8.1(4) \times 10^{-8}$
b (cm^{-2})	0.0204(c)	0.0234(c)	0.0237(1)	0.01826(6)
"$^5T_2 \rightarrow {}^5E$"				
E (nm)	803	802	810	802
E (1000 cm^{-1})	12.454(1)	12.469(1)	12.343(2)	12.469(3)
W (1000 cm^{-1})	2.453(2)	2.532(3)	2.830(6)	2.672(9)
I (cm^{-1})	2.244(3)	1.881(3)	1.581(3)	1.601(5)
A (1000 cm^{-2})	5.859(7)	5.069(7)	4.76(1)	4.55(2)
R^2	48190/196	18500/186	5767/159	8915/174

CHAPTER 7

d^5-Minerals Fe^{3+} and Mn^{2+}

Fe^{3+} commonly substitutes for Al^{3+} in minerals, while Mn^{2+} is mainly found in solid solution with iron and magnesium. Each of the five d electrons of the d^5 configuration is unpaired in a d-orbital resulting in a free ion ground state ^6S. In the presence of an octahedral crystal field, the ground state remains unsplit, $^6A_{1g}$. The higher energy quartet terms of the free ion are split by the octahedral field. Spin-forbidden transitions to the quartet states from the ground state are commonly measured in the visible-near-infrared spectra of Fe^{3+} and Mn^{2+} minerals.

The relative slopes of the energy levels on the Tanabe-Sugano diagram for d^5 (Figure 31) give an indication of the direction and magnitude of changes in energy of absorption bands due to Fe^{3+} and Mn^{2+}. The $^6A_{1g} \rightarrow {}^4T_{1g}(G)$ and $^6A_{1g} \rightarrow {}^4T_{2g}(G)$ transitions result in broad, low intensity bands which will shift to higher energy with increased temperature. The energy separation of the $^6A_{1g}$ and the $^4E(G)$ and $^4A_{1g}$ states is nearly independent of the strength of the crystal field. Absorption bands arising from $^6A_{1g} \rightarrow {}^4E(G)$ and $^6A_{1g} \rightarrow {}^4A_{1g}(G)$ transitions are sharp bands.

The absorption spectra of Fe^{3+}-minerals andradite and epidote and Mn^{2+}-minerals spessartite and rhodonite were measured over the temperature range 20C to 400C. Sources and compositions are reported in Table 16.
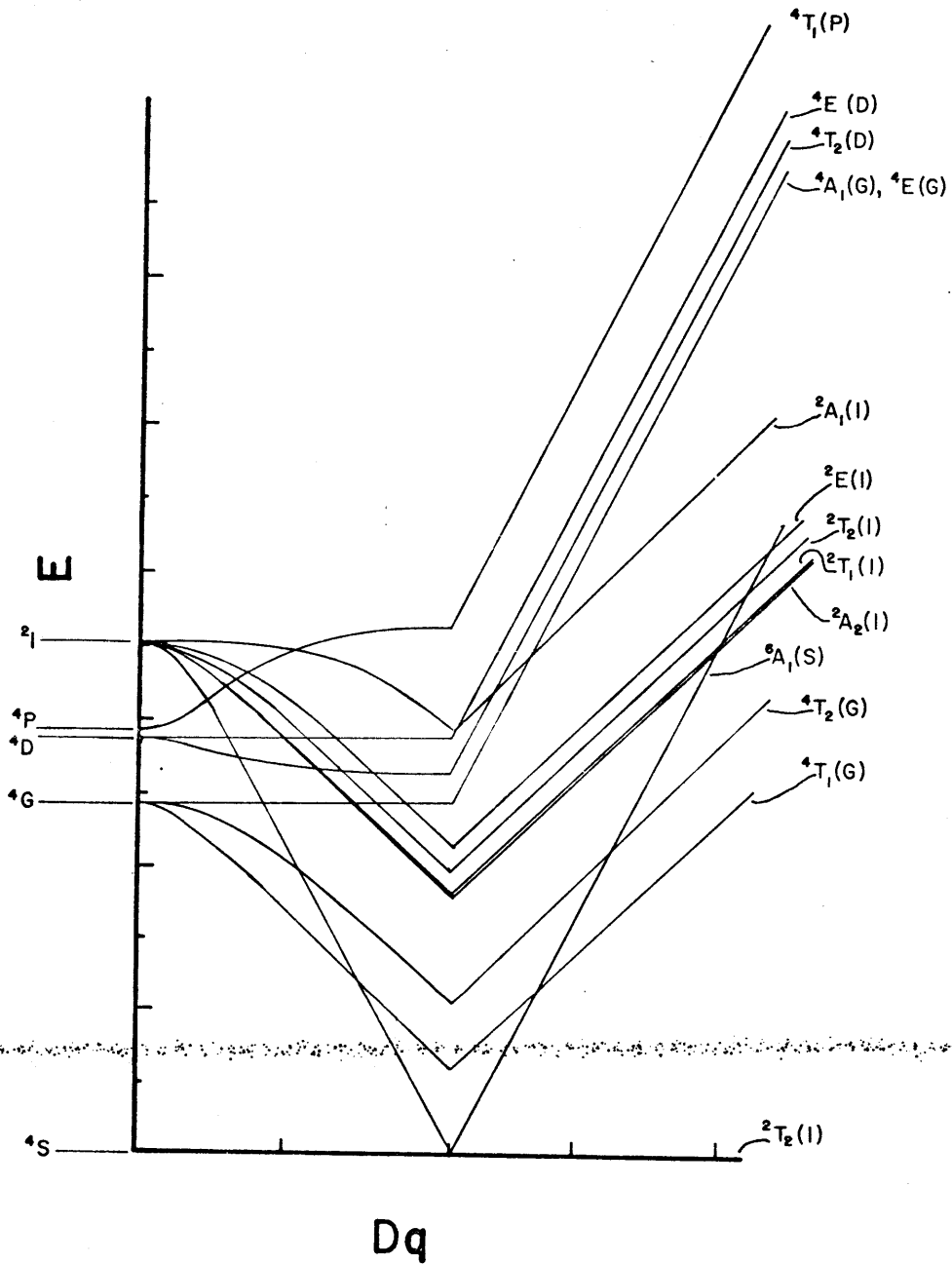
Figure 31. d^5 octahedral energy level diagram (after Keester and White, 1968).

Table 16

Fe^{3+} - and Mn^{2+}-Minerals Chemical Compositions and Sources

	Epidote	Andradite	Spessartite	Rhodonite
SiO_2	37.62(16)	35.48(28)	36.83(13)	47.25(23)
TiO_2	0.44(1)	0.05(2)	0.01(1)	0.02(2)
Al_2O_3	20.87(16)	0.06(1)	20.07(14)	0.04(1)
Cr_2O_3	-	0.00(1)	0.06(3)	0.02(1)
MgO	0.05(1)	0.21(2)	0.12(4)	0.46(1)
CaO	23.18(11)	33.13(23)	0.49(6)	4.83(3)
MnO	0.15(2)	0.01(2)	26.91(154)	36.25(25)
*FeO	14.25(17)	27.55(18)	14.92(139)	11.82(13)
Na_2O	-	0.00(2)	0.0	0.0
K_2O	-	0.00(1)	0.0	0.0
Total:	96.56	96.49	99.41	100.68

Epidote   UCB # 13528
             α-β section 0.0248(2) cm
             γ section 0.0120(2) cm

Andradite   HVD # 87373 Val Maleneo
             random section 0.0536(2) cm, 0.115(5) cm

Spessartite HVD # 107003, Rostadhein pegmatite, Jueland, Norway
             random section 0.0340(2) cm

Rhodonite   HVD # 92634, Broken Hill Mine, New South Wales
             α-β section 0.0640(2) cm

* All Fe reported as FeO

1. Andradite

Fe^{3+} occupies the slightly distorted octahedral (Y) site in silicate garnets (M-O distance 2.02Å, Novak and Gibbs, 1971). The optical absorption spectrum of Fe^{3+} in garnet has been reported by Manning (1967a, 1972) and Moore and White (1972). Three absorption bands were measured; two broad weak bands at 16,500 cm^{-1} and 12,500 cm^{-1} which were assigned to $^6A_1 \rightarrow {}^4T_2$(G) and $^6A_1 \rightarrow {}^4T_1$(G), respectively, and a sharp, asymmetry peak at 21,400 cm^{-1} assigned to $^6A_1 \rightarrow {}^4E, {}^4A_1$(G).

The structure of the aluminum end member garnet, grossularite $(Ca_3Al_2Si_3O_{12})$, has been determined to 675C by Meagher (1975). The Al(Y) site is only slightly distorted, and both the shared and unshared edges of the (Y) octahedron expand at nearly the same rate with increased temperature. The octahedral bond-angle variance (Robinson et al., 1971) decreases with increased temperature, indicating that the site becomes more regular.

Results

An apple green andradite containing 30.6 wt.% Fe_2O_3 was used to measure the absorption spectra of Fe^{3+} in garnet at five temperatures from 20C to 400C (Figure 32). The crystal was cut and thinned to 0.115 cm. The absorption spectra in the region 450nm to 1350nm was measured in order to obtain reasonable intensity of the peaks at 17,000 cm^{-1} ($^6A_1 \rightarrow {}^4T_2$) and 11,700 cm^{-1} ($^6A_1 \rightarrow {}^4T_1$) (Figures 33 and 34). The same sample was further thinned in order to measure the sharp bands at 22,900 cm^{-1} and 22,700 cm^{-1} ($^6A_1 \rightarrow {}^4E, A_1$) (Figures 35 and 36). Fit spectral parameters are reported in Table 17.
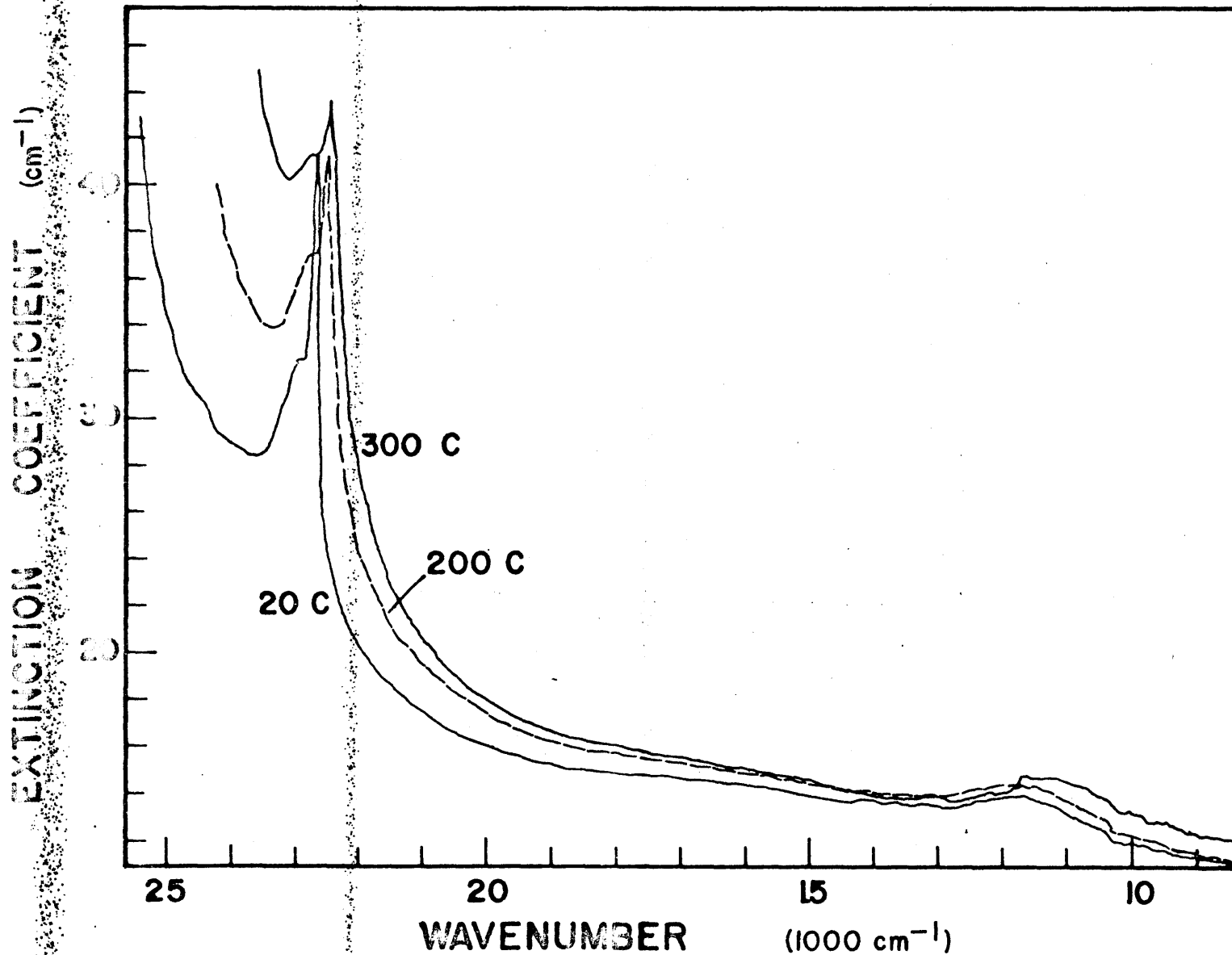
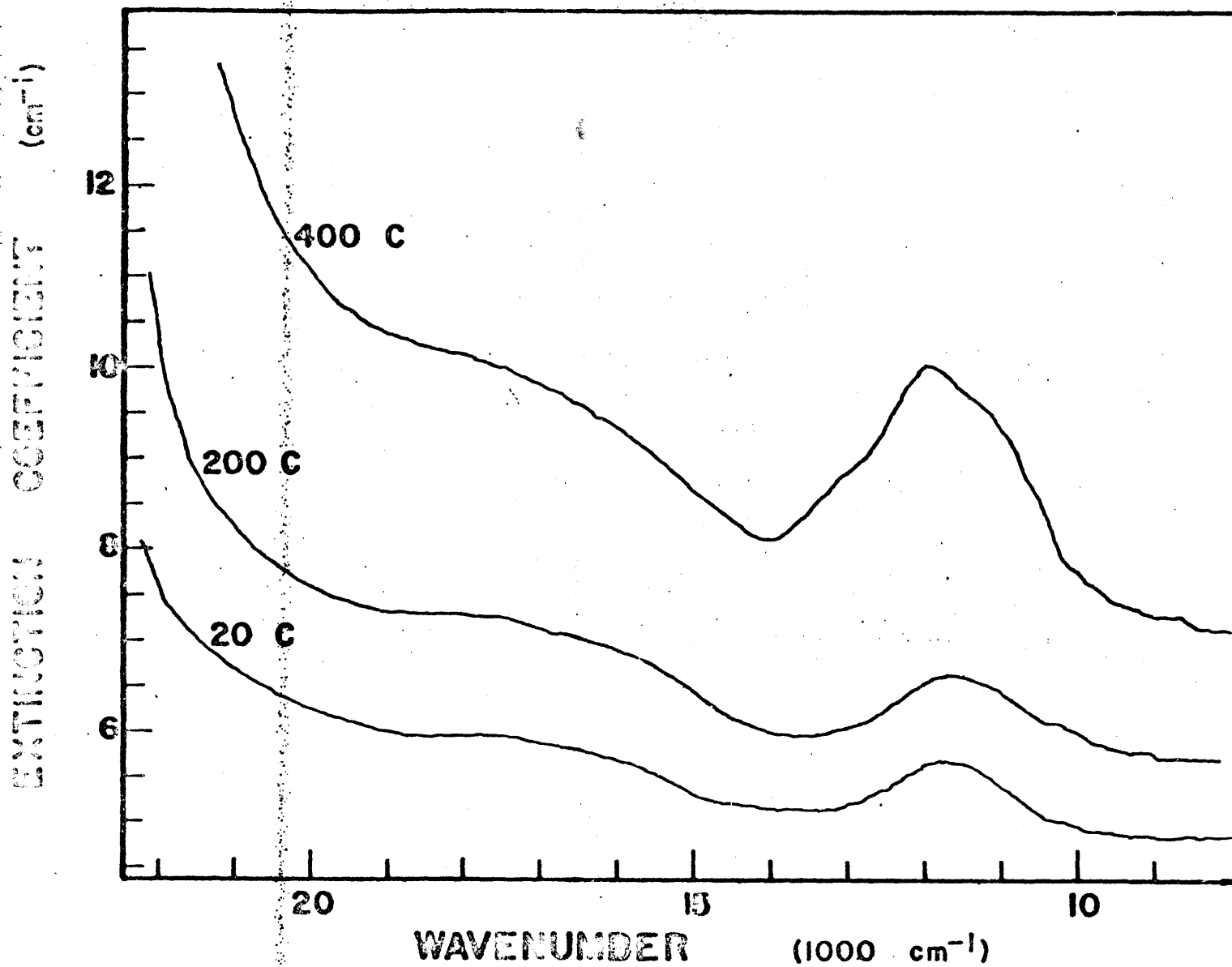Figure 32. Absorption spectra of andradite (380-1350nm) at 20C, 200C, and 300C

Figure 33. Absorption spectra of andradite (450-1350nm) at 20C, 200C, and 400C
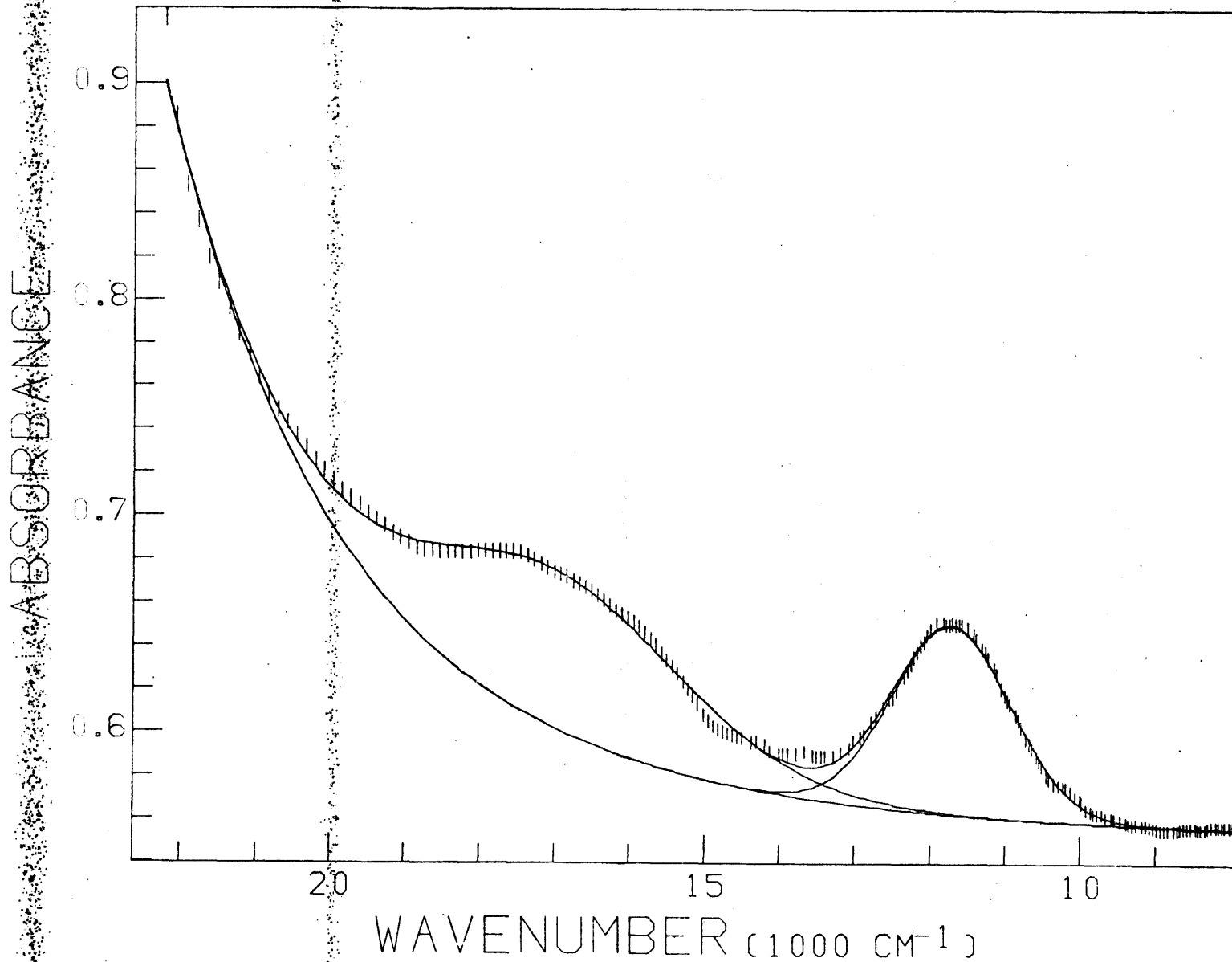
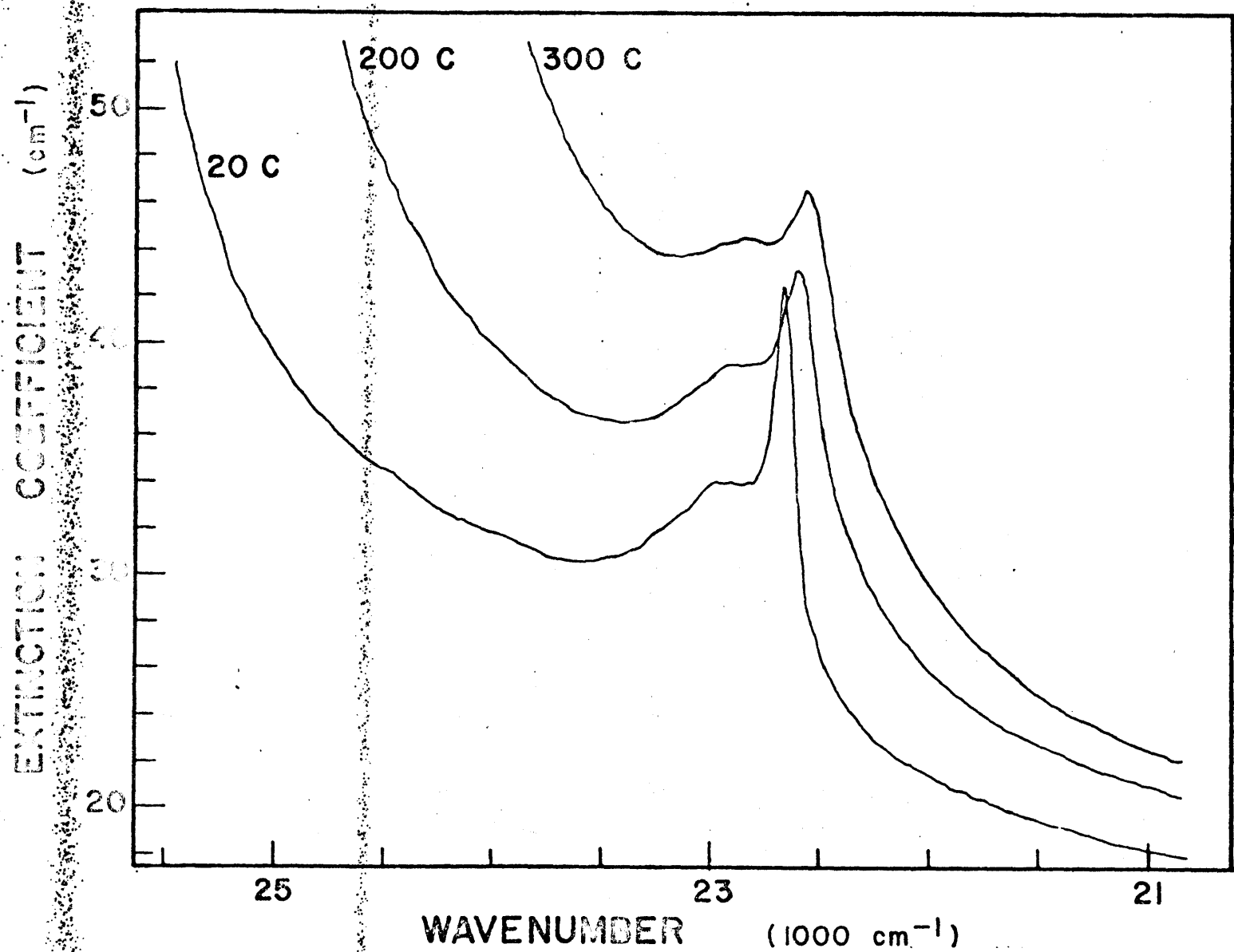Figure 34. 20C spectrum of andradite (450-1350nm), computer fit

Figure 35. Absorption spectra of andradite (380-480nm) at 20C, 200C, and 300C
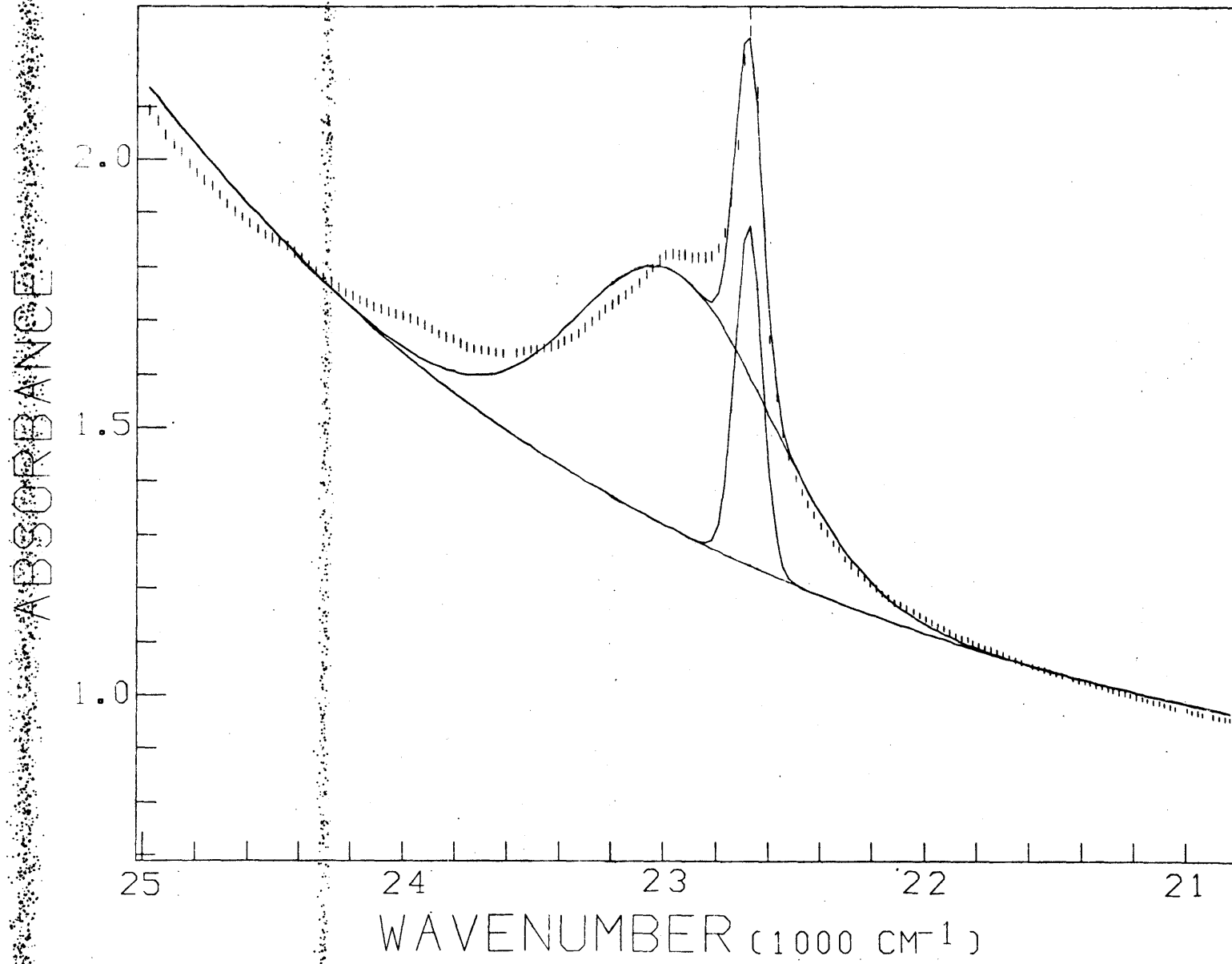
Figure 36.   20C spectrum of andradite (380-480nm), computer fit

Table 17

Andradite Absorption Spectra Parameters (380-480nm)

	20C	100C	200C	300C
baseline (abs)	0.6982(c)	0.6989(c)	0.6996(c)	0.7001(c)
a (abs)	0.00584(6)	0.00701(8)	0.00794(9)	0.00365(4)
b (cm^{-2})	0.00882(2)	0.00877(2)	0.00903(2)	0.01117(2)
$^6A_1 \rightarrow {}^4E$				
E (nm)	435	437	439	441
E (1000 cm^{-1})	22.964(2)	22.906(2)	22.799(3)	22.689
W (1000 cm^{-1})	0.882(5)	0.916(5)	0.890(6)	0.796(8)
I (cm^{-1})	8.98(6)	9.14(6)	9.29(7)	9.1(1)
A (1000 cm^{-2})	8.43(6)	8.91(6)	8.80(7)	7.72(8)
$^6A_1 \rightarrow {}^4A_2$				
E (nm)	441	442	442	444
E (1000 cm^{-1})	22.674(1)	22.646(1)	22.602(1)	22.545(2)
W (1000 cm^{-1})	0.121(1)	0.148	0.169(3)	0.176(6)
I (cm^{-1})	11.9(1)	9.6(1)	6.9(1)	5.0(1)
A (1000 cm^{-2})	1.53(2)	1.51(2)	1.24(3)	0.94(4)
R^2	2131/158	960/136	143/120	72/112

Andradite (450-1260nm) Absorption Spectral Parameters

	20C	100C	200C	300C	400C
baseline (abs)	0.5491(10)	0.5690(6)	0.6535(7)	0.7765(7)	0.81(c)
a (abs)	0.0036(5)	0.00088(15)	0.00019(3)	0.00054(19)	0.000841(c)
b (cm^{-2})	0.0093(3)	0.0126(3)	0.0163(3)	0.0149(7)	0.0149(c)
$^6A_1 \rightarrow {}^4T_2$					
E (nm)	587	578	568	579	577
E (1000 cm^{-1})	17.04(4)	17.31(4)	17.60(4)	17.27(8)	17.31(1)
W (1000 cm^{-1})	4.03(11)	4.66(10)	4.93(8)	6.81(16)	5.18(3)
I (cm^{-1})	0.64(3)	0.95(5)	1.35(6)	2.62(13)	2.29(10)
A (1000 cm^{-2})	2.74(13)	4.7(3)	7.1(4)	19.0(12)	12.6(5)
$^6A_1 \rightarrow {}^4T_1$					
E (nm)	854	860	868	849	851
E (1000 cm^{-1})	11.713(8)	11.631(10)	11.515(11)	11.769(6)	11.748(5)
W (1000 cm^{-1})	1.35(2)	2.07(3)	2.12(3)	1.92(2)	2.50(1)
I (cm^{-1})	0.76(3)	0.60(4)	0.36(4)	1.84(8)	2.72(11)
A (1000 cm^{-2})	1.50(7)	1.77(8)	1.95(9)	3.77(17)	7.3(3)
R^2	176/185	222/161	580/164	170/182	498/215

The broad, weak spin-forbidden bands at 17,000 cm^{-1} and 11,700 cm^{-1} shifted to higher energy with increased temperature and broadened significantly. The bands also increased in intensity. The crystal field independent transitions, $^4A_1 \rightarrow E$ and $^4A_1 \rightarrow {}^4A_1$, consisted of a sharp, narrow band at 22,670 cm^{-1} superimposed on a slightly broader band at 22,900 cm^{-1}. Because of inconsistencies of the baseline, the broader band was not fit very well at 20C and 100C. The peak position may be high by as much as 100 cm^{-1}. The bands both shifted to lower energy by ∿150 cm^{-1}, which indicates that the bands are not absolutely field independent. The better characterized band at 22,670 cm^{-1} shifted 130 cm^{-1} as the temperature increased from 20C to 300C. This shift is significantly less than the measured energy shifts of crystal field dependent bands of both Fe^{2+} and Cr^{3+}.

The $^6A_1 \rightarrow {}^4E$ and $^6A_1 \rightarrow {}^4A_1$ band intensities decreased sharply with increased temperature. This decrease, which was also observed in the field independent spin-forbidden bands of Cr^{3+} in emerald, could indicate that specific vibrational levels must be occupied in order for the field-independent spin-forbidden transitions to occur. Increased temperature increased the occupation of higher energy vibrational levels and decreased the probability of the spin-forbidden transition. The field-dependent transitions which occur over a broader energy region can accomodate changes in the occupancy of the vibrational levels and therefore do not show the dramatic decrease in absorption intensity.

2. Epidote

Fe^{3+} occupies the very distorted octahedral M(3) site
in epidote (mean M-O distance 2.00-2.04Å, Gabe et al., 1973)
with site symmetry C_s. The absorption spectra of Fe^{3+}
in epidote, reported by Burns and Strens (1967), showed
significant polarization dependence. Two sharp bands at
22,200 cm^{-1} were found to be present in all three polarizations
and were attributed to the $^6A_1 \rightarrow {}^4E, {}^4A_1$ transition of Fe^{3+}.
The other two Fe^{3+} bands due to $^4A_1 \rightarrow {}^4T_2$ and $^4A_1 \rightarrow {}^4T_1$
occured as weak, broad bands at 12,300 cm^{-1} and 17,900 cm^{-1}
in α-polarized spectrum, at 11,000 cm^{-1} and 17,900 cm^{-1} in
the β-polarized spectra, and with considerably more intensity
at 9,600 cm^{-1} and 16,500 cm^{-1} in the γ-polarized spectra. With
increased Fe^{3+} content, that is, with increased M(3) site
size (Gabe et al., 1973), Burns and Strens (1967) noted that
the absorption band maxima migrated. The γ-polarized bands
at 10,000 cm^{-1} and 17,000 cm^{-1}, as well as the 22,000 cm^{-1}
peaks in all polarizations, shifted to lower energy. The
α-polarized band at 11,000 cm^{-1} shifted to higher energy.

Results

The α- and β-polarized absorption spectra of an epidote
containing 15.8 wt.% Fe_2O_3 were measured at four temperatures
from 20C to 300C. Since the extremely thin sample, which was
necessary in order to record γ-polarized bands at 22,000 cm^{-1},
fell from the beam path during the recording of the 300C spectrum,
only the γ-polarized spectra at 20C, 100C, and 200C are reported.

Each spectrum was fit to four peaks. The fit 20C α-,
β-, and γ-polarized spectra are presented in Figures 37, 38
and 39, respectively, and the spectral parameters are reported
in Tables 18, 19 and 20. It was not possible to measure the
absorption spectra (α and β) in the region 750nm to $\sim$900nm,
because of the previously described problem with the slit
system of the Cary 17. The lack of data in this region
seriously affected the fitting procedure. The low energy
band was fit to a region with data points and could be as
much as 900-1000 cm^{-1} too low in energy and 500-1500 cm^{-1}
too narrow.

The field independent bands at 21,000 cm^{-1} shifted to lower ener
by 200-300cm^{-1} and broadened 20-50%. They also decreased
in integrated intensity by 10-40%. The temperature dependence
of the lower energy bands was more complicated. The $^6A_1 \rightarrow {}^4T_2$
and $^6A_1 \rightarrow {}^4T_1$ bands at 17,600 cm^{-1} and 12,100 cm^{-1},
respectively, in the α-polarized spectra are weak and broad
(Figure 40). From 20C to 200C, the bands decreased in energy
450cm^{-1} and 730 cm^{-1}. This shift is opposite to that
observed by Burns and Strens (1967) due to increased Fe^{3+}
concentration and site size. The bands showed little change
in width and decreased in intensity $\sim$20%. The bands in the
β-polarized spectra are so weak that it is impossible to
visually identify the peak maxima (Figure 41). This factor
seriously affects the fitting procedure in that convergence
to a unique set of peak parameters may not possible. Also,
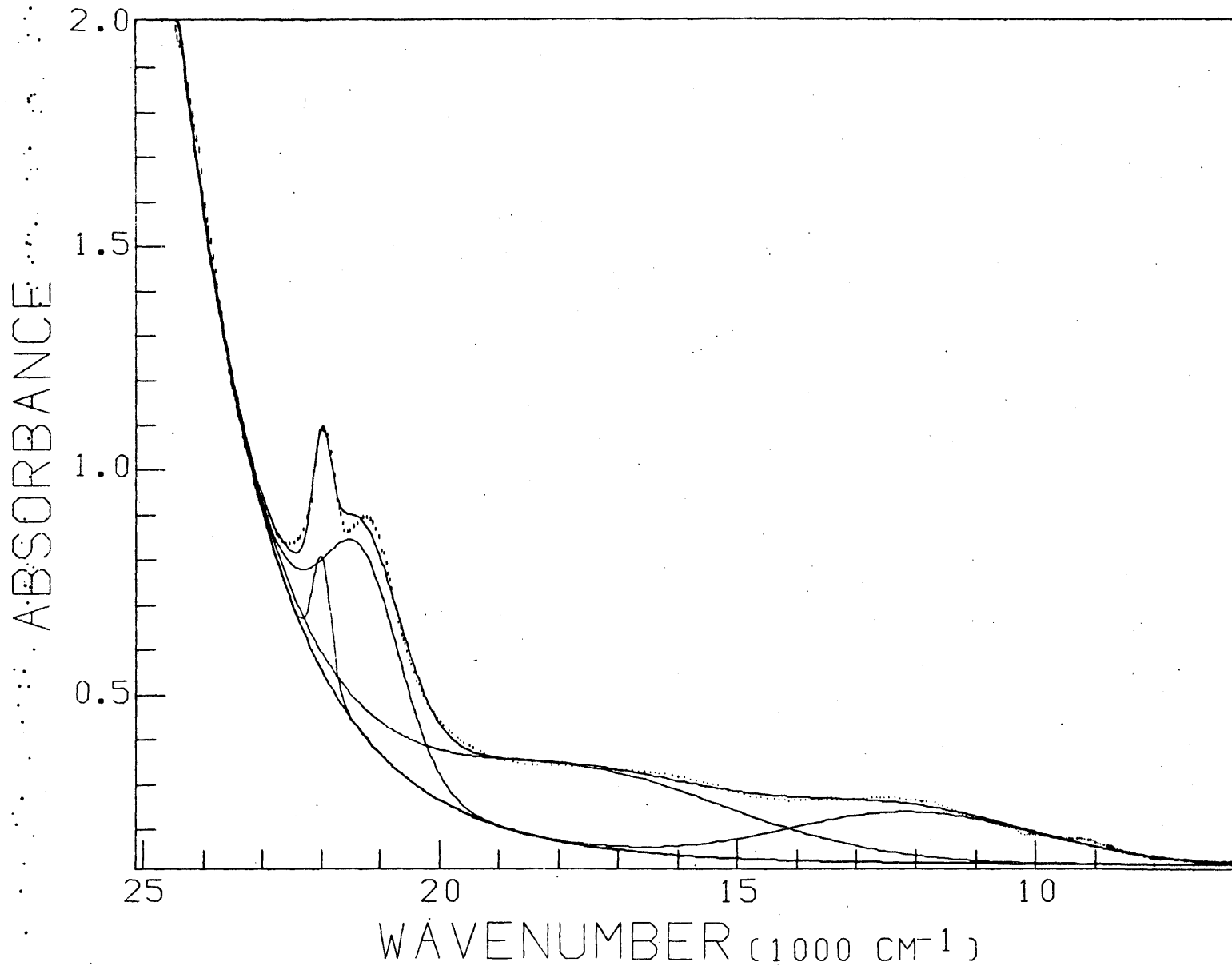the choice of a baseline is critical in the determination
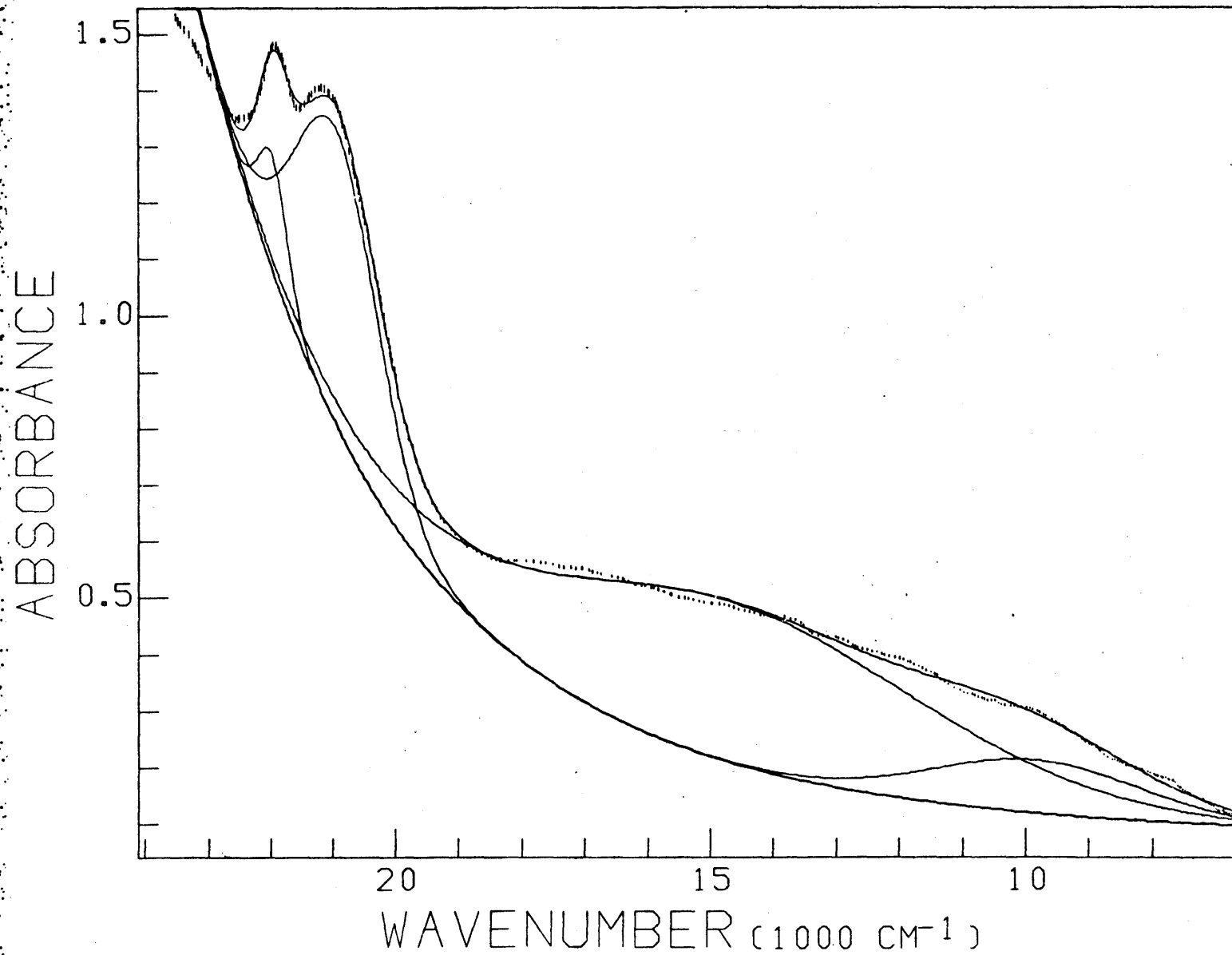
Figure 37. 20C spectrum of epidote (α), computer fit

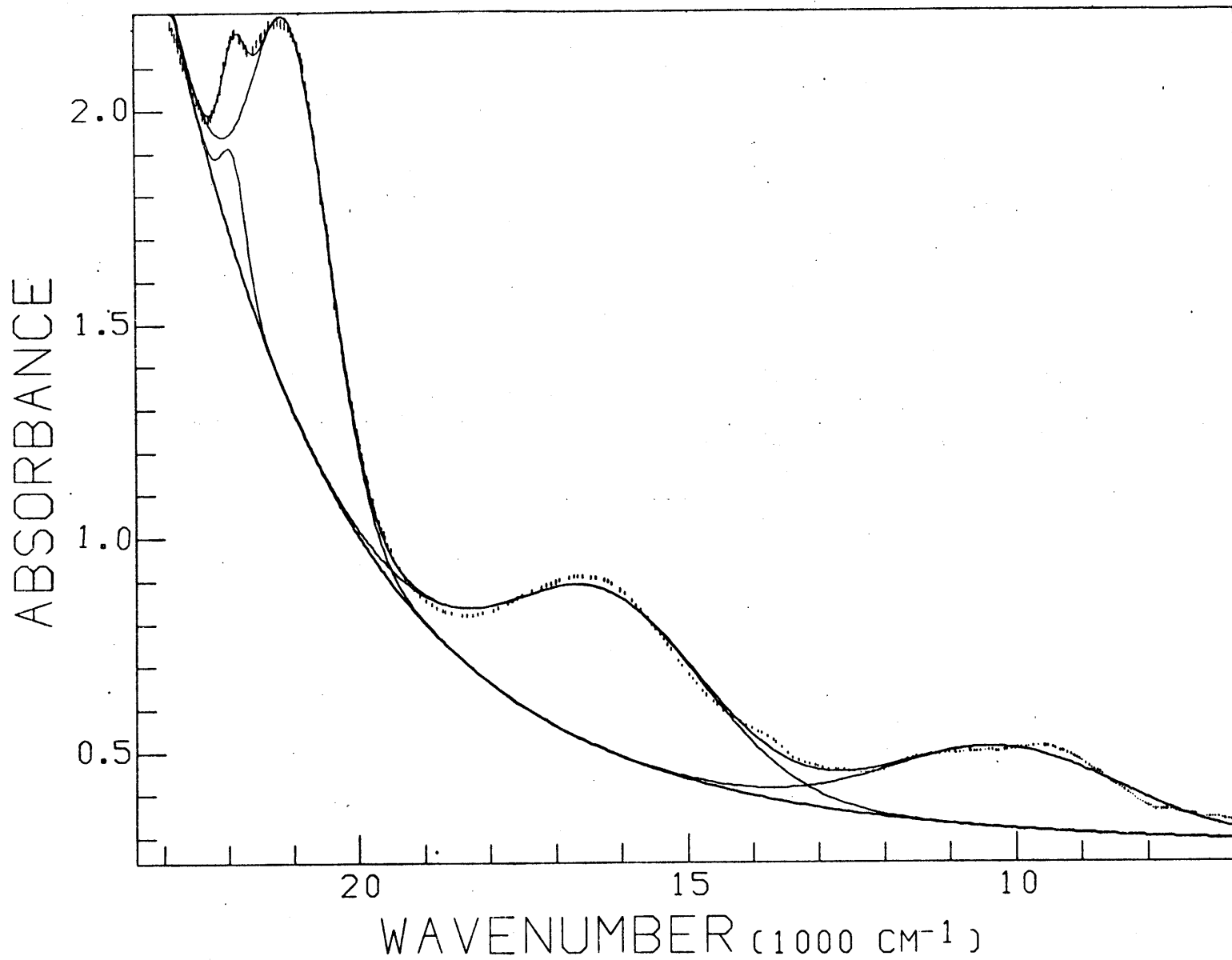Figure 38. 20C spectrum of epidote (β), computer fit

Figure 39.   20C spectrum of epidote (γ), computer fit

Table 18

Epidote (α) Absorption Spectra Parameters

	20C	100C	200C	300C
baseline (abs)	0.1212(3)	0.0918(5)	0.1855(5)	0.26(c)
a (abs)	0.00076(2)	0.00216(6)	0.00234(8)	0.00170(13)
b (cm^{-2})	0.01311(5)	0.01140(5)	0.01137(6)	0.00120(13)
$^6A_1 \rightarrow {}^4A_1$				
E (nm)	455	456	457	458
E $(1000\ cm^{-1})$	21.987(2)	21.923(2)	21.879(4)	21.812(6)
W $(1000\ cm^{-1})$	0.359(5)	0.439(8)	0.515(15)	0.53(3)
I (cm^{-1})	10.20(15)	8.23(15)	6.38(19)	3.87(18)
A $(1000\ cm^{-2})$	3.90(8)	3.85(12)	3.49(17)	2.20(17)
$^6A_1 \rightarrow {}^4E$				
E (nm)	469	472	474	475
E $(1000\ cm^{-1})$	21.317(4)	21.173(6)	21.100(9)	21.037(11)
W $(1000\ cm^{-1})$	1.570(9)	1.562(11)	1.651(16)	1.81(2)
I (cm^{-1})	16.62(16)	14.98(15)	14.59(16)	12.97(16)
A $(1000\ cm^{-2})$	27.7(3)	24.9(4)	25.6(5)	25.0(5)
$^6A_1 \rightarrow {}^4T_2$				
E (nm)	569	580	584	563
E $(1000\ cm^{-1})$	17.58(2)	17.25(3)	17.13(2)	17.76(14)
W $(1000\ cm^{-1})$	6.03(9)	6.12(10)	6.03(10)	9.9(3)
I (cm^{-1})	7.09(6)	6.89(7)	5.46(6)	4.44(11)
A $(1000\ cm^{-2})$	45.5(9)	44.9(10)	35.0(8)	47.(2)
$^6A_1 \rightarrow {}^4T_1$				
E (nm)	827	854	879	1018
E $(1000\ cm^{-1})$	12.10(4)	11.71(5)	11.37(3)	9.83(1)
W $(1000\ cm^{-1})$	4.98(4)	5.43(6)	4.69(5)	2.98(2)
I (cm^{-1})	4.56(8)	4.84(9)	3.94(6)	4.42(5)
A $(1000\ cm^{-2})$	24.2(6)	28.0(8)	19.66(5)	14.0(2)
R^2	7960/305	6950/285	3030/275	2920/248

Table 19

Epidote (β) Absorption Spectra Parmeters

	20C	100C	200C	300C
baseline (abs)	0.05(c)	0.08(c)	0.35(c)	0.10(c)
a (abs)	0.0352(c)	0.0408(c)	0.038(c)	0.19(c)
b (cm^{-2})	0.007(c)	0.007(c)	0.007(c)	0.0045(c)

$^6A_1 \rightarrow {}^4A_1$

	20C	100C	200C	300C
E (nm)	455	458	459	461
E ($1000\ cm^{-1}$)	21.961(4)	21.834(6)	21.796(11)	21.67(2)
W ($1000\ cm^{-1}$)	0.562(12)	0.54(2)	0.79(4)	0.81(7)
I (cm^{-1})	8.2(2)	6.2(2)	5.7(3)	3.9(4)
A ($1000\ cm^{-2}$)	4.9(2)	3.6(2)	4.8(4)	3.4(5)

$^6A_1 \rightarrow {}^4E$

	20C	100C	200C	300C
E (nm)	477	481	483	487.
E ($1000\ cm^{-1}$)	20.942(2)	20.785(5)	20.683(11)	20.518(15)
W ($1000\ cm^{-1}$)	1.583(9)	1.606(11)	1.84(2)	1.93(2)
I (cm^{-1})	21.1(2)	19.1(2)	19.6(2)	18.0(2)
A ($1000\ cm^{-2}$)	35.6(4)	32.6(4)	38.3(7)	37.0(6)

$^6A_1 \rightarrow {}^4T_2$

	20C	100C	200C	300C
E (nm)	677	618	642	699
E ($1000\ cm^{-1}$)	14.76(2)	16.19(4)	15.58(3)	14.30(2)
W ($1000\ cm^{-1}$)	7.35(5)	5.16(8)	6.36(13)	6.7(c)
I (cm^{-1})	11.48(9)	6.2(2)	6.48(6)	8.55(7)
A ($1000\ cm^{-2}$)	89.9(10)	34.1(16)	43.8(9)	61.0(5)

$^6A_1 \rightarrow {}^4T_1$

	20C	100C	200C	300C
E (nm)	1013	846	974	1073
E ($1000\ cm^{-1}$)	9.87(2)	11.82(9)	10.27(3)	9.32(1)
W ($1000\ cm^{-1}$)	3.93(4)	7.19(9)	4.07(4)	3.6(c)
I (cm^{-1})	3.76(10)	6.96(13)	4.31(9)	7.70(7)
A ($1000\ cm^{-2}$)	15.7(6)	53.2(16)	13.7(6)	29.5(3)
R^2	10087/307	13640/256	4430/260	1515/231

Table 20

Epidote (γ) Absorption Spectral Parameters

|	20C	100C	200C
baseline (abs)	0.25(c)	0.28(c)	0.38(c)
a (abs)	0.0308(c)	0.0249(c)	0.0167(c)
b (cm^{-2})	0.008(c)	0.0085(c)	0.009(c)
$^6A_1 \rightarrow {}^4A_1$			
E (nm)	457	459	468
E $(1000\ cm^{-1})$	21.891(5)	21.771(7)	21.39(3)
W $(1000\ cm^{-1})$	0.429(14)	0.55(5)	1.11(7)
I (cm^{-1})	18.2(6)	16.8(7)	18.(4)
A $(1000\ cm^{-2})$	8.3(4)	9.8(6)	21.(5)
$^6A_1 \rightarrow {}^4E$			
E (nm)	476	479	487
E $(1000\ cm^{-1})$	21.008(3)	20.869(4)	20.54(5)
W $(1000\ cm^{-1})$	1.376(6)	1.399(7)	1.73(5)
I (cm^{-1})	74.4(13)	69.4(11)	48.(2)
A $(1000\ cm^{-2})$	109.0(19)	103.3(18)	90.(6)
$^6A_1 \rightarrow {}^4T_2$			
E (nm)	617	621	610
E $(1000\ cm^{-1})$	16.217(4)	16.111(4)	16.375(6)
W $(1000\ cm^{-1})$	3.479(10)	3.346(10)	3.674(13)
I (cm^{-1})	31.1(5)	25.7(4)	26.4(4)
A $(1000\ cm^{-2})$	115.1(19)	91.6(15)	103.(2)
$^6A_1 \rightarrow {}^4T_1$			
E (nm)	981	990	1057
E $(1000\ cm^{-1})$	10.193(5)	10.105(5)	9.458(4)
W $(1000\ cm^{-1})$	4.178(11)	3.982(13)	4.016(10)
I (cm^{-1})	15.7(3)	13.8(2)	20.2(2)
A $(1000\ cm^{-2})$	69.9(11)	56.5(10)	56.3(14)
R^2	5422/299	4267/271	5603/284
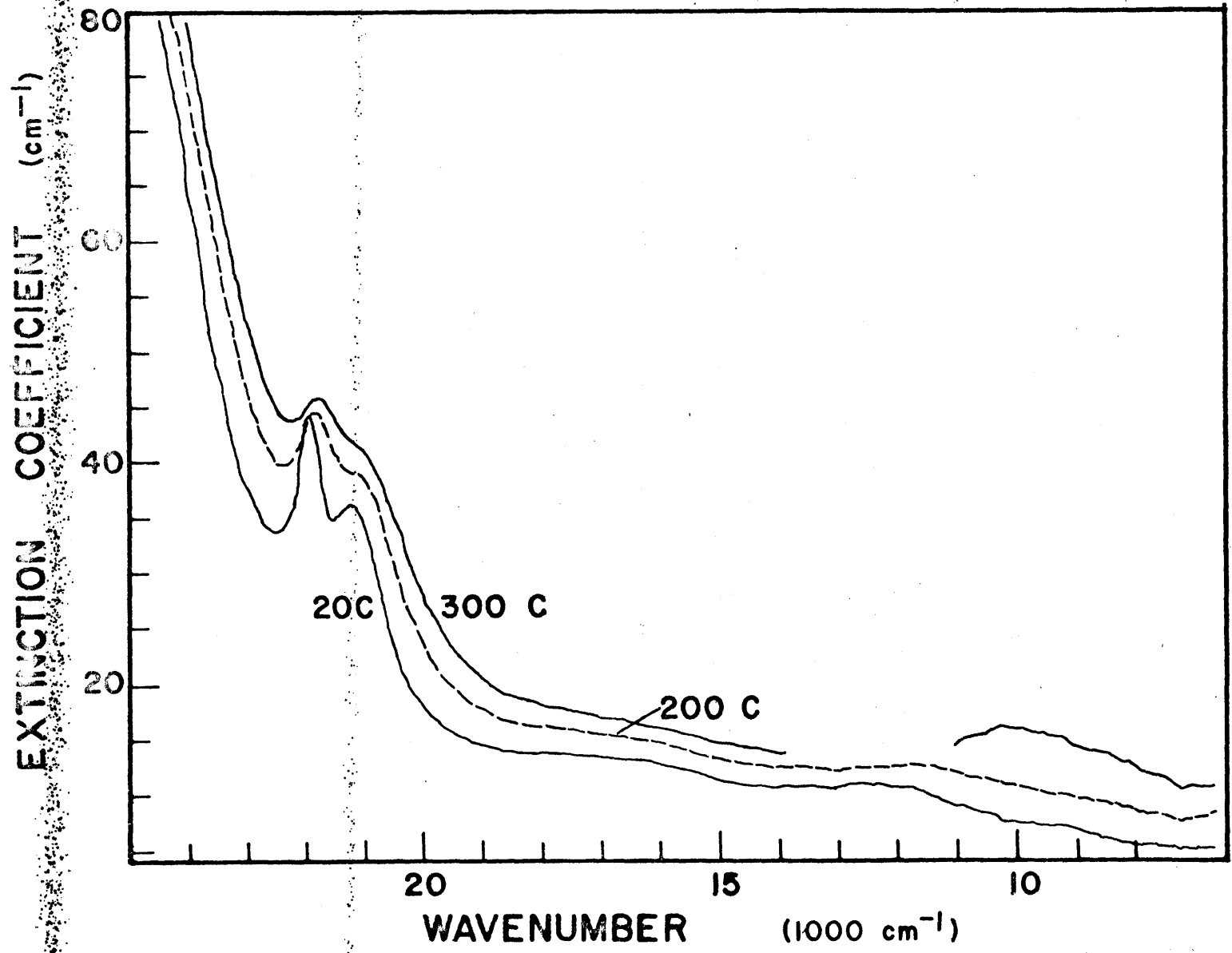
Figure 40. Absorption spectra of epidote (α) at 20C, 200C, and 300C
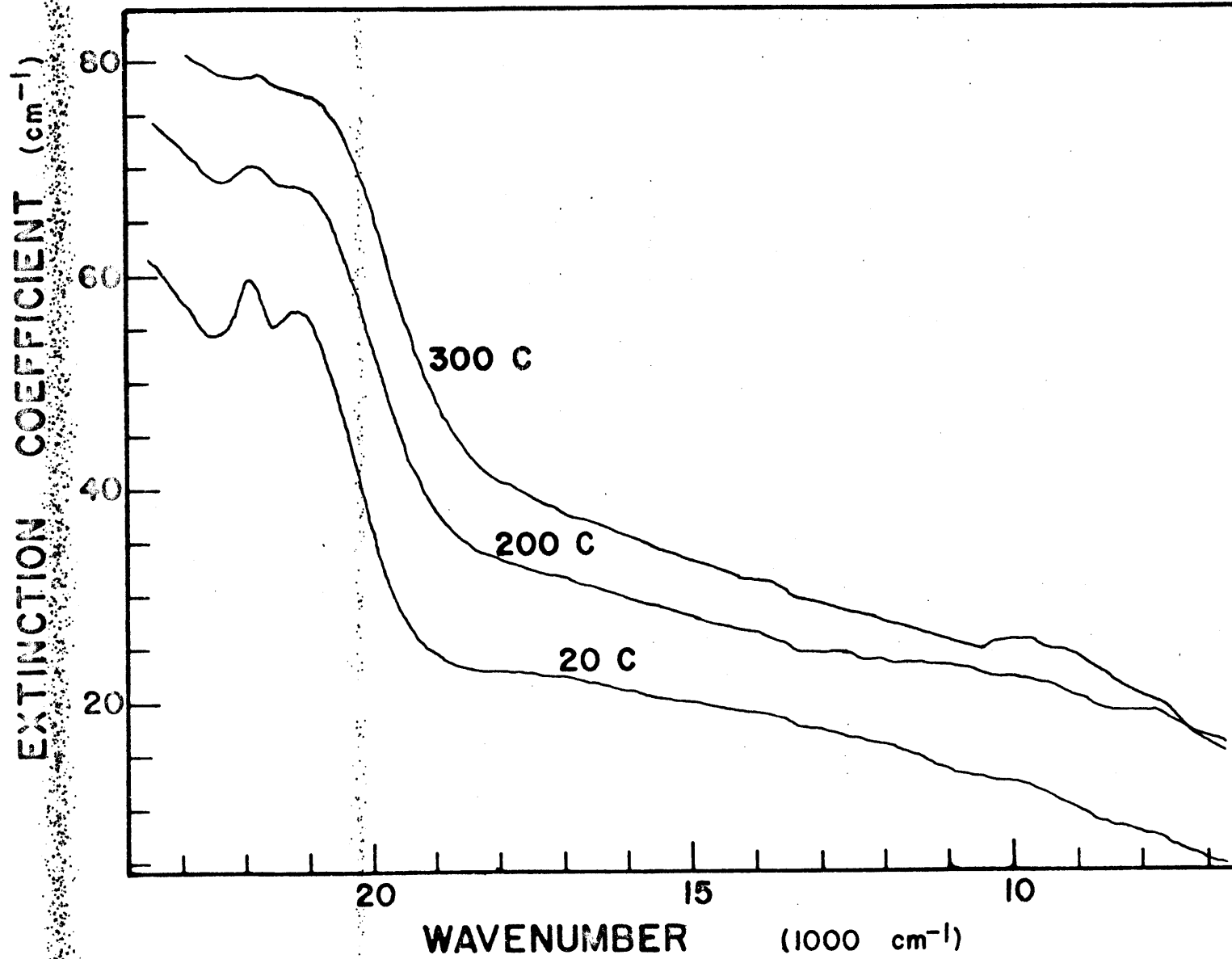
Figure 41.   Absorption spectra of epidote (β) at 20C, 200C, and 300C

of peak widths and intensities. Given these uncertainties, it is not possible to draw significant conclusions from the β-polarized spectra.

The $^6A_1 \rightarrow {}^4T_2$ (16,200 cm^{-1}) and $^6A_1 \rightarrow {}^4T_1$ (10,200 cm^{-1}) bands in the γ-polarized spectra (Figure 42) were significantly more intense than in the α- and β-polarized spectra. The high energy bands showed very little change with temperature. The change in energy of ± 150 cm^{-1} was probably more a function of the selection of the baseline than an actual shift in energy. There was no significant change in either width or intensity as the temperature increased from 20C to 200C. The lower energy band shifted ∿700 cm^{-1} to lower energy and increased slightly in intensity. Again, there was no significant change in band width with temperature. The differences between the changes in peak position due to temperature and those due to increased concentration of Fe^{3+} (Burns and Strens, 1967) indicate that the M3 site in epidote changes its size and distortion differently for the two cases.
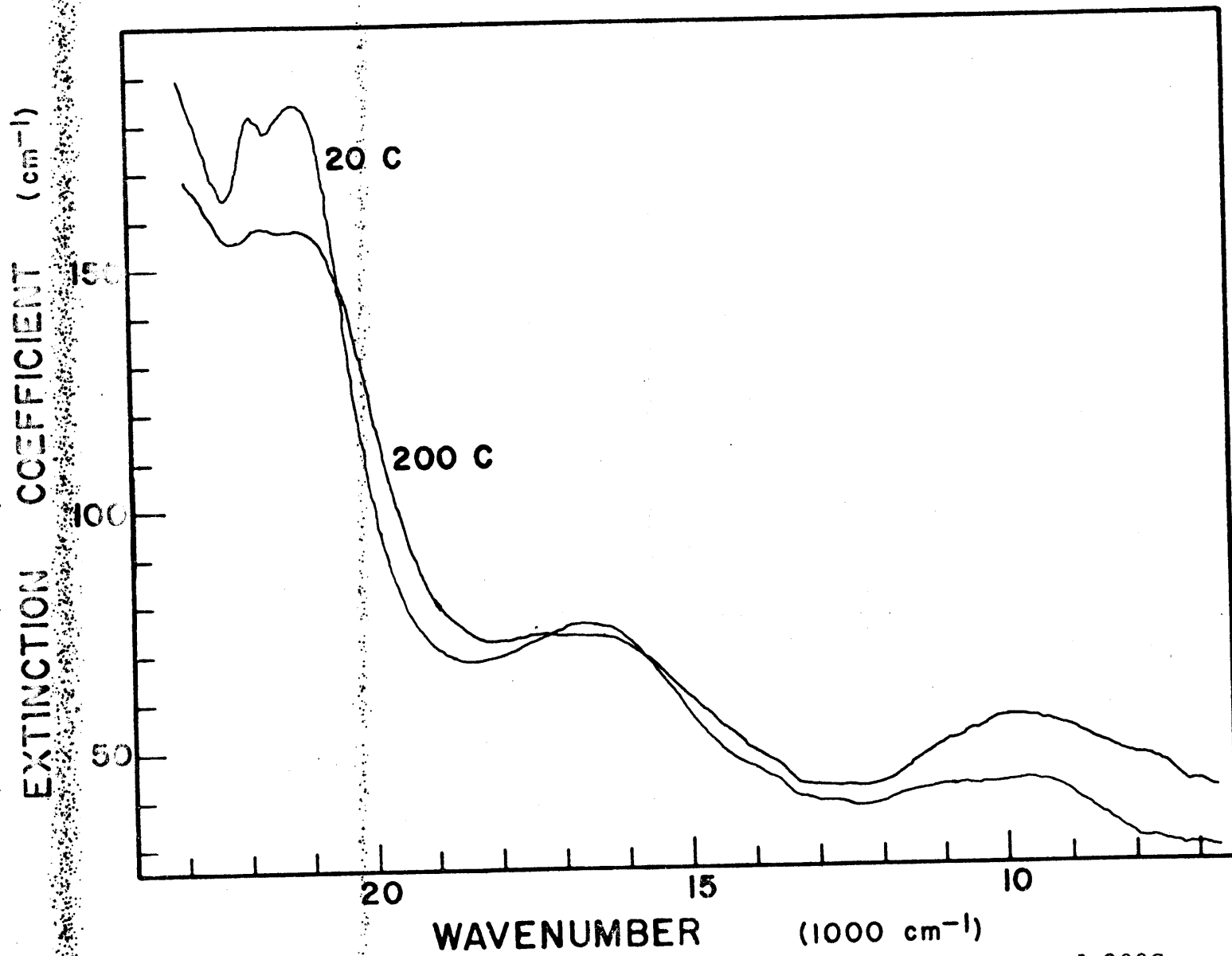
Figure 42. Absorption spectra of epidote (γ) at 20C and 200C

3. Spessartite

Mn^{2+} occupies the distorted cubic {X} site in silicate
garnets (mean M-O distance, 2.33Å, Novak and Gibbs, 1971).
Because Fe^{2+} and Fe^{3+} are common constituents of spessartites
($Mn_3Al_2Si_3O_{12}$), the assignment of the Mn^{2+} absorption spectrum
in garnet is difficult. Moore and White (1972) measured
the absorption spectra of a variety of silicate garnets.
By careful comparison of the concentration of transition
metal cations with absorption spectral features, they
concurred with the assignment of Manning (1967b) of an
intense, sharp doublet at 24,500 cm^{-1} to the $^6A_1 \rightarrow {}^4E$, $^4A_1$
transition of Mn^{2+} and bands at 20,800 cm^{-1} and 23,500 cm^{-1}
to the $^6A_1 \rightarrow {}^4T_1$ and $^6A_1 \rightarrow {}^4T_2$ transitions of Mn^{2+},
respectively. While the sharp, field independent band at
24,500 cm^{-1} is easily identified, the coincidence of broad,
weak spin-forbidden bands due to Fe^{2+}, Fe^{3+} and Mn^{2+} makes
identification of the broader $^6A_1 \rightarrow {}^4T_1$ and $^6A_1 \rightarrow {}^4T_2$ bands
difficult.

The structure of the magnesium garnet, pyrope
($Mg_3Al_2Si_3O_{12}$), has been determined by Meagher (1975)
to 750C. The {X} site increased in mean M-O distance
from 2.7Å to 2.8Å between 25C and 350C. Distortion of the
site also increased as the longer Mg(2)-O(4) bond lengths
increased at a greater rate with temperature than the
Mg(1)-O(4) bond length.

Results

The unpolarized absorption spectra of a spessartite containing 26.9 wt.% MnO and 14.9 wt.% FeO were measured at five temperatures between 20C and 400C. It was not possible to fit the spectra due to the high iron content of the sample. As discussed previously, the number and relative intensities of the spin-forbidden absorption bands due to Fe^{2+} on the {X} site are not well known. Without that information, it is not possible to separate the absorbance due to Fe^{2+} from that due to Mn^{2+}.

The field independent Mn^{2+} absorption band, $^6A_1 \rightarrow {}^4E, {}^4A_1$, is readily identified at 24,500 cm^{-1} (Figure 43). Using the Mn^{2+} assignment of Moore and White (1972) as a guide, the approximate peak positions of the other Mn^{2+} bands were determined from the digitized data and the plotted spectra (Table 21)

The $^6A_1 \rightarrow {}^4E, {}^4A_1$ band shifted to higher energy with increased temperature and decreased in intensity, in the same manner as other field-independent spin-forbidden bands. The $^6A_1 \rightarrow {}^4T_2$ and $^6A_1 \rightarrow {}^4T_1$ bands shifted to lower energy and also lost intensity with increased temperature. At 400C, the bands were nearly indistinguishable from the absorption edge.
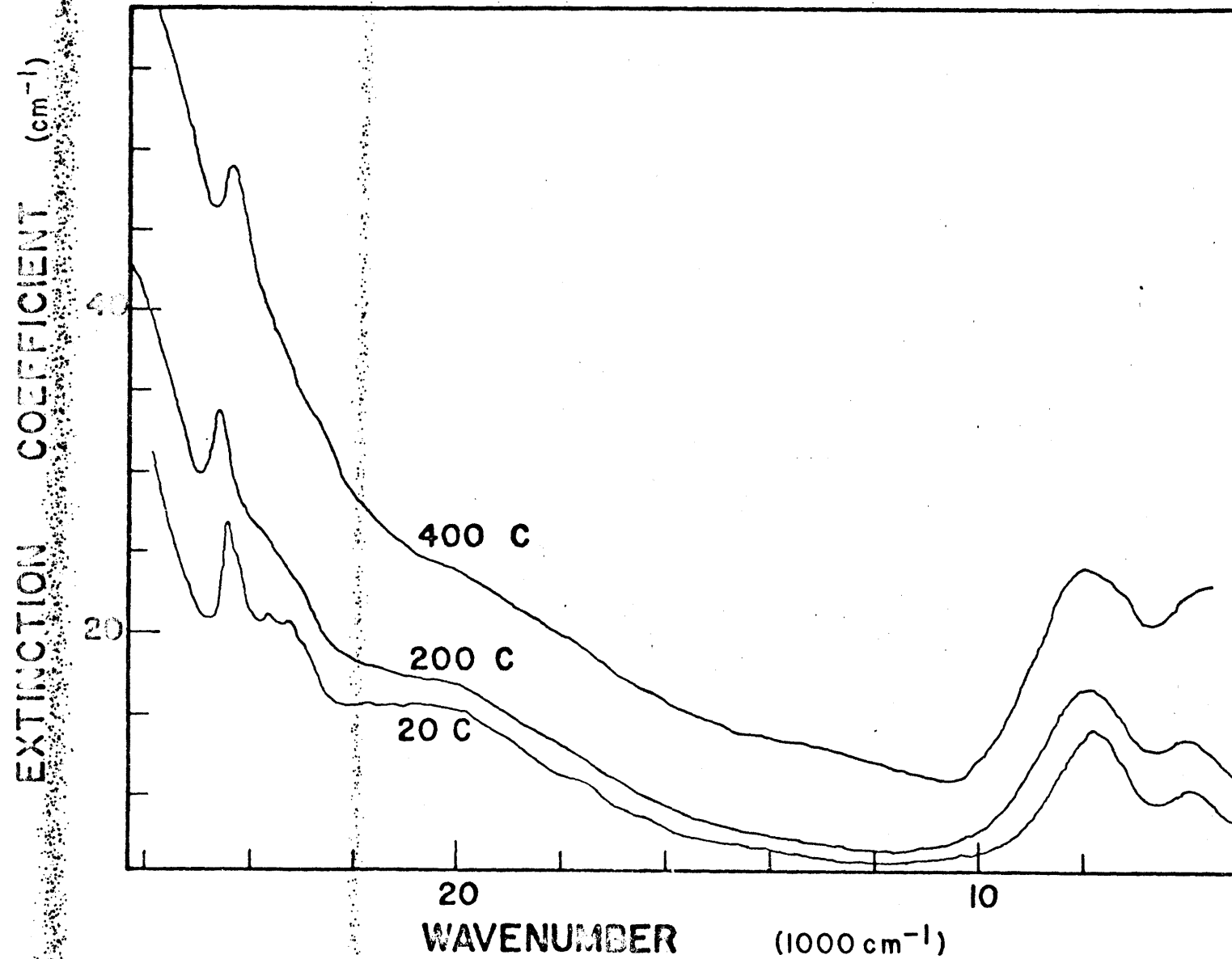
Figure 43. Absorption spectra of spessartite at 20C, 200C, and 400C

Table 21

Spessartite Absorption Peak Positions

	20C	100C	200C	300C	400C
$^6A_1 \rightarrow \ ^4E, A_1$					
E (1000 cm^{-1})	24.46	24.49	24.60	24.65	24.36
$^6A_1 \rightarrow \ ^4T_2$					
E (1000 cm^{-1})	23.3	23.4	23.4	23.3	22.8
$^6A_1 \rightarrow \ ^4T_1$					
E (1000 cm^{-1})	20.0	19.8	19.8	19.8	19.4
$Fe^{2+}-\ ^5A \rightarrow \ ^5B_2$					
E (1000 cm^{-1})	7.8	7.8	7.9	7.9	8.0

4. Rhodonite

Rhodonite, $(Mn, Fe, Ca) SiO_3$, contains five cation sites which range in mean M-O distance from $2.215Å$ to $2.418Å$ (Peacor and Niizeki, 1963). Ca^{2+} occupies the seven-coordinated M_5 site, while Fe^{2+} and Mg^{2+} preferentially occupy the nearly five-coordinated M_4 site (Dickson, 1975). Mn^{2+} occupies all five of the M sites.

The electronic absorption spectra of rhodonite has been measured by Lakshman and Reddy (1973) at 300K and 80K and Marshall and Runciman (1975) at 300K and 18K. Because of the large number of cation sites and the presence of both Fe^{2+} and Mn^{2+}, the absorption spectra of rhodonite is very complex. Similar assignments of the Mn^{2+} bands were made by both groups of workers. Marshall and Runciman (1975) were able through the use of spectra obtained at 18K on samples of varying composition to distinguish transitions due to Mn^{2+} on the seven-coordinated M_5 site. Excluding the bands due to M_5 manganese, the Mn^{2+} assignment in rhodonite can be summarized:

$$^6A_1(S) \rightarrow {}^4T_1(G) \quad 18,500 \text{ cm}^{-1}$$

$$^6A_1(S) \rightarrow {}^4T_2(G) \quad 23,600 \text{ cm}^{-1}$$

$$^6A_1(S) \rightarrow {}^4A_1(G) \quad 24,080 \text{ cm}^{-1}$$

$$^6A_1(S) \rightarrow {}^4E(G) \quad 24,480 \text{ cm}^{-1}$$

$$^6A_1(S) \rightarrow {}^4T_2(D) \quad 27,000 \text{ cm}^{-1}$$

$$^6A_1(S) \rightarrow {}^4T_2(P) \quad 27,800 \text{ cm}^{-1}$$

$$^6A_1(S) \rightarrow {}^4E(D) \quad 29,200 \text{ cm}^{-1}$$

Results

The α- and β-polarized spectra of a rhodonite containing 36.2 25.% MnO, 11.8 wt.% FeO, and 4.8 wt.% CaO were measured at 20C, 100C and 200C in the spectral region 320nm to 2100nm and at 300C and 400C in the region 320nm to 750nm. Due to the large number of absorption bands and the high degree of overlap, the spectra were not computer fit. The two field-independent bands at 29,120 cm^{-1} ($^6A_1 \rightarrow {}^4E$ (D)) and 24,460 cm^{-1} and 24,180 cm^{-1} ($^6A_1 \rightarrow {}^4A_1$, E (G)) were easily distinguished (Figures 44 and 45). An intense, broad band near 10,000 cm^{-1} and a shoulder near 6700 cm^{-1}, which were assigned by Marshall and Runciman (1975) to transitions of Fe^{2+} on the M_4 site, were the other major features of the spectra. Absorption bands due to the $^6A_1 \rightarrow {}^4T_1$ (G) transition near 18,500 cm^{-1} and bands due to the $^6A_1 \rightarrow {}^4T_2$ (D) transition near 27,800 cm^{-1} were also identified. The energies of these bands, as determined from the digitized data, are reported in Table 22.

The field independent Mn^{2+} bands shifted to slightly lower energies with increased temperature. The band at 29,150 cm^{-1} exhibited the decrease in absorption intensity which has been observed in bands due to field-independent spin-forbidden transitions in Cr^{3+}- and Fe^{3+}-minerals. The band at 24,500 cm^{-1}, however, did not decrease significantly with increased temperature. The band broadened and, above 200C, the doublet due to the $^6A_1 \rightarrow {}^4E$ (G) and $^6A_1 \rightarrow {}^4A_1$ (G) transitions was not apparent, as it had been at 20C. The bands due to field-dependent $^6A_1 \rightarrow {}^4T_2$ (G) and $^6A_1 \rightarrow {}^4T_2$ (D)
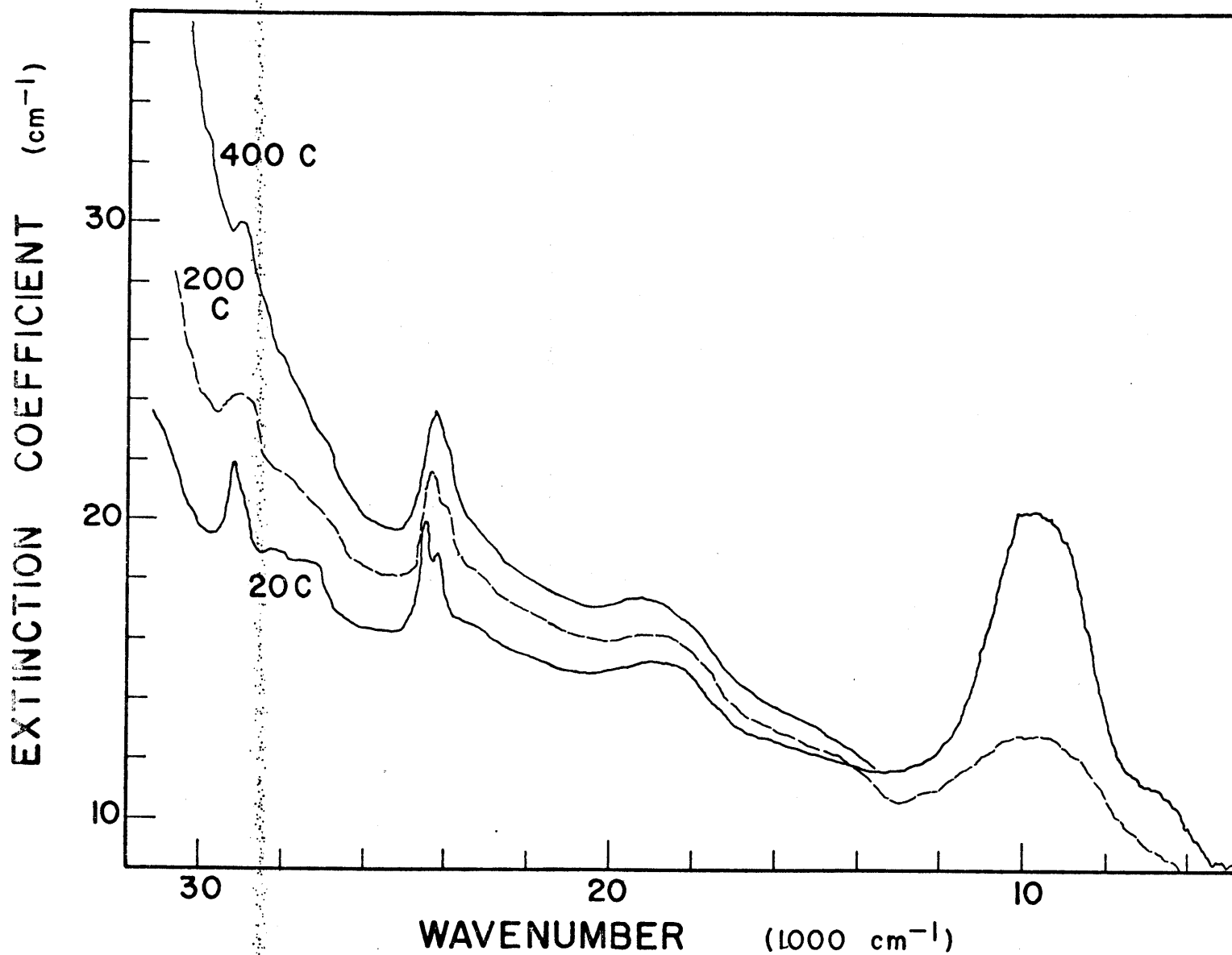
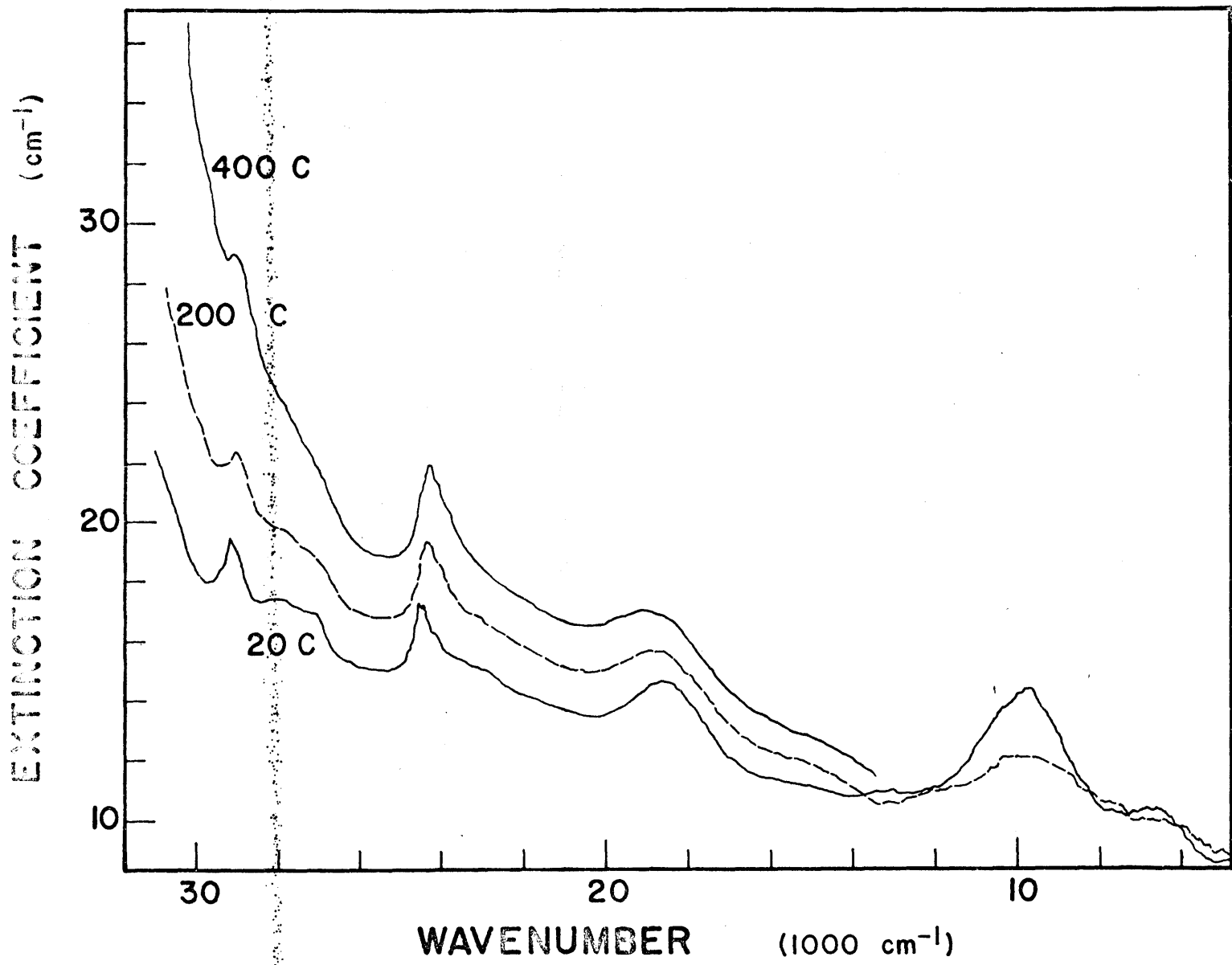Figure 44. Absorption spectra of rhodonite (α) at 20C, 200C, and 400C

Figure 45. Absorption spectra of rhodonite (β) at 20C, 200C. and 400C

Table 22

Rhodonite Absorption Peak Positions

	RT	100	200	300	400
$^6A_1 \to {}^4E(D)$					
α E(1000 cm^{-1})	29.12	29.02	29.00	28.98	28.97
β E(1000 cm^{-1})	29.17	29.07	28.99	28.98	28.97
$^6A_1 \to {}^4T_2(D)$					
α E(1000 cm^{-1})	27.0	27.2	26.9	26.9	
β E(1000 cm^{-1})	27.2	27.0	27.0		
$^6A_1 \to {}^4E(G)$					
α E(1000 cm^{-1})	24.46	24.39	24.33	24.32	24.23
β E(1000 cm^{-1})	24.53	24.39	24.32	24.33	24.24
$^6A_1 \to {}^4A_1(G)$					
α E(1000 cm^{-1})	24.18	24.11	24.09		
β E(1000 cm^{-1})					
$^6A_1 \to {}^4T_2(G)$					
α E(1000 cm^{-1})	23.6	23.3	23.1	22.9	
β E(1000 cm^{-1})	23.4	23.2	22.8	22.7	
$^6A_1 \to {}^4T_1(G)$					
α E(1000 cm^{-1})	18.4	18.5	18.5	18.5	18.6
β E(1000 cm^{-1})	18.5	18.5	18.6	18.6	18.6
Fe^{2+}: $^5A' \to {}^5A''$					
α E(1000 cm^{-1})	9.8	9.6	9.3		
β E(1000 cm^{-1})	9.7	9.7	9.6		
Fe^{2+}: $^5A' \to {}^5A'$					
α E(1000 cm^{-1})	6.5	6.6			
β E(1000 cm^{-1})	6.5	6.5	6.5		

at 23,500 cm^{-1} transitions decreased in energy and intensity with increased temperature, while the band at 18,500 cm^{-1} due to $^6A_1 \rightarrow {}^4T_1$(G) exhibited very little change in peak position or intensity. The decrease in energy of the field-dependent absorption bands was unexpected, as a decrease in the influence of the crystal field due to site expansion should cause an increase in the energy of the bands (Figure 31). The effect may have been due to the multiple site occupancy of Mn^{2+} if the sites expand and/or distort differently with temperature.

CHAPTER 8

Discussion and Conclusions

Changes in spectral parameters with temperature can be correlated with structural changes, primarily, and with changes in the character of the cation-ligand bond. Sung et al. (1977) correlated the changes in absorption band energies of olivine, orthopyroxene, and clinopyroxene with known structural changes. With the exception of the M2 site in olivine, all the Fe^{2+} crystal field bands shifted to lower energy with increased temperature. Using the data presented for Fe^{2+} on the M1 site in olivine in Figure 3 of Sung et al (1977), we note that the average energy of the two bands arising from the splitting of the ^5E state ("Δ_{vi}") decreased by $\sim400cm^{-1}$ in forsterite and by $\sim200cm^{-1}$ in fayalite as the temperature increased from 25C to 400C. Over the same temperature range, the M1 site increased in mean M-O distance by $0.012\overset{o}{A}$ in forsterite (Smyth and Hazen, 1973) and $0.003\overset{o}{A}$ in fayalite (Smyth, 1975). The spectral changes with temperature correlate well both in direction and magnitude with the "reference curves" of Faye (1972) which predict changes in "Δ_{vi}" of $\sim150\ cm^{-1}$ per $0.01\overset{o}{A}$ difference in mean M-O distance.

The theoretical relationship between the d-orbital splitting due to an octahedral crystal field (Δ_o) and the splitting due to a cubic (Δ_c) or tetrahedral field (Δ_t) is

$$\Delta_c = \frac{8}{9}\Delta_o \text{ and } \Delta_t = \frac{4}{9}\Delta_o$$

for polyhedra with the same M-O distances (Burns, 1970). Δ_c for Fe^{2+} in almandine can be calculated from the absorption spectral data and the Mössbauer data of Huggins (1975). From the slight decrease of Δ_c from 5400 cm^{-1} at 20C to 5300 cm^{-1} at 400C (Δ_o of 6100 cm^{-1} to 6000 cm^{-1}), a change in mean M-O distance of <0.01Å is expected. While the high temperature structure of almandine has not been determined, Meagher (1975) reported the structure of pyrope to 750°. The mean M-O distance of the {X} site increased 0.013Å over the temperature range 20C to 400C. When it is noted that the change in cation site size with temperature is commonly less for Fe^{2+} minerals than for isostructural Mg^{2+} minerals (e.g., hedenbergite-diopside, Cameron et al., 1973), the prediction of an increase in mean M-O distance of <0.01Å for the {X} site in almandine appears reasonable.

The relationship between the mean M-O distance and Δ_o in Cr^{3+}-minerals is not as well defined as in Fe^{2+}-minerals. Using the data presented by Burns (1975), a plot of mean M-O distance versus Δ_o for a suite of Cr^{3+}-minerals is given in Figure 46. There is substantially more scatter in the data for Cr^{3+} minerals than for Fe^{2+} (Faye, 1972; Goldman, 1977). A linear least squares regression of the data indicated a decrease in Δ_o of ∿60 cm^{-1} per 0.01Å increase in mean M-O distance; however the coefficient of determination (r^2) was 0.25. Elimination of kammererite and emerald from the regression analysis, simply because they appeared to deviate most significantly from the trend of the remaining data, improved
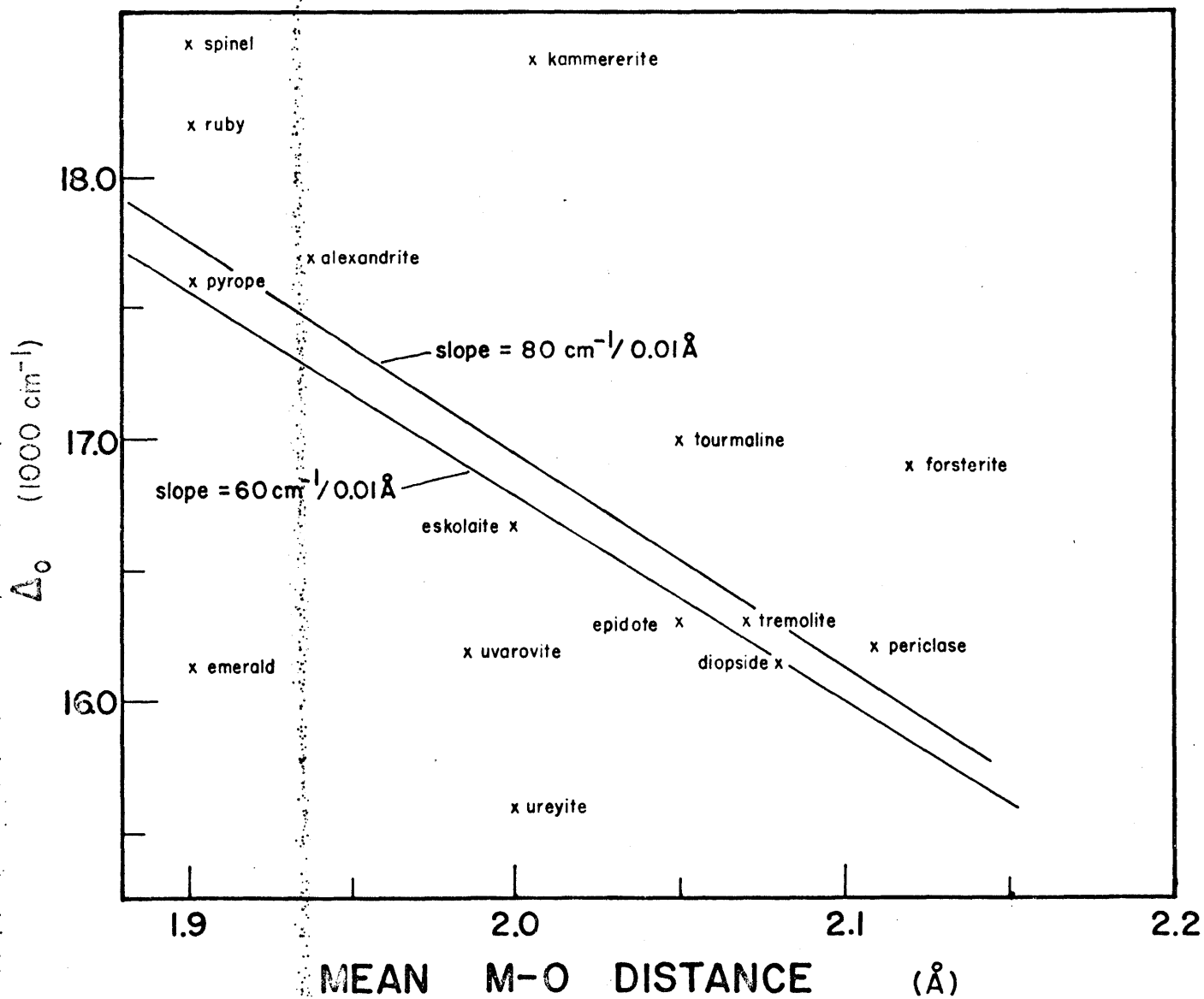
Figure 46. Cr^{3+} crystal field splitting parameter Δ_o versus mean metal-oxygen distance (data from Burns, 1975)

r^2 to 0.49 and changed the slope slightly to ~80 cm^{-1}/0.01Å. Clearly, the only conclusions to be drawn from the data in Figure 46 are that Δ_o for Cr^{3+} minerals decreases slightly with increasing site size, but that unlike the case of Fe^{2+}-minerals, Δ_o is not an adequate measure of Cr^{3+}-site size.

Abu-Eid and Burns (1976), utilizing the same data of Burns (1975), determined a better measure of Cr^{3+}-site size in the B Racah parameter. A linear trend of increasing B with increasing Cr-O distance (~50 cm^{-1}/0.1Å) was determined for the minerals with only O^{2-} among the coordinating ligands. The B Racah parameter is a measure of interelectronic repulsion, and hence, is an indicator of the degree of covalency of the cation-ligand bond. A short cation-ligand distance allows overlap of the cation d-orbitals and ligand orbitals, in effect, increasing the size of the cation orbitals and decreasing interelectronic repulsion. Abu-Eid and Burns (1976) reported a decrease in the B parameter with increased pressure for Cr^{3+}, Fe^{3+} and Fe^{2+} minerals, indicating both an increase in orbital overlap and a decrease in M-O distance.

The effect of temperature on Cr^{3+} spectral parameters is not so easily explained. Δ_o in emerald is significantly less than what would be expected based on site size alone (Figure 46). In the temperature range 20C to 400C, Δ_o decreased 700 cm^{-1}. Considering only the slope of the Cr^{3+}-mineral data in Figure 46, this indicated an increase in Cr^{3+}-O distance of ~0.08Å. The B Racah parameter increased

by ~85 cm^{-1}, indicating a M-O distance increase of ~0.15Å.
This is unreasonable since the indicated increase in M-O
distance is significantly greater than the increase in Al-O
distance in pyrope (0.009Å) or grossularite (0.018Å,
Meagher, 1975) or the increase in Mg-O distance in structurally
similar cordierite (0.012Å, Hochella et al., 1979) over the
same temperature range.

Cameron et al. (1973) determined the crystal structure
of diopside to 1000C. The mean M-O distance of the Ml site
increased by 0.011Å in the temperature range 24C to 400C.
Over the same temperature range, Δ_o of Cr^{3+} in diopside
decreased 340 cm^{-1} and B increased 120 cm^{-1}, indicating an
unreasonable increase in mean M-O distance of 0.04-0.2Å.

Clearly, the Cr^{3+} absorption spectra parameters are not
adequate indicators of small changes in cation site size.
As noted by Abu-Eid and Burns (1976), the Cr^{3+}-minerals in
which the coordinating ligands included OH$^-$ have significantly
different B-parameter values from those with only O^{2-} in
the coordination sphere. Both Δ_o and B seem to be much
more sensitive to the bonding nature of the cation than to
its site size or distortion. The B parameter value in
ruby remained nearly constant as temperature increased from
20C to 400C while Δ_o decreased ~430 cm^{-1}. Since the
bonding of Cr^{3+} in ruby is predominantly ionic at room
temperature, little decrease in ionic character would be
expected as temperature increased and the cation site
expanded. Until the relationship between absorption spectral

parameters and bonding in Cr^{3+}-compounds is better understood,
only qualitative information can be acquired from Cr^{3+}-spectra
obtained under varying temperature and pressure conditions.

Because there are no high spin d^5 spin-allowed transitions,
the relationship of Δ_o to the energies of absorption bands is
not as easily determined for Fe^{3+}- and Mn^{2+}-minerals.
The energy at which a transition will occur depends upon
all three crystal field parameters Δ, B and C. The B-
parameter can be easily determined from the energy either
the field independent transitions $^6A_1 \rightarrow {}^4E(G)$ and $^6A_1 \rightarrow {}^4E(D)$
(Keester and White, 1968) or the field dependent transitions
$^6A_1 \rightarrow {}^4T_1(G)$ and $^6A_1 \rightarrow {}^4T_2(G)$ (Marfunin, 1979). C and Δ
can then be calculated.

Keester and White (1968) noted smaller B-values and,
presumably, a greater degree of covalent bond character
in manganese silicates as compared with MnO, MnF_2 and
$MnSO_4 \cdot 4H_2O$. However, Abu-Eid and Burns (1976) detected
no measurable energy shift of the field-independent bands
in Fe^{3+}-bearing minerals as pressure increased to 50kbar,
indicating negligible change in B and C with increased
pressure.

The absorption bands due to the field independent
transitions in Fe^{3+}- and Mn^{2+}-minerals did shift to lower
energy with increased temperature. Rhodonite was the only
mineral phase in which both field independent bands are found in
region of the spectrum which was studied. The bands
shifted to lower energy by $\sim$150 cm^{-1} between 20C and 400C,

However the B-parameter increased by less than 10 cm^{-1}.

The shift in energy of the bands resulted from the decrease
of the C-parameter from 3570 cm^{-1} at 20C to 3500 cm^{-1} at
400C. The C-parameter is also a term arising from inter-
electronic repulsion, but its relationship to bonding is
not as well known.

In order to calculate B from the spectral data of the
other Fe^{3+}- and Mn^{2+}-minerals studied, it was necessary to
use the energies of the field dependent bands, which are not
as precisely determined. The B-parameter of Fe^{3+} in andradite
and epidote and Mn^{2+} in spessartite increased by 30 cm^{-1}
to 50 cm^{-1} over the temperature range studied indicating a
decrease in covalent bond character probably due to increased
site size. Because of the difficulties in determining
precise band positions for the broad, weak bands, no attempt
has been made to compare the changes in B with varying
ionic-covalent bond types.

The other spectral change that was noted in the measurement
of absorption spectra at elevated temperature was the variation
of band intensity. As was noted earlier, the spin-allowed
absorption bands of Fe^{2+} and Cr^{3+} generally increase in
absorption intensity from 10-100% as temperature increased
from 20C to 400C, although exceptions to this trend have
been observed for Fe^{2+} in the M2 site in olivine (Sung
et al., 1977; and Fukao et al., 1968) and Fe^{2+} in rhodonite
(Figure 44). Goldman (1977) correlated absorption intensity
and cation site distortion in a suite of Fe^{2+}-octahedral

minerals. After distinguishing between centrosymmetric and non-centrosymmetric cation sites, Goldman noted an increase in molar absorptivity with increased mean M-O distance and with increased range of M-O distances within a site. The distinction between centrosymmetric and non-centrosymmetric sites is important in that d-d transitions are symmetry-forbidden in centrosymmetric sites and absorption intensity must be the result of vibronic coupling (Figgis, 1966).

It was noted earlier that the most dramatic increase in absorption intensity of the Cr^{3+} spin-allowed bands in emerald and ruby was observed for the symmetry-forbidden transitions $^4A_2 \rightarrow {}^4A_1$ ruby (Figure 6) and $^4A_2 \rightarrow {}^4A_2$ in emerald. Integrated intensity of these bands increased more than 100% as temperature increased ∿380C as compared with the 10-50% increases observed in the symmetry-allowed bands. This observed increase was attributed to an increase in the occupancy of higher energy vibrational levels with increased temperature (McClure, 1962). It was also noted that all the spin-allowed absorption bands increased in intensity more than 100% in almandine garnet over the same temperature range, despite the fact that two of the three bands are symmetry-allowed. This may be an indication of the increase in distortion of the eight-coordinated {X} site with increased temperature, as was observed in the structure of pyrope determined at elevated temperature. However, at this point the data are too sparce to draw general conclusions concerning the change in intensity of absorption bands with temperature.

From this study of the electronic absorption spectra of minerals at elevated temperature, the following conclusions may be drawn:

1) For Fe^{2+}-minerals, the decrease in the crystal field splitting parameter Δ can be an indicator of the magnitude of cation site expansion with increased temperature. Δ is not a good indicator of site expansion for Cr^{3+}-minerals.

2) The B Racah parameter generally increases with increasing temperature in Cr^{3+}-minerals, indicating an increase in mean M-O distance and a decrease in cation-ligand bond covalency. An exception to this trend is Cr^{3+} in ruby where no significant change in B was determined as temperature increased from 20C to 400C.

3) The field independent crystal field bands of Mn^{2+} and Fe^{3+} shift to lower energy with increased temperature. Since the energy of the transitions giving rise to the bands is independent of the crystal field, the interelectronic repulsion parameters B and/or C decreases with temperature.

4) The intensities of field-dependent absorption bands generally increase with temperature. The intensities of bands which are forbidden by the symmetry selection rules and gain intensity through vibronic coupling increase at a greater rate than the intensities of symmetry-allowed bands.

5) The intensities of field-independent spin-forbidden absorption bands decrease with increased temperature. At present, no explanation of this effect can be presented.

These results indicate three main areas for further
research in the area of high temperature absorption spectroscopy
of minerals.

1) The data obtained so far demonstrate the usefulness
of high temperature absorption spectra in examining the crystallo-
graphic environment of Fe^{2+} ions. Other minerals with Fe^{2+} in
various environments need to be examined especially those minerals
for which crystal structural information at elevated temperature
exists. The olivine and pyroxene spectra need to be reexamined
utilizing the spectral fitting procedure introduced here in
order to quantify the trends observed by Burns (1965), Fukao
et al. (1968) and Sung et al. (1977). Also, since Fe^{2+} spectra
appear to give the best structural information at elevated
temperatures of the transition metal ions studied, the electroni-
cally similar ions Mn^{3+}, Cu^{2+} and possibly Ti^{3+} should be examined.

2) The lack of structural information available from the
Cr^{3+}-spectra indicates a need for substantial work to be done
theoretically and experimentally in order to more fully understand
the electronic environment of d^3-ions. Molecular orbital
calculations may be of use in determining the relative effects
of coordination site size, ligands and bond covalency on the
energies of d^3-electronic transitions.

3) In order to more fully use the absorption spectra fitting
routine developed here, the problems described in Chapter 4
concerning the statistical or experimental weighting of the
data and the lineshape of both peaks and background need to be
resolved.

The results presented here constitute a preliminary study of the effect of temperature on the electronic absorption spectra of minerals. Further work of both an experimental and theoretical nature needs to be done in order to utilize high-temperature absorption spectra as either a structural probe of transition metal ions in minerals or as a prospecting tool for the location of transition metal-bearing minerals on planetary surfaces through remote sensing. The value of the technique to investigate a specific cation in a specific site provides the impetus for such further research.

REFERENCES

Abu-Eid, R.M. (1976) Absorption spectra of transition metal-bearing minerals at high pressures, In: The Physics and Chemistry of Minerals and Rocks, (R.G.J. Strens, ed.), John Wiley and Sons, London, 641-676.

Abu-Eid, R.M. and Burns, R.G. (1976 The effect of pressure on the degree of covalency of the cation-oxygen bond in minerals, Amer. Mineral. 61, 391-397.

Albee, A.L. and L. Ray (1970) Correction factors for electron probe microanalysis of silicates, oxides, carbonates, phosphates, and sulfates, Anal. Chem. 42, 1408-1414.

Bancroft, G.M. and Burns, R.G. (1967) Interpretation of the electronic spectra of iron in pyroxenes. Amer. Mineral. 52, 1278-1277.

Bence, A.E. and A.L. Albee (1968) Empirical correction factors for the electron microanalysis of silicates and oxides. Jour. Geol. 76, 382-403.

Berkes, J.S. (1968) Energy level diagrams for transition metal ions in cubic crystal fields, MRL Manager 2, Mat. Res. Lab, Pennsylvania State Univ.

Bloss, F.D. and Papike, J.J. (1973) (eds) High Temperature Crystal Chemistry. Am. Mineral. 58, 577-705.

Boksha, O.N., Varina, T.M. and Kostyukova, I.G. (1974) Structure of the absorption spectrum of chromdiopsides, Soviet Physics-Crystallography 19, 241-242 (transl. from Kristallografiya, 19, 392-394, 1974).

Bragg, W.L. and J. West (1926) The structure of beryl, $Be_3Al_2Si_6O_{18}$ Proc. Roy Soc. (London) A111, 691-714.

Brown, G.E. and Prewitt, C.T. (1973) High-temperature crystal chemistry of hortonolite, Amer. Mineral. 58, 577-587.

Burnham, C.W. (1963) Refinement of the crystal structure of kyanite Z. Krist. 118, 337-360.

Burns, R.G. (1965) Electronic spectra of silicate minerals: applications of crystal field theory to aspects of geochemistry, Ph.D. Diss. U. California, Berkeley, CA.

Burns, R.G. (1970) Mineralogical Applications of Crystal Field Theory, Cambridge Univ. Press, London 225 pp.

Burns, R.G. (1975) Crystal field effects in chromium and its partitioning in the mantle, Geochim. et Cosmachim Acta, 39, 857-864.

Burns, R.G. and R.G.J. Strens (1967) Structural interpretation of the polarized absorption spectra of the Al-Fe-Mn-Cr epidotes, Mineral. Mag. 36, 204-226.

Cameron, M, Sueno, S; Prewitt, C.T., and Papike, J.J. (1973) High temperature crystal chemistry of acmite, diopside, hedenbergite, jadeite, spodumene, and ureyite, Amer. Mineral. 58, 594-618, structure 400-1000c.

Clark, Jr., S.P. (1957) Absorption spectra of some silicates in the visible and near infrared, Amer. Mineral. 42, 732-742.

Dickson, B.L. (1975) The iron distribution in rhodonite, Amer. Mineral. 60, 98-104. MS

Dickson, B.L. and Smith, G. (1976) Low-temperature optical absorption and Mossbauer spectra of staurolite and spinel. Canad. Mineral. 14, 206-215.

Duncan, J.F. and Johnston, J.H. (1974) Single crystal ^{57}Fe Mossbauer studies of the site positions in cordierite, Austr. J Chem. 27, 249-258.

Faye, G.H. (1972) Relationship between crystal-field splitting parameter, "Δ_{VI}", and M_{host} - 0 bond distance as an aid in the interpretation of absorption spectra of Fe^{2+}-bearing silicates, Canad. Mineral. 11, 473-487.

Figgis, B.N. (1966) Introduction to Ligand Fields, Wiley Interscience, New York 350 p.

Fukao, Y, Mizutani, H. and Uyeda, S. (1968) Optical absorption specta at high temp. and radiative thermal conductivity of olivines, Phys. Earth Planet Interiors 1, 57-62.

Gabe, E.J., Portheine, J.C., and Whitlow, S.H. (1973) A reinvestigation of the epidote structure: confirmation of the iron location, Amer. Mineral. 58, 218-223.

Gibbs, G.V., D.W. Breck, and Meagher, E.P. (1968) Structural refinement of hydrous and anhydrous synthetic beryl, $Al_2(Be_3Si_6)O_{18}$ and emerald $Al_{1.9}Cr_{0.1}(Be_3Si_6)O_{18}$, Lithos 1, 275-285.

Goldman, D.S. (1977) Crystal-field and Mossbauer applications to the study of site distribution and electronic properties of ferrous iron in minerals with emphases on calcic amphiboles, orthopyroxeros and cordierite, Ph.D. thesis, Cal. Inst. Tech, (Pasadena).

Goldman, D.S., Rossman, G.R. and Parkin, K.M. (1978). Channel constituents in beryl, Phys. Chem. Minerals 3, 225-235.

Hochella, M.F., Brown, G.E., Ross, F.K. and Gibbs, G.V. (1979) High-temperature crystal chemistry of hydrous Mg- and Fe-cordierites, Amer. Mineral. $\underline{64}$, 337-351.

Huggins, F.E. (1975) The 3d levels of ferrous ions in silicate garnets, Amer. Mineral. $\underline{60}$, 316-319.

Jørgensen, C.K. (1958) The interelectronic repulsion and partly covalent bonding in transition-group complexes, Disc. Faraday Soc. $\underline{26}$, 110-115.

Keester, K.L. and White, W.B. (1968) Crystal-field spectra and chemical bonding in manganese minerals. In Papers and Proceedings, International Mineralogical Association (1966) p. 22-35.

Kushida, T. (1966) Absorption spectrum of optically pumped ruby. I: Experimental study of spectra in excited states, J. Phys. Soc. Japan $\underline{21}$, 1331-41.

Lager, G.A. and Meagher, E.P. (1978) High temperature structural study of six olivines, Amer. Mineral. $\underline{63}$, 365-377.

Lakshman, S.V. and Reddy, B.J. (1973) Optical absorption spectrum of Mn^{2+} in rhodonite, Physica $\underline{66}$, 601-610.

Langer, K. (1976) Synthetic $3d^{3+}$ - transition metal bearing kyanites $(Al_{2-x}M_x^{3+})SiO_5$. The Physics and Chemistry of Minerals and Rocks, R.G.J. Strens, ed. New York (Wiley-Interscience) 389-402.

Langer, K. and Abu-Eid, R.M. (1977) Measurement of the polarized absorption spectra of synethetic transition metal-bearing silicate microcrystals in the spectral range 44,000-4,000cm^{-1}, Phys. Chem. Miner., $\underline{1}$, 273-299.

Langer, K. and Seifert, F. (1971) High-pressure, high-temp-
erature synthesis and properties of chromium kyanite
Z. anorg. allg. Chem. 383, 29-39.

Loeffler, B.M. and Burns, R.G. (1976) Shedding light on the
color of gems and minerals, Amer. Scien. 64, 636-647.

Manning, P.G. (1967a) The optical absorption spectra of some
andradites and the identification of the $'A_1 \to {}^4A_1$, $E(G)$
transition in octahedrally bonded Fe^{3+}, Can. Jour. Earth
Sci. 4, 1039-1047.

Manning, P.G. (1967b) The optical absorption spectra of the
garnets almandine-pyrope and spessartine and some struc-
tural interpretations of mineralogical significance, Canad.
Mineral. 9, 237-251.

Manning, P.G. (1970) Racah parameters and their relationship
to lengths and covalencies of Mn^{2+} and Fe^{3+} oxygen bends
in silicates, Can. Min. 10, 677-688.

Manning, P.G. (1972) Optical Absorption spectra of Fe^{3+} in
octahedral and tetrahedral sites in natural garnets, Can.
Min. 11, 826-839.

Mao, H.K., Bell, P.M. and Dickey, J.S., (1972) Comparison of
the crystal-field spectra of natural and synthetic chrome
diopside, Carnegie Inst. Washington Year Book 71, 538-541.

Marfunin, A.S. (1979) Physics of Minerals and Inorganic Ma-
terials, Springer-Verlag, Berlin, 340 pp.

Marshall, M. and Runciman, W.A. (1975) The absorption spectrum
of rhodonite, Amer. Mineral 60, 88-97.

McClure, D.S. (1962) Optical spectra of transition metal ions
in corundum. J. Chem Phys. 36, 2757-79.

Meagher, E.P. (1975) The crystal structures of pyrope and grossularite at elevated temperatures, Amer. Mineral 60, 218-228.

Moore, R.K. and White, W.B. (1972) Electronic spectra of transition metal ions in silicate garnets, Canad. Mineral. 11, 791-811.

Moss, S.C. and Newnham, R.E. (1964) The chromium position in ruby, Z. Kristallogr. 120, 359-363.

Noray-Szabo, I. and Sasvari, K. (1958) On the structure of staurolite, Acta Crystallogr. 11, 862-867.

Nassau, K. (1978) The origins of color in minerals, Amer. Mineral 63, 219-229.

Novak, G.A. and Gibbs, G.V. (1971) The crystal chemistry of the silicate garnets, Amer.Mineral 56, 791-825.

Peacor, D.R. and Niizeki, N. (1963) The redetermination and refinement of the crystal structure of rhodonite, $(Mn,Ca)SiO_3$, Z. Kristallogr. 119, 98-116.

Robinson, K. Gibbs, G.V., Ribbe, P.H. (1971) Quadratic Elongation: A quantitative measure of distortion in coordination polyhedra, Science, 172, 567-570.

Runciman, W.A. and Sengupta, D. (1974) The spectrum of Fe^{2+} in silicate garnets, Amer. Mienral 59, 563-566.

Schmetzer, K., Berdensinski, W. and Bank, H. (1974) Uber die Mineralart Beryll, ihre Farben und Absorptionsspektren, Zeitschrift der Deutschen Gemmonlogischen Gesellschaft 23, 5-39

Schmetzer, K und Medenbach (1974) Chrom-Diopsid aus Kenya, Z. Dt. Gemmol. Ges 23, 178-179.

Smyth, Joseph R. (1973) An orthopyroxene structure up to 850°C.

 Amer. Mineral $\underline{58}$, 636-648.

Smyth, Joseph R. (1975) High temperature crystal chemistry

 of fayalite. Amer. Mineral. $\underline{60}$, 1092-1097.

Smyth, J.R. and Hazen, R.M. (1973) The crystal structures

 of forsterite and hortonolite at several temperatures up

 to 900°C. Amer. Mineral $\underline{58}$, 588-593.

Stone, A.J., Aagaard, H.J., and Fenger, J. (1971) MOSSPEC:

 A programme for resolving Moessbauer spectra. Danish

 Atomic Energy Commission, Risoe Research Establishment,

 R1SO-M-1348, 42p.

Sung, C.M., Singer, R.B., Parkin, K.M. Burns, R.G. and Osborne,

 M. (1977) Temperature dependence of Fe^{2+} crystal field

 spectra: Implications to mineralogical mapping of plane-

 tary surfaces. Proc. Lunar Sci. Conf. 8th, 1063-1079.

White, W.B. and Moore, R.K. (1972) Interpretation of the spin-

 allowed bands of Fe^{2+} in silicate garnets. Amer. Mineral

 $\underline{57}$, 1692-1710.

Witzke, H. (1971) Semiempirical evaluations of Racah B and

 C parameters from crystal field spectra of chromium (III)

 complexes. Theor. Chim. $\underline{20}$:171.

Wood, D.L. (1965) Absorption, fluorescence and zeeman Effect

 in emerald. J. Chem. Phys. $\underline{42}$(10), 3404-3410.

Wood, D.L., Ferguson, J., Knox, K., and Dillon, Jr., J.F. (1963)

 Crystal-field spectra of $d^{3,7}$ ions. III Spectrum of Cr^{3+}

 in various octahedral crystal fields. J. Chem. Phys.

 $\underline{39}$, 890-898.

Wood, D.L. and Nassau, K. (1968) The characterization of beryl
and emarlad by visible and infrared absorption spectroscopy.
Amer. Mineral. 53, 777-800.